Study of New MAX Phase Materials: Sc_2AX (A = Bi, Br; X = C, B) via *Ab-initio* Method

By

Ruma Akther

MSc in Physics

Student ID: 20MSPHY010F

A thesis submitted in partial fulfilment of the requirements for the degree of MASTER OF SCIENCE in Physics

Department of Physics

CHITTAGONG UNIVERSITY OF ENGINEERING AND TECHNOLOGY

October 2024

CERTIFICATION

The thesis titled "Study of New MAX Phase Materials: Sc_2AX (A = Bi, Br; X = C, B) via *Ab-initio* Method", submitted by **Ruma Akther,** Roll No. 20MSPHY010F, Session: 2020-2021 has been accepted as satisfactory in partial fulfilment of the requirement for the degree of Master of Science (Physics) on 03 October 2024.

BOARD OF EXAMINERS

1. _____

Dr. Nusrat Jahan — Chairman (Supervisor)
Professor
Department of Physics
Chittagong University of Engineering and Technology
Chattogram-4349

2. _____

Dr. H. M. A. R. Maruf — Member (Ex-Officio)
Head
Department of Physics
Chittagong University of Engineering and Technology
Chattogram-4349

3. _____ Member

Dr. Md. Mohi Uddin
Professor
Department of Physics
Chittagong University of Engineering and Technology
Chattogram-4349

4. _____ Member

Dr. Md. Ashraf Ali
Professor
Department of Physics
Chittagong University of Engineering and Technology
Chattogram-4349

5. _____ Member (External)

Dr. Md. Kamruzzaman
Professor
Department of Physics
Begum Rokeya University, Rangpur
Rangpur-5404

Declaration

I hereby declare that the work contained in this thesis has not been previously submitted to meet the requirements for an award at this or any other higher education institution. To the best of my knowledge and belief, the Thesis contains no material previously published or written by another person except where due reference is cited. Furthermore, the Thesis complies with the PLAGIARISM and ACADEMIC INTEGRITY regulations of CUET.

Ruma Akther

20MSPHY010F

Department of Physics

Chittagong University of Engineering & Technology (CUET)

Dedication

I dedicate this thesis to my family, friends, and mentors, whose unwavering support, love, and encouragement have shaped my journey. Their guidance, patience, and belief in me have been invaluable. This achievement reflects their contributions, and I am deeply grateful to each of them for making this possible.

List of Publications

Journal Article

R. Akther, N. Jahan, M. A. Ali. “Study of New MAX Phase Materials: Sc_2AX (A = Bi, Br; X = C, N, B) via *Ab-initio* Method”. Journal of Materials Today Communication (Elsevier, IF-3. 8). https://doi.org/10.1016/j.mtcomm.2024.109679

Conference

1. Study of New MAX Phase Materials: Sc_2AX (A = Bi, Br; X = C, N, B) via *Ab-initio* Method: R. Akther, N. Jahan, M. A. Ali. (National Conference on Physics -2023) 9-11 March 2023; organized by Bangladesh Physical Society.

2. Study of New MAX Phase Materials: Sc_2AX (A = Bi, Br; X = C, N, B) via *Ab-initio* Method: R. Akther, N. Jahan, M. A. Ali. 5^{th} International conference on "Physics for Sustainable Development & Technology (ICPSDT-2023)” 7-8 September 2023; organized by Department of Physics, CUET.

Declaration

This is to certify that Ruma Akther, bearing roll number 20MSPHY010F, has carried out this research work under my supervision and she has fulfilled the relevant Academic Ordinance of the Chittagong University of Engineering and Technology so that she is qualified to submit the following Thesis in the application for the degree of MASTER OF SCIENCE in PHYSICS. Furthermore, the thesis complies with the PLAGIARISM and ACADEMIC INTEGRITY regulations of CUET.

Dr. Nusrat Jahan
Professor
Department of Physics
Chittagong University of Engineering & Technology (CUET)

Acknowledgement

I express my gratitude to Almighty Allah and extend my heartfelt thanks to my family members for their support in the successful completion of my dissertation work.

This work has been done under the supervision of Dr. Nusrat Jahan, Professor, Department of Physics, Chittagong University of Engineering and Technology (CUET). Most heartfelt thanks to Prof. Dr. Nusrat Jahan for her excellent guidance. Her intellectual mentoring, critical reviews and constructive comments contributed significantly to the formulation of my thesis. Her helpful direction and unwavering support throughout the procedure were truly encouraging, which allowed me to submit this dissertation with confidence.

I would like to express my special gratitude to Prof. Dr Md. Ashraf Ali for his constructive guidance and continuous support throughout the procedure. I thank Prof. Dr. H.M.A.R. Maruf, who is the Head of the Physics Department at Chittagong University of Engineering and Technology (CUET) for giving me the chance to do research. I am also grateful to Prof. Dr Swapan Kumar Roy, Ex-head of the Department of Physics, CUET, who was cordial throughout the research journey. I would also like to express my gratitude to Prof. Dr. Md. Mohi Uddin and Associate Prof. Dr. Mukter Hossain for their guidance. I am grateful to Prof. Dr. Mohammad Belal Hossen, Prof. Dr. Animesh Kumar Chakraborty and all other faculties for their constant encouragement and support.

I would like to thank the authority of CUET for giving me a chance to do research. I'm grateful to Advanced Computational Materials Research Laboratory (ACMRL), which is founded with the aid of a grant (grant number: 21-378 RG/PHYS/AS_G-FR3240319526) from UNESCO-TWAS and the Swedish International Development Cooperation Agency (SIDA) for giving me the computational facilities.

October 2024 Author

(Ruma Akther)

Abstract

The *ab-initio* calculation has been used to investigate the physical properties of Sc–based ternary MAX phases Sc_2AX (A = Bi, Br; X = C, B), wherein Sc_2BiB, and Sc_2BrB have been predicted for the first time. The optimized lattice constants have been obtained by minimizing the total energy. The formation energies, phonon dispersion curves, and elastic constants (C_{ij}) were calculated to confirm the thermodynamic, dynamical, and mechanical stability. The calculation of the electronic band structure revealed that the Sc_2BrB compound exhibits a semiconducting nature, whereas the remaining compounds are metallic. The mechanical behavior has been explored by calculating the elastic constants, elastic moduli, and hardness parameters. In this study, Cauchy pressure, Poisson's ratio (υ), and Pugh's ratio were calculated to assess the ductility and brittleness. Additionally, the fracture toughness and machinability index were computed to understand the resistance to crack propagation and damage tolerance behavior. This study also encompassed discussions of acoustic behavior and the *f*-index of the Sc_2AX phases. The hardness was evaluated by calculating the Vickers hardness. The Debye temperature (Θ_D), Grüneisen parameter, specific heat, thermal expansion coefficient, Helmholtz free energy, internal energy, entropy, lattice thermal conductivity (K_{ph}), minimum thermal conductivity (K_{min}), and melting temperature (T_m) were calculated to assess the title compound's suitability as thermal barrier coating materials. The optical properties were explored to assess their response to incident photons and found their compatibility as coating materials to mitigate solar heating. Finally, the obtained properties were compared with those of Sc_2AN (A = Bi, Br) so that our research takes a comprehensive form.

বিমূর্ত

Sc-ভিত্তিক ternary MAX Phase Sc_2AX (A = Bi, Br; X = C, B) এর ভৌত বৈশিষ্ট্যগুলি নিয়ে গবেষণা করতে *ab-initio* পদ্ধতি ব্যবহার করা হয়েছে, যেখানে Sc_2BiB এবং Sc_2BrB যৌগগুলোকে সম্ভাব্য MAX Phase হিসাবে ঘোষণা করা হয়েছে । যৌগগুলোর সর্বনিম্ন শক্তির মান নির্নয়ের মাধ্যমে ল্যাটিস ধ্রুবকগুলি নির্ধারণ করা হয়েছে। formation energies, phonon dispersion curves, ও elastic constants (C_{ij}) সমুহের মান বের করে তাদের thermodynamic, dynamical, and mechanical স্থায়িত্ব নিশ্চিত করা হয়েছে। ইলেকট্রনিক ব্যান্ড স্ট্রাকচার দেখিয়েছে যে Sc_2BrB যৌগটি অর্ধপরিবাহী প্রকৃতি প্রদর্শন করে, তবে বাকি যৌগগুলি ধাতব প্রকৃতি প্রদর্শন করে। যান্ত্রিক আচরণ elastic constants, elastic moduli এবং hardness parameters এর গণনা দ্বারা অনুসন্ধান করা হয়েছে। এই গবেষণায়, ductility এবং brittleness নির্ধারণের জন্য Cauchy চাপ, Poisson's অনুপাত (υ), এবং Pugh's অনুপাত গণনা করা হয়েছে। Crack propagation এবং damage tolerance আচরণ বোঝার জন্য fracture toughness এবং machinability সূচক গণনা করা হয়েছে। এই গবেষণায় Sc_2AX পর্যায়ের acoustic আচরণ এবং f-index নিয়েও আলোচনা করা হয়েছে। Vickers hardness গণনা করে hardness নির্ধারণ করা হয়েছে। Thermal barrier coating উপাদান হিসাবে যৌগটির উপযুক্ততা মূল্যায়নের জন্য Debye তাপমাত্রা (Θ_D), Grüneisen parameter, নির্দিষ্ট তাপ, তাপীয় সম্প্রসারণ সহগ, Helmholtz মুক্ত শক্তি, অভ্যন্তরীণ শক্তি, entropy, lattice তাপ পরিবাহিতা (K_{ph}), ন্যূনতম তাপ পরিবাহিতা (K_{min}), এবং গলন তাপমাত্রা (T_m) গণনা করা হয়েছে। যৌগগুলির optical বৈশিষ্ট্যগুলি আলোচিত হয়েছে তাদের incident photons এর প্রতি প্রতিক্রিয়া মূল্যায়ন করতে এবং সৌর উত্তাপ কমানোর জন্য coating উপাদান হিসাবে তাদের উপযুক্ততা খুঁজে পেয়েছে। অবশেষে, প্রাপ্ত বৈশিষ্ট্যগুলোর তুলনা Sc_2AN (A = Bi, Br) এর বৈশিষ্ট্যগুলোর সাথে করা হয়েছে, যাতে আমাদের গবেষণাটি একটি বিস্তৃত রূপ লাভ করে।

Table of Contents

CHAPTER 4: RESULTS & DISCUSSION

CHAPTER 5: CONCLUSIONS

List of Figures

List of Tables

Abbreviations

BFGS	Broyden–Fletcher-Goldfarb–Shanno
BOP	Bond Overlap Population
BZ	Brillouin Zone
CBM	Conduction Band Minimum
CC	Coupled Cluster
CDM	Charge Density Mapping
CO	Crystal Orbital
DF	Density Functional
DFPT	Density Functional Perturbation Theory
DFT	Density Functional Theory
DOS	Density Of States
DP	Dulong–Petit
EBS	Electronic Band Structure
EVC	Effective Valence Charge
eV	Electron Volts
GGA	Generalized Gradient A pproximation
GPa	Giga Pascals
GS	Ground State
HF	Hartree-Fock
IR	Infrared
KS	Kohn and shan
LDA	Local Density Approxiamtion
LO	Longitudinal Optical
MPn	Møller–Plesset perturbation
MP	Monkhorst–Pack
PBE	Monkhorst–Pack
PBEsol	Perdew, Burke and Ernzerhof for solids
PDC	Phonon Dispersion Curves
PDOS	Partial Density of States
PHDOS	Phonon Density of States

PP	Pseudopotential
PWPP	Plane Wave Pseudopotential
TBC	Thermal Barrier Coating
TEC	Thermal Expansion Coefficient
TO	Transverse Optical
USP	Ultra-soft Pseudopotential
UV	Ultraviolet
XC	Exchange Correlation
XRD	X-Ray Diffraction

CHAPTER 1
INTRODUCTION

This chapter introduces the main topics covered in this thesis and provides a summary of the objective of this work, along with an outline of how the various chapters are structured.

1.1 Background

Traditional ceramics have a very determinate range of functional and structural applications due to their intrinsic fragility, fracture toughness, poor machinability, and damage tolerance [1]. As a result, considerable work has been put into developing techniques like composite creation, microstructure control, and bio–mimetic technology to boost the ceramic's machinability and toughness. Owing to their distinct hybrid properties that combination of metals and ceramics, a class of isotropic laminated nitrides or carbides or boron conversant as MAX phases with a chemical formula $M_{n+1}AX_n$ where M refers to a transition metal, A being the semimetal or metalloid elements belonging to group IIIA–VIA in the periodic table, X being N or C or B and n = 1–6 [2,3]. A sufficient number of ternary MAX phases were discovered in the 1960's by Nowotny and co–workers [4–7]. But these identified MAX Phases had gained adequate attention since Barsoum and co–workers synthesized high–purity dense bulk Ti_3SiC_2 in 1996 and revealed a distinct combination of some remarkable properties of engineering ceramics and metals [9].

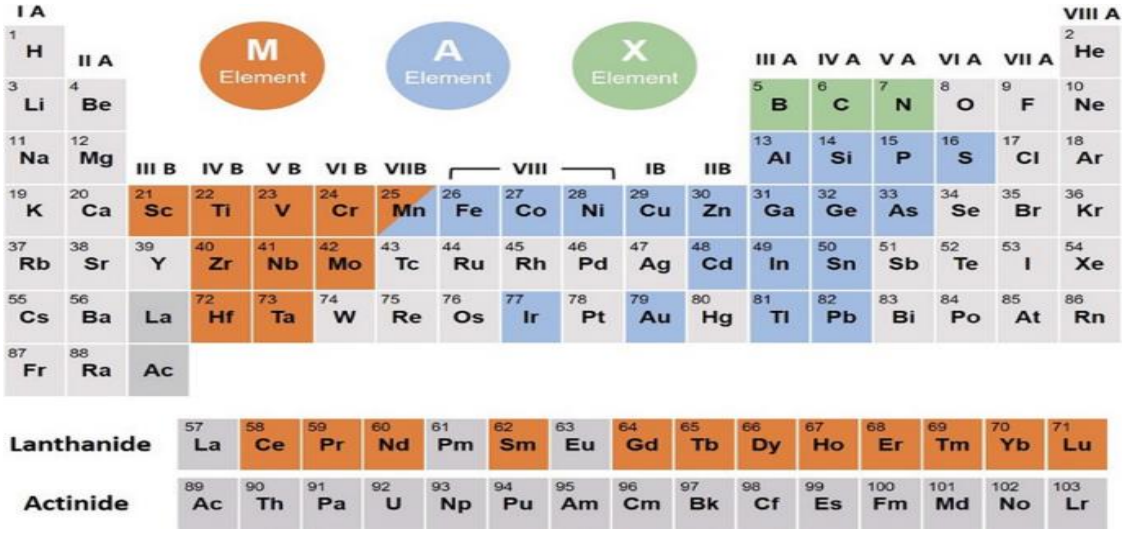

Fig. 1.1: MAX phase based periodic table. Reprinted from [8].

Building on this innovative work, research on this class of ternary compounds has expanded significantly over the last 25 years. The exploration initially focused on Ti_3SiC_2 and subsequently extended to other members of the MAX phase family [10]. The MAX phase exhibits the hybrid combination of both metallic and ceramic behavior due to its structure, which consists of stacking "ceramic" layers of MX between A "metallic" planes. Like metals, they possess thermal and electrical conductivity, resistance to thermal shock, good machinability, irradiation, and damage tolerance [11,12]. They also exhibit ceramic properties such as hardness and elastic rigidity, outstanding oxidation and corrosion resistance, and lightweight, low density with high decomposition [9]. Their metallic and ceramic properties make them multipurpose numerous potential candidates applicable for high–temperature substitutes for graphite, composites components, gas heater nozzles, high–temperature coated bearings, nuclear industry, superconducting materials, instrumentation, aerospace, bulk and coating materials, fuel cells, and sensors [13–16]. Recently, these ternary compounds are possessing to synthesize 2D nanocrystal MXenes, which are applicable in micro–super capacitors, electrochemical capacitors, Li–ion, and sodium–ion batteries as cathodes, energy storage, sensors, CO catalysts, filtration, biosensors, and antibacterial agents, further expanding the research field of interest for researchers [17,18].

1.2 Crystal Structure of MAX Phase

To study the physical characteristics, material's structure is necessary to observed. The ternary MAX phase compounds with space group P_{63}/mmc (No. 194) belong to the hexagonal crystal structure, in which an atomic layer of A atoms is interspersed between M_6X (X = C, N, B) edge shared octahedrons and One "M" atom and three "X" atoms are stacked to create a tetrahedron along the a–axis. Understanding the structural nuances of MAX phases is essential for appreciating their versatility. MAX phase can be classified into three types according to the value of n. Figure 1.2 illustrates the crystal structures of 211, 312, and 413 MAX phases. Notably, the 312 MAX phase features two distinct M sites, MI and MII, while the 413 MAX phases introduce two distinct X sites, XI and XII. Thus, for the 211 structures, there are three inequivalent atoms, while for the 312 structures there are four, and for the 413 structure there are five unique atomic sites.

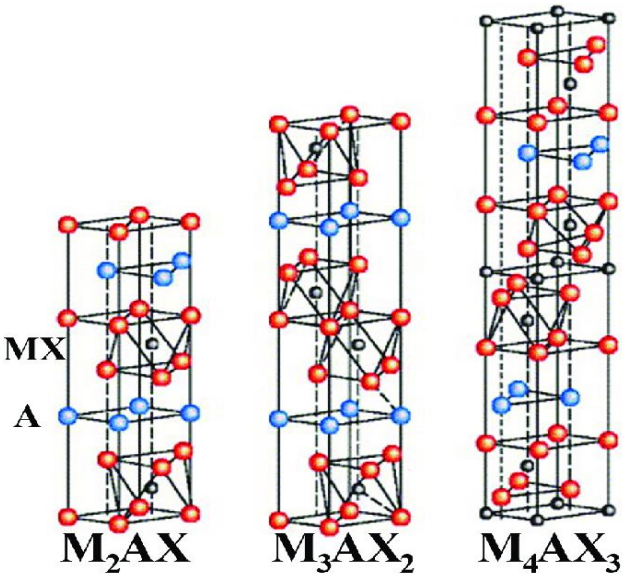

Fig. 1.2: Crystal structure of $M_{n+1}AX_n$ phase [19].

The c-axis is longer than *a* and *b* axis in all three structure, typically measuring around 12-13 Å in the 211 MAX phase structure, 17-18 Å in the 312 structure, and 22-23 Å in the 413 structures. This unique structural arrangement endows MAX phases with anisotropic properties, evident in the c/a ratios. The 211 MAX phase exhibits the *c/a* ratio of 4, while the 312 phase boasts the ratio of 6, and the 413 phase features the ratio

of 8.

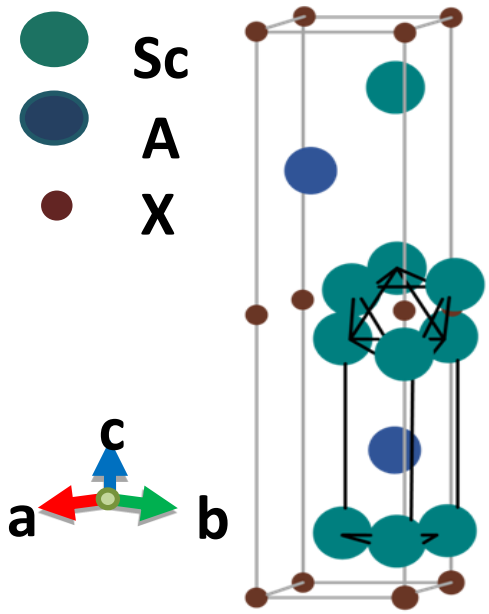

Fig. 1.3: The unit cell structure of these X (A = Bi, Br; X = C, N, B) with an edge – shared $[M_6X]$ octahedra, and a $[M_6A]$ trigonal prism are outlined.

The term "nano-laminated" aptly characterizes the MAX phase structure, highlighting its multilayered composition with nanoscale layers. This layered nature not only contributes to their anisotropy but also presents exciting opportunities for various applications. In addition to this core MAX phases, there are intriguing variants within the MAX phase family.

For instance, Figure 1.3 showcases Sc_2AX, a rare earth "Sc"-based MAX phase with similarities to the 211 MAX phase depicted in Figure 1.2. These structural intricacies, along with the remarkable properties of MAX phases, continue to capture the imagination of materials scientists, offering a rich landscape for tailoring materials to meet the diverse requirements of numerous applications.

1.3 Structural Aspects

1.3.1 Lattice parameters

The lattice parameter of MAX phases is a critical aspect that defines the structural characteristics and properties of these remarkable materials. Lattice parameters, which consist of both length and angle measurements, provide key information about the size and shape of the unit cell within the crystal lattice. In the case of MAX phases, these lattice parameters are especially vital because they govern the arrangement of atoms within the crystal structure, affecting the material's overall performance. In three-dimensional lattices of MAX phases are typically considered: *a, b,* and *c*. They represent the lengths of the sides of the unit cell. In the MAX phase hexagonal structures are characterized by equal values for '*a*' and '*b*'. Instead, the parameters '*a*' and '*c*' are used to describe the crystal lattice, with '*a*' representing the basal parameter, and *'c'* signifying the height parameter. Alongside these lengths, the lattice parameters also include three angles: α, β, and γ, measuring the angles between the lattice vectors. The angles in hexagonal MAX phases are simplified to $\alpha = \beta = 90°$ and $\gamma = 120°$. In the case of MAX phases, it's worth noting that the distances between the M atoms (metal atoms) are highly interconnected with *'a'* and closely resemble the M-M distances observed in the MX phases (binary metal compounds) [20,21]. To provide a more comprehensive perspective, it can be helpful to regard MAX compounds as interstitial compounds. In this conceptual framework [22,23], the A atoms and X atoms occupy interstitial sites within the crystal lattice, nestled among the M atoms. According to this interpretation, in the 211 phases, which consist of four layers per unit cell, the '*c*' parameter (representing the height of the unit cell) should be approximately four times the value of the '*a*' parameter (representing the basal plane of the unit cell).

1.3.2 Unit cell

The unit cells of MAX phases exhibit distinct structural features. They consist of closely packed layers of M atoms, which are separated by layers composed solely of A-group elements. In M layers, X atoms occupy the octahedral sites, forming M_6X octahedra that are identical to those found in the rock salt structure of their binary MX carbide counterparts. The A-group elements are situated at the corners of trigonal prisms, which are slightly larger and thus more accommodating to the larger A atoms compared to the octahedral sites [24–26]. When the value of 'n' is 1, there are two M layers that separate the A layers. For 'n' equal to 2, three M layers are present, and for 'n' equal to 3, there are four M layers that separate the A layers. In the case of 312 and 413 MAX phases, there are two polymorphs, denoted as α and β. The polymorphism observed in the 413 phases differs from that seen in the 312 phases, particularly in the arrangement of the A-element layers. Specifically, the difference between α- and β-413 lies in the positions of the M and X atoms. Among these phases, only Ta_4AlC_3 is found in both polymorphs in bulk form, whereas the remaining 413 phases predominantly crystallize in the α polymorph [27,28]. Furthermore, the 211 MAX phase members have two formula units within the unit cell, and each formula unit cell contains four atoms.

1.3.3 Crystallography

Within the hexagonal crystal system, we find the elements used in MAX phases. In MAX phases, the space group notation, *$P6_3/mmc$*, based on Hermann-Mauguin conventions, is employed, and it corresponds to the space group number 194. The *$P6_3/mmc$* signifies in this context:

- The "P" signifies a primitive cell, containing lattice points only at the eight corners. No further translation symmetries apply to these lattice points, and there is no additional base, body, or face-centered positions.

- The "6_3" part of *$P6_3/mmc$* represents the rotational and translational symmetry of the screw axis. In this case, the "6" indicates a 6-fold symmetry, and the subscript "3" signifies that the primary direction of this symmetry is along the c-axis, with [0001] being the primary direction. The symbol "n" denotes a symmetry component with a rotation of $2\pi/n$ and translation of (r/n) of the unit

cell length "c". So, "6_3" translates to a rotation of $2\pi/6 = \pi/3$ (60 degrees), and translation of 3/6 along the c-axis, which is half of the lattice constant.

- The "*mmc* -" part conveys the presence of mirror and glide plane symmetries when viewed perpendicularly to the primary, secondary, and tertiary axes. In the hexagonal system, the [0001] direction is considered the primary direction along the c-axis, and the [10$\underline{1}$0] direction serves as the secondary direction along the a-axis. Furthermore, [11$\underline{2}$0] is recognized as the tertiary axis, bisecting both the *'a'* and *'b'* axes. "*mm*" signifies mirror symmetry for both the (0001) and (10$\underline{1}$0) planes, while *'c'* denotes a glide plane perpendicular to [11$\underline{2}$0], featuring a glide vector of c/2. Depending on the value of "n," which can be 1, 2, 3, or 4, MAX phases are categorized into various subgroups. Notably, between the 312 and 413 phases, you find two distinct stacking layers known as α and β phases.

1.4 Aims and Objectives of the present Study

The objectives of the present research encompass a wide array of analyses to comprehensively explore the properties of Sc_2AX (A = Bi, Br); (X = C, N, B) materials of significant interest:

- In the realm of structural properties, the research will involve determining key parameters, including lattice constants, density, and volume, to gain insights into the material's crystal lattice structure of Sc_2AX phases.

- To assess the dynamical stability of Sc_2AX (A = Bi, Br); (X = C, N, B), the study will focus on computing phonon dispersion curves (PDC) and phonon density of states (PHDOS), which are crucial in understanding the material's vibrational stability.

- The electronic properties will be investigated by calculating the electronic band structure and density of states, providing a detailed picture of the energy bands and electronic structure within the material.

- In the realm of mechanical properties, the research will encompass a comprehensive exploration of various factors, including elastic constants, elastic moduli, hardness parameters, Pugh ratio, Poisson's ratio, and mechanical

anisotropy, all of which are essential for understanding how the material responds to mechanical stress and deformation.

- The study will delve into thermodynamic properties, aiming to determine the Debye temperature, minimum thermal conductivity, thermal expansion coefficient, and melting temperature, shedding light on the material's thermal behavior and phase transitions.

- In the domain of optical properties, the investigation will focus on essential constants such as the dielectric constant, refractive index, absorption coefficient, photoconductivity, reflectivity, and the loss function, providing insights into how the material interacts with light and electrical fields.

1.5 Thesis Outline:

- **Chapter 1:** The initial chapter furnishes a comprehensive overview of the ongoing research.
- **Chapter 2:** Chapter two delves into an extensive review of existing literature concerning the MAX phase, providing a comprehensive background on this material.
- **Chapter 3:** Chapter three outlines the research methodology and discusses the relevant theories associated with the material's properties.
- **Chapter 4:** Chapter four is dedicated to showcasing the research findings and conducting a subsequent in-depth discussion on the outcomes.
- **Chapter 5:** Conclusions: The pivotal findings and insights of the current study are encapsulated in chapter five, where conclusions are draw

CHAPTER 2
LITERATURE REVIEW

2.1 General

An exploration of the existing literature unveils the evolutionary trajectory of MAX phases over time. This chapter aims to furnish readers with a comprehensive understanding of the historical progression of MAX phase research. Notably, this investigation extends to boride phases within the conventional MAX structure, as well as borides characterized by distinct space groups and subtly altered structures. The pursuit of novel and practical MAX phase materials has prompted a diverse shift in research methodologies. This shift underscores the dynamic nature of our scientific inquiry, enhancing our insights into the historical context surrounding MAX phases incorporating carbon (C), nitrogen (N), and boron (B).

2.2 Literature review of the previous work:

The prevalence of MAX phases is notably extensive, owing to robust research efforts dedicated to their exploration. Although numerous compounds have been extensively studied in theory, experimental investigations have not kept pace with theoretical advancements. Notably, compounds falling within the 211-phase exhibit significantly higher availability compared to other phases.

For a considerable duration, the utilization of carbon (C) and nitrogen (N) as X elements remained restricted [6]. However, recent developments have expanded this scope to include boron (B) as an X element, marking a notable shift in MAX phase research. This extension has opened new avenues in the field, driven by the intriguing properties and potential applications of boron-containing compounds [29,30]. Despite the vast number of predicted boride phases, the synthesis of MAX phase borides remains limited, with only a few compounds successfully synthesized [31].

The theoretical research on MAX phase materials has been massive and rapidly expanding since Medvedeva *et al.* [32] presented the first *ab-initio* calculations on MAX phases in 1998 using density functional theory (DFT). To better understand and

predict the properties of the MAX phases, DFT has constantly played a vital role. The scientific community has reported about 150 MAX phases of their ongoing efforts [33]. Aryal *et al.* [34] provide the results of using *ab initio* to investigate the 792 MAX phase with the value of n = 1–4 and state that 665 are thermodynamically and elastically stable, the ones in which the M site component is rare earth Sc.

M. W. Barsoum *et al.* conducted an extensive analysis on the characterization of predominantly single-phase, fully dense Hf_2InC samples, fabricated via reactive hot isostatic pressing of elemental powders. They determined the lattice parameters 'a' and 'c' to be 0.331 nm and 1. 472 nm, respectively, for Hf_2InC. Additionally, they systematically measured heat capacities, thermal expansion coefficients, and both thermal and electrical conductivities across a range of temperatures. Remarkably, Hf_2InC demonstrates excellent electrical conductivity, evidenced by a resistivity that shows a consistent linear increase with rising temperatures. Within the temperature interval of 300 to 1273 K, the thermal expansion coefficient of Hf_2InC was identified to be 7. 63 $\times 10^{-6}$ K^{-1} [35]. This investigation contributes significant insights into the material's conductive properties and its response to thermal variations.

Keast *et al.* [36] employed density-functional theory within the WIEN2k software package to assess the stability of various phases by comparing their total energies against those of suitable competing phases. Through computational analysis, they evaluated the total energies of five distinct schemes (Cr_{n+1}-Al-C_n, Ti_{n+1}-Al-C_n, Ti_{n+1}-Si-N_n, Ti_{n+1}-Al-N_n, and Ti_{n+1}-Si-C_n), where n represents a positive integer ranging from 1 to 4. Their investigation not only confirmed the stability of these phases but also suggested the potential synthesis of metastable compounds such as Ti_2SiC, Ti_2SiN, and Ti_3AlN_2. This research underscores the utility of density-functional theory in predicting and understanding the stability and potential formation of novel phases within materials science.

Z. J. Yang *et al.* investigated the elastic and structural properties of nanolaminate Zr_2InC using first-principles calculations. They identified an ultra-incompressibility along the c-axis between 70 GPa and 400 GPa, attributed to core-valence charge transfer slowdown and rapid Zr atom shift along the c-axis. Structural instability and elastic softening occurred at 70–160 GPa and 700–850 GPa, indicating a structural

transformation. Zr_2InC initially exhibited elastic isotropic behavior, transitioning to anisotropic with increasing pressure, influencing material properties. The (B/G) and B/C_{44} ratios highlighted brittleness at ambient conditions, decreasing with pressure [37]. This study sheds light on pressure-induced properties in Zr_2InC.

Wang *et al.* [38] successfully synthesized Ti_2InB_2, a significant 212 MAX phase boride. TiB formation from Ti_2InB_2 via high temperature alloying in a vacuum removes the indium layer. They theoretically proposed that TiB single-layer structures exhibit superior potential as Li/Na ion battery anode materials compared to Ti_3C_2 MXenes, showing enhanced ion storage capacity and minimal energy barriers for Li/Na ion transport. Ali *et al.* [39] further investigated these findings extensively.

Before Barsoum and El-Raghy's publication, the MAX phase received scant attention from researchers. Their work revealed the dual metallic and ceramic properties of MAX phases [9,29]. In 2011 and 2012, researchers identified numerous 2D transition metal carbides and nitrides [30,31]. During this time, a significant number of new MAX phases were synthesized, recognized for their potential in energy storage applications and various modern technologies.

211 MAX phases were limited to X elements C, N and B, either as compounds or solid solutions. Expanding X elements beyond C/N/B, offers a substantial opportunity for diversification and participation in MAX phase materials.
From a theoretical perspective, Dahlqvist *et al.* [41] studied the stability of MAX phases with M = Sc, Ti, V, Cr, or Mn; A = Al, and X = C or N, exposing that maximum stability exists for “C” and “N” containing MAX phases, respectively, with V and Ti as the transition metals, accordingly.

Due to the promising future of B and related compounds, the X element has already been extended to B by the researchers, providing space for this alteration (known as MAX phase borides) [42]. It is currently shown that they can serve as prospective materials in a variety of fascinating sectors [43,44]. The structural, electrical, elastic, and lattice dynamical characteristics of M_2AB (M = Ti, Zr, Hf; A = Al, Ga, In) compounds were studied by G. Surucu *et al.* and they found that Ti_2AB & Hf_2AB are ductile in nature [45].

A. Bouhemadou *et al.* conducted a study on the structural and elastic properties of Sc_2AC (where A = Al, Ga, In, Tl) using first-principles calculations with the pseudo-potential plane-waves method. Their research, within the local density approximation to the exchange-correlation energy, examined the impact of high pressures (up to 20 GPa) on lattice constants and internal parameters. They also determined bulk and shear moduli, Young's moduli, Poisson's ratio, and estimated the Debye temperature based on average sound velocity for ideal polycrystalline Sc_2AC aggregates [46].

Hossain *et al.* studied the physical characteristics of Hf_2AB (A = Pb and Bi) and confirmed their potential use as covering materials to block solar radiation [47]. The formation energy, electrical, and several mechanical properties of M_2AlC, M_2AlN andM_2AlB (M = Sc, Ti, Cr, Zr, Nb, Mo, Hf, or Ta) MAX phases have been studied by Khazaei and co–workers [48].
In addition, electronic characteristics have been researched of Sc_2AC (A = Al, Ga, In, Ti) by Music *et al.* [49] whereas, Bouhemadou *et al.* [46] addressed the structural and elastic properties of these compounds. Cover *et al.* [50] investigated the elastic properties of 240 MAX phase compounds and Ali *et al.* [51] carried out a theoretical investigation to calculate the thermodynamic, optical, and lattice dynamical characteristics of the Sc_2AlC compound and revealed that it could be used as a shielding material to prevent solar heating.

The electrical structures, bonding characteristics, and defect mechanisms in the Sc_2SnC MAX phases have been studied by Hadi *et al.* [52] and it is the first Sc–based MAX phase to be described with complete crystallographic data. Sc_2InC had previously been listed among MAX phases in the literature [53], but there were no crystallographic data and the source was identified as private communication. There hasn't been any experimental proof of the synthesis and characterization of Sc_2InC. Therefore, it can be assumed that Sc_2SnC is the first Sc–based molecule in the MAX family.

Although the Sc_2InC MAX phase has not been experimentally discovered, its structure, characteristics, and potential uses are being researched using theoretical predictions. These predictions indicate that the phase is a promising candidate for coating materials that prevent solar heating as well as optoelectronic devices for visible and ultraviolet

light spectrums [54]. While S. Kuchida *et al.* [55] concentrated on non-transition metal M_2AX compounds that contain Sc, Y, and Lu atoms in the M site element; nevertheless, only polycrystalline samples of Lu_2SnC were published.

Table 2.1: Summary of the previous studies of Sc_2AX (A = Bi, Br; X = C, N, B).

Phase	Structural	Mechanical	Stability	Electronic	Thermal	Optical	Ref.
Sc_2BiC	No	Yes	Yes	No	No	No	[60]
Sc_2BiN	No	No	No	No	No	No	
Sc_2BiB	No	No	No	No	No	No	
Sc_2BrC	No	Yes	Yes	No	No	No	[60]
Sc_2BrN	No	Yes	Yes	No	No	No	[60]
Sc_2BrB	No	No	No	No	No	No	

Bouhemadou *et al.* investigated the structural and elastic properties of M_2InC compounds (where M = Sc, Ti, V, Zr, Nb, Hf, Ta) using ab initio calculations. They observed a quadratic relationship between lattice parameters and applied pressure and determined elastic constants via the static finite strain technique. Additionally, bulk and shear moduli, Young's moduli, Poisson's ratio, and Debye temperature estimates based on average sound velocity were derived for ideal polycrystalline M_2InC aggregates. This study represents the first comprehensive theoretical prediction of elastic properties for Sc_2InC, Ti_2InC, V_2InC, Zr_2InC, Nb_2InC, Hf_2InC, and Ta_2InC compounds, awaiting experimental validation [56]. So far, some of MAX phases borides: M_2SB [M = Hf, Nb, Zr] [57] , Hf_2TeB [58], Zr_2SeB, Hf_2SeB [59] have also been synthesized.

2.3 Motivation for the present work

In this study, we have chosen to explore the theoretical analysis of the structural, electrical, thermal, phonon dynamic, mechanical, acoustic, and optical properties of Sc_2AX (A = Bi, Br; X = C, N, B) MAX phases. The Sc_2BiC, Sc_2BrC, and Sc_2BrN compounds have been theoretically investigated by Dominik *et al.* [60]. Only the electronic and elastic properties have been examined, which limits the scope of this research. It would be beneficial to discuss a few additional crucial features that might increase the variety of possible applications. In terms of applications, dynamic stability

research is essential. Since key phenomena that limit the usage of structural materials, such as fracture initiation, anisotropic plastic deformation and dissemination, and elastic instability, are intimately related to mechanical anisotropy, it is crucial to comprehend this phenomenon.

Mulliken population analysis confirms the coexistence of ceramic and metallic properties in MAX phases. Assessing thermal properties is crucial for predicting suitability in extreme conditions. Optical characteristics of MAX phase compounds are essential for foreseeing applications, like using them as coatings to mitigate solar heating. These analyses inform practical utilization and potential advancements in material applications.

Vickers hardness measures the overall bonding power produced by a solid's bonds. Optically beneficial traditional MAX phase materials exist. As a result, it is expected to demonstrate that the MAX phases are valuable materials for applications involving optical devices. Therefore, it is important to look at the optoelectronic properties of Sc_2AX (M = Bi, Br; X = C, N, B). The present investigation is highly motivated by these issues.

CHAPTER 3
THEORETICAL METHODOLOGY

3.1 Introduction

Our primary objective is to comprehend the behavior of quantum mechanical many-particle systems from an ab initio standpoint, i.e., beginning with the fundamental components and their interactions. DFT is a fantastic quantum mechanical tool to ascertain the structural, electronic and ground state characteristics of molecules and solids [61]. The *ab initio* calculations in this work were performed using the DFT–based Cambridge Serial Total Energy Package (CASTEP) [62]. The electronic exchange and correlation terms were estimated using the Generalized Gradient Approximation (GGA) framework with the Perdew–Burke–Ernzerhof (PBE) [63], and Perdew–Burke–Ernzerhof for solids (PBEsol) [64]. Pseudo–atomic computations were performed on the electronic orbitals of Sc– $3d^1 4s^2$; Bi–$6s^2 6p^3$; Br–$4s^2 4p^5$; B–$2s^2 2p^1$; C–$2s^2 2p^2$; and N–$2s^2 2p^3$ respectively. OTF-Gultra–soft pseudo potential was employed to model the interactions of electrons and ion cores [65]. The Brillouin zone was integrated over using the Monkhorst–Pack (MP) [66]technique in the reciprocal space of the Sc_2AX (A = Bi, Br; X = C ,N, B)hexagonal unit cell using a k–point mesh that was 10×10×2 grid–centered. The plane–wave energy cutoff 500eV was used according to the convergence calculation.

The minimization technique Broyden–Fletcher-Goldfarb–Shanno (BFGS) [67] was employed to accomplish geometric optimizations by minimizing the internal forces and total energy. To achieve excellent convergence, the self–consistent field, total energy, maximum displacement, maximum stress, and maximum force are taken as 5.0×10^{-7}eV/atom, 5.0×10^{-6}eV/atom, and 5.0×10^{-4}, 0.02GPa, and 0.01eV/Å, respectively. Using periodic boundary conditions, the unit cell's total energies were determined. To determine the elastic constants, we applied the "stress–strain" method that is built into the CASTEP program. The estimated elastic constant C_{ij} was used to derive the elastic moduli. The perturbation DFT–based finite displacement super cell approach was used to analyze the phonon dispersions [68]. The quasi–harmonic approximation was employed to calculate the thermodynamic properties from the phonon density of states.

The relevant sections contain brief explanations of the methodology used to investigate the bonding and optical characteristics of theSc_2AX (A = Bi, Br; X = C, N, B) MAX phase compounds. This chapter provides a concise summary of the tools and methodology used in this investigation. It outlines the specific approaches and techniques employed throughout the study.

3.2 *Ab-initio* approach

The *ab initio* approach offers a robust method to derive atomic and molecular structures based on fundamental principles of quantum mechanics. This methodology provides valuable insights that are not reliant on experimental conditions. The term *'ab initio'*, derived from Latin, literally means 'from the beginning', emphasizing its foundation in fundamental principles. One widely employed application of this approach is the study of ground state properties in periodic systems, utilizing solutions to Schrödinger's equation and wave functions.

The HF method is fundamental to ab initio approaches, focusing on the mean field approximation rather than considering instantaneous electron-electron repulsion. Although it is a variational method, computed energies typically tend to slightly overestimate the actual energy due to vibrational effects and the wave function's properties. As the basis set size increases, these computed values approach the Hartree-Fock limit. Initial computations often begin with Hartree-Fock calculations, followed by corrections for electron-electron repulsion such as Møller–Plesset perturbation theory (MPn) and coupled cluster theory (CC) [69,70]. However, the Hartree-Fock approach has notable limitations, particularly in scenarios involving bond-breaking. Post-Hartree–Fock theories often build upon single-determinant reference functions, although methods employing multi-determinant references have also been developed.

Regarding the ab initio method, it allows for the precise determination of both physical and chemical properties in periodic arrangements, starting from a known chemical structure with a stable internal configuration. Importantly, this approach operates independently of any prior knowledge or assumptions.

At its core, this method hinges on expanding the single-valued wave function (crystalline orbital, CO) into Bloch functions, a fundamental approximation in quantum mechanics. These Bloch functions are characterized by a local Gaussian-like form, with coefficients and exponents adjusted based on given input parameters [71]. The *ab initio* approach proves particularly effective for systems where initial assumptions are minimal, offering close approximations to solutions. However, achieving convergence is not always uniform, and in some cases, simpler approaches may yield more accurate results for certain characteristics.

3.3 CASTEP Code

The CASTEP (CAmbridge Serial Total Energy Package) software, developed through first-principles theory including density functional theory (DFT), was collaboratively created by scientists from York, Durham, Cambridge, St. Andrews universities, and Rutherford Labs for parallel computations [72]. This powerful tool can calculate a wide range of solid-state properties, including structural, thermal, optical, mechanical, and electrical characteristics. Additionally, CASTEP enables detailed investigation of wave functions and charge density mappings within systems. It is extensively utilized for studying chemical reactions in bulk materials, surface diffusion processes, and more. Comprehensive documentation on CASTEP can be found elsewhere [72,73]. CASTEP employs a plane-wave pseudopotential method based on DFT, simplifying computations by replacing the total potential accounting for both core and valence electrons with a more theoretically advantageous term. The plane-wave basis set extends electron wave functions, while generalized gradient approximations (GGA) or local density approximations (LDA) are used to compute exchange and correlation effects among electrons. These parameters are crucial for optimizing the geometries of solids, surfaces, molecules, and interfaces. Further physical properties can be derived from simulation results using the methodologies described in subsequent chapters.

3.4 Many-body Problems in Quantum Mechanics

A many-body system, starting from its atomic constituents, can be comprehensively characterized by its electronic structure and atomic configuration, obviating the need for additional exploration variables. In this context, we delve into essential quantum

mechanical principles that form the foundation for solving equations necessary to elucidate material properties.

3.5 Schrödinger Equation

In theory, the characteristics of a system can be determined by solving the quantum mechanical wave equation that describes its dynamics. In the context of non-relativistic systems, this equation is known as the Schrödinger equation [74]. The behavior of such systems, which do not depend on time, is dictated by this fundamental equation

$$\hat{H}\psi = E\psi \qquad \text{……. (3.1)}$$

where Ψ represents the wave function describing the many-electron system, '*E'* denotes the total energy of the system, and *H* denotes the Hamiltonian operator governing the system's dynamics. In the case of a system consisting of N_e electrons and N_n nuclei, the Hamiltonian can be formulated as

$$H = -\frac{1}{2}\sum_{i=1}^{N_e}\nabla_i^2 - \sum_{k=1}^{N_n}\frac{1}{2M_k}\nabla_k^2 - \sum_{i\neq k}^{N_e N_n}\frac{z_k}{|r_i - R_k|} + \sum_{i\neq j}^{N_e N_e}\frac{1}{|r_i - r_j|} + \sum_{k\neq l}^{N_n N_n}\frac{Z_k Z_l}{|R_k - R_l|}$$

……. . . (3.2)

The initial two terms correspond to the kinetic energies of the electrons and nuclei, respectively. The third term accounts for the Coulombic attraction between electrons and nuclei. The fourth and fifth terms depict the repulsive Coulomb interactions between electrons and between nuclei. While the hydrogen atom offers an exact analytical solution, Schrödinger's equation poses a challenge for systems with multiple particles because analytical solutions are generally not feasible. Consequently, approximations become necessary in such cases.

3.6 Density functional theory

Density Functional Theory (DFT) stands as one of the pivotal computational quantum mechanical modeling methods utilized in physics, chemistry, and materials science. It provides a way to investigate the electronic structure (principally the ground state) of many body systems, especially atoms, molecules, and condensed phases. The success

of DFT can be attributed to its balance of accuracy and computational feasibility, making it a widely used tool in the study of electronic properties of matter.

The foundational ideas of DFT were laid down in the 1960s by Pierre Hohenberg and Walter Kohn. Their landmark paper established that all ground-state properties of a many-electron system are determined uniquely by the electron density, rather than the wave function. This was a significant simplification because the electron density is a function of just three spatial coordinates, whereas the wave function is a function of 3N coordinates for an N-electron system. This reduction in complexity is one of the key reasons for DFT's popularity [75].

The central concept of DFT is electron density, which describes the probability of finding an electron at a point r in space. The Hohenberg-Kohn theorems laid the groundwork by proving that:

1. The ground-state energy of a many-electron system is a unique functional of the electron density.
2. The correct ground-state density minimizes this energy function.

DFT has revolutionized the way scientists approach problems in materials science, chemistry, and physics. It allows for the calculation of various properties, including:

- Electronic structure: Understanding the distribution and behavior of electrons in a material.
- Magnetic properties: Investigating the magnetic moments and ordering materials.
- Optical properties: Studying the interaction of materials with electromagnetic fields.
- Mechanical properties: Evaluating the strength, ductility, and other mechanical behaviors of materials.

Density Functional Theory remains a cornerstone of computational material science, providing a powerful framework for understanding and predicting the properties of matter at the atomic scale. Its blend of theoretical elegance and practical applicability ensures that it will remain a vital tool for researchers for years to come.

3.7 Kohn-Sham formulation

The Kohn-Sham (KS) formulation is a cornerstone of Density Functional Theory (DFT), providing a practical approach to solving the many-body problem of interacting electrons in a system. This formulation, developed by Walter Kohn and Lu Jeu Sham in 1965, introduces a set of non-interacting electrons that possess the same ground-state electron density as the actual interacting system. This innovative concept simplifies the complex quantum mechanical problem, making it computationally feasible to study electronic structures of atoms, molecules, and solids. [76]

The central task in the Kohn-Sham formulation is to solve the Kohn-Sham equations, which are self-consistent field equations given by:

$$\left[-\frac{\hbar^2}{2m}\nabla_i^2 + V_{eff}(r)\right]\Psi_i(r) = E_i\Psi_i(r) \quad \ldots\ldots\ldots (3.3)$$

In this formulation, $\Psi_i(r)$ represent the single-electron orbitals, where the ground-state electron density $\rho_o(\mathbf{r})$ is derived from these orbitals. The electron density is computed using the relation:

$$\rho_o(r) = \sum_i|\Psi_i|^2 \quad \ldots\ldots\ldots (3.4)$$

In the Kohn-Sham equations, the effective potential V_{eff}, referred to as the Kohn-Sham potential, represents the interactions between electrons in an average manner. It includes the electrostatic potential generated by all the electrons and the nuclei, thereby simplifying the complex electron interactions into a more manageable form,

$$V_{eff} = V_{XC}(\rho,r) + V_{ext}(r) + \int\frac{\rho(r')}{|r-r'|}dr' \quad \ldots\ldots\ldots (3.5)$$

The Kohn-Sham equations must be solved in a self-consistent manner as

$$V_{eff}(r) = V_{eff}[\rho(r)] \quad \ldots\ldots\ldots (3.6)$$

The KS equations are solved iteratively through the following steps:

- Initial Guess: Begin with an initial guess for the electron density, $\rho(r)$.

- Calculate Effective Potential: Use the guessed density to compute the effective potential $V_{eff}(r)$.
- Solve KS Equations: Solve the KS equations to obtain new KS orbitals $\Psi_i(r)$.
- Update Density: Compute a new electron density from the KS orbitals.
- Check Convergence: Compare the new density with the previous one. If they are sufficiently close, the solution is converged; otherwise, iterate the process.

The Kohn-Sham formulation effectively transforms the many-body problems into a series of single-body problems, each interconnected through the Kohn-Sham effective potential. Because V_{eff} (**r**) depends on the electron density, the resulting eigenvalue problem is nonlinear and must be solved iteratively using a self-consistent field algorithm. This iterative process is depicted in Fig. 3. 1, which outlines the flow chart for the Kohn-Sham equations.

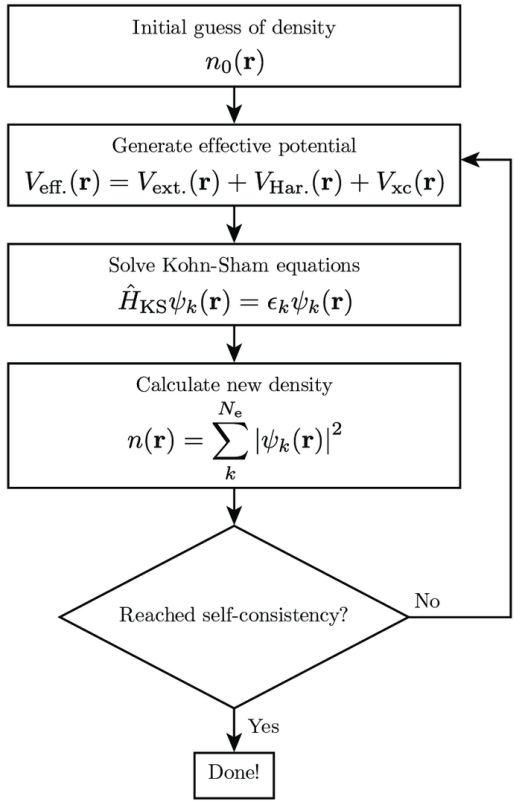

Fig. 3.1: Self-consistent field algorithm for solving the Kohn-Sham equations. [77]

The most computationally demanding step within this iterative loop is solving the Kohn-Sham equation for a given potential (step 2 in the loop). In this step, the equations are solved with a specified V_{in}, yielding an output density ρ_{out}. Once convergence is achieved in the self-consistent loop (as shown in Fig. 3. 1), additional iteration schemes can be employed to further minimize the energy. This may involve adjusting atomic positions or modifying the cell volume.

3.8 Generalized gradient approximation (GGA) –PBE and GGA-PBE$_{Sol}$

In Density Functional Theory (DFT) calculations, the exchange-correlation functional approximation often utilized belongs to the Generalized Gradient Approximation (GGA) class. Two prominent GGA functionals are GGA-PBE and GGA-PBEsol.

GGA-PBE, which stands for Perdew, Burke, and Ernzerhof, is an advanced form of the original GGA proposed by the same authors. In the exchange-correlation functional, GGA-PBE incorporates both the electron density and its gradient. This improvement provides highly accurate results for a wide range of molecules and solids.

GGA-PBEsol [78], on the other hand, is a modified version specifically designed to better describe solid-state systems. It offers improved predictions for structural properties such as lattice constants and bulk moduli. The enhanced exchange factor in GGA-PBEsol addresses the self-interaction error present in the original GGA-PBE, leading to even more accurate results for solids [79].

Both GGA-PBE and GGA-PBEsol are widely applied in computational chemistry and materials science. They are used to study the behavior of molecules, solids, and surfaces, generating reliable results that enhance the understanding of chemical and physical phenomena at the quantum level.

3.9 k-point Sampling

One of the most widely used methods for generating k-points was introduced by Monkhorst and Pack [80]. This approach, which was later adapted to accommodate hexagonal systems [81], creates a uniform grid of k-points along the three axes in

reciprocal space. The Monkhorst-Pack grid is defined by three integers, q_i (where i = 1, 2, 3) representing the number of divisions along each axis.
These integers generate a series of values according to the formula:

$$u_r = (2r - q_i - 1)/2q_i \quad \text{..... (3.7)}$$

where r ranges from 1 to q_i. The resulting Monkhorst-Pack grid is then constructed using:

$$k_{prs} = u_p b_1 + u_r b_2 + u_s b_3 \quad \text{..... (3.8)}$$

This set of q_1, q_2, q_3 distinct points is subsequently symmetrized, and weights are assigned based on the number of symmetry equivalents for each point in the symmetrized set. A constant shift can be applied to all points before summarization, which is particularly useful for hexagonal symmetry systems. For hexagonal systems, the sequence for points along the 'a' and 'b' axes is slightly modified and given by:

$$u_p = (p - 1)/q_i \quad \text{..... (3.9)}$$

where p ranges from 1 to q_i.
This adjustment ensures the k-points are distributed appropriately for hexagonal structures, maintaining the uniformity and efficiency of the Monkhorst-Pack scheme while accommodating the unique geometry of these systems.

3.10 Pseudopotential

An approximate method to describe complex systems involves using pseudopotentials [82]. This approach replaces the Coulomb potential in the Schrödinger equation with an effective potential. The concept of pseudopotentials was first introduced by Hans Hellmann in the 1930s. Thanks to pseudopotentials, the valence wave function remains orthogonal to all core states. This effective potential effectively substitutes for atomic electrons, allowing the pseudo wave function to represent valence electrons accurately. In this method, core electrons are primarily left frozen with the nuclei, focusing on the

chemical valence electrons.

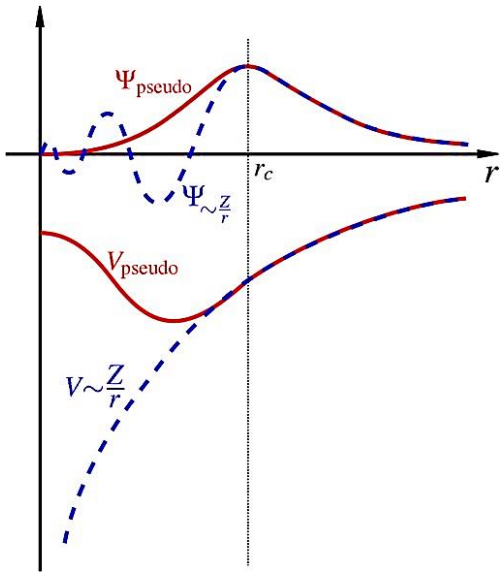

Fig. 3.2 Schematic representation of the all-electron and pseudized wavefunctions and potentials.

By employing pseudopotentials, calculations become more efficient, especially for systems where accurately modeling core electrons would be computationally prohibitive. This method allows researchers to focus on the valence electrons, which are most relevant to the chemical and physical properties of materials.

CHAPTER 4
RESULTS & DISCUSSION

4. Results and discussion

4. 1. Structural properties and stability

4. 1. 1 Structural properties

The ternary MAX phase compounds Sc_2AX (A = Bi, Br; X = C, N, B) belong to the hexagonal crystal structure with space group P_{63}/mmc (No. 194), in which an atomic layer of A (A = Bi, Br) atoms is interspersed between Sc_6X (X = C, N, B) edge shared octahedrons. One Sc atom and three X atoms are stacked to create a tetrahedron along the *a*–axis. Each unit cell of the Sc_2AX phase has two formula units and eight atoms.

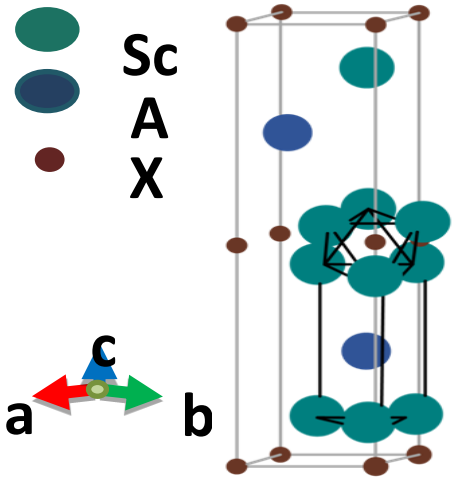

Fig. 4.1: The unit cell structure of Sc_2AX (A = Bi, Br; X = C, N, B) with an edge–shared $[M_6X]$ octahedra and $[M_6A]$ trigonal prism is outlined.

As seen in Fig. 4.1 the Wyckoff positions in the Sc_2AX phase are arranged as follows: The position of the "X" atoms is 2a (0, 0, 0),"A" atoms are 2d (2/3, 1/3, 3/4), and "Sc" atoms is 4f (1/3, 2/3, Z_M), where Z_M is the internal parameter. The structural parameters of the optimized structure are provided in Table 4.1.

The distortion parameters of the unit cell structure are computed using the internal coordinate z_M and the *c/a*. An ideal structure should have a unit (1) octahedron and trigonal parameter ($O_r = P_r = 1$). Any deviation of O_r and P_r from 1 indicates a distortion

in the corresponding polyhedral. Aydin *et al*. [83] suggested that the stability of the structure increases with decreasing distortion.

Table 4.1: Calculated lattice parameters (*a* and *c*), internal parameter (ZM), *c*/*a* ratio, Volume (*V*), the ratio of *O*r and *P*r, and formation energy (E_{for}) of Sc_2AX.

Phase	*a* (Å)	*c* (Å)	Z_M	*c/a*	V(Å^3)	O_r	P_r	O_r/P_r	$E_{\text{for}}(eV/atom)$	Ref.
Sc_2BiC	3.406	14.562	0.081	4.275	146.326	1.16	1.08	1.07	-0.66	This
									-0.67	[60]
Sc_2BiN	3.343	14.268	0.079	4.268	138.118	1.17	1.07	1.09	-1.37	This
Sc_2BiB	3.607	14.493	0.082	4.018	163.292	1.20	1.12	1.07	-0.50	This
Sc_2BrC	3.427	12.853	0.089	3.750	130.698	1.19	1.19	1.00	-1.36	This
									-1.04	[60]
Sc_2BrN	3.350	12.684	0.086	3.786	123.296	1.21	1.18	1.03	-1.79	This
									-1.62	[60]
Sc_2BrB	3.582	13.008	0.092	3.632	144.507	1.19	1.23	0.97	-1.09	This

The octahedral prism (O_r) and trigonal prism (P_r) distortions are calculated as follows [84]:

$$O_r = \frac{\sqrt{3}}{2\left\{4Z_M^2\left(\frac{c}{a}\right)^2 + \frac{1}{12}\right\}^{\frac{1}{2}}}; \text{and } P_r = \frac{1}{\left\{\left(\frac{1}{4} - Z_M\right)^2\left(\frac{c}{a}\right)^2 + \frac{1}{3}\right\}^{\frac{1}{2}}} \quad (4.1)$$

Table 4.1 lists the value of the O_r/P_r ratio for the Sc_2AX phases and shows that the octahedron prism and trigonal prism exhibit roughly identical distortion due to the similar values of the ratios (O_r/P_r). Compared to the Sc_2BiX (X = C, N, B) phases, the Sc_2BrX phases are less distorted since their O_r/P_r ratio is close to 1. With the increase of the valence of the A element, O_r increases, P_r decreases [85].

The formation energy (E_F) of the Sc_2AX phase was calculated to investigate the chemical stability by the following equation [84]:

$$E_{for}^{Sc_2AX} = \frac{E_{total}^{Sc_2AX} - \left(xE_{solid}^{Sc} + yE_{solid}^{A} + zE_{solid}^{X}\right)}{x + y + z}; A = Bi, Br; X = C, N, B \quad (4.2)$$

Where $E_{total}^{Sc_2AX}$ is the total energy of the Sc_2AX Phase and E_{solid}^{Sc}, E_{solid}^{A}, and E_{solid}^{X} indicate the total energy of Sc, A, and X atoms in their solid forms, whilex = 4, y = 2, and z = 2 represent the number of Sc, A, and X atoms for each of the unit cell.

Table 4.2: Some particulars to calculate formation energy E_f.

Phase	Space group	F.E.(eV)	No.of atom	F.E.(eV/atom)
Sc	P4/nmm(129)	-5108.654	4	-1277.164
Sc	$P6_122$ (178)	-7662.529	6	-1277.088
Sc	I4/mcm (140)	-5108.074	4	-1277.019
Bi	$P12_1/m1$ (11)	-614.0997	4	-153.525
Bi	$Pm\bar{3}m$ (221)	-153.494	1	-153.494
Bi	$P12_1/m1$ (11)	-614.0438	4	-153.511
Br	$Pm\bar{3}m$ (221)	-1099.8126	3	-366.6042
Br	Immm (71)	-367.0513	1	-367.0513
Br	I4/mmm (139)	-734.0036	2	-367.0018
C	Pnma (62)	-2476.5	6	-154.7813
C	Cmmm (65)	-618.24	4	-154.578
C	Im3m (229)	-1234.456	8	-154.307
N_2	Pa3 (205)	-2163.986	8	-270.498
N_2	Imma (74)	-1079.929	4	-269.982
N_2	$P4_2/mnm$ (136)	-1081.977	4	-270.494
B	Pnnm (58)	-2160.86	28	-77.174
B	P1 (1)	-923.045	12	-76.921
B	Fm-3m (225)	-922.895	12	-76.908
Sc_2BiC	$P6_3/mmc$ (194)	-5730.426	8	
Sc_2BiN	$P6_3/mmc$ (194)	-5967.748	8	
Sc_2BiB	$P6_3/mmc$ (194)	-5572.476	8	
Sc_2BrC	$P6_3/mmc$ (194)	-6161.872	8	
Sc_2BrN	$P6_3/mmc$ (194)	-6398.222	8	
Sc_2BrB	$P6_3/mmc$ (194)	-6004.4853	8	

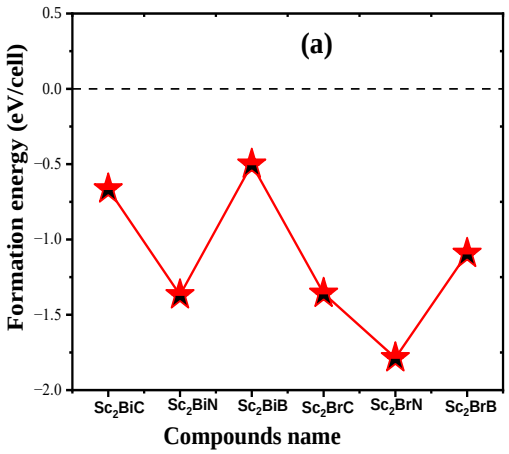

Figure 4.2: Formation energies E_f of Sc_2AX (A = Bi, Br; X = C, N, B) compounds.

Additional details on estimating the formation energy are provided in Table 4.2. The anticipated formation energy of the Sc_2BiC, Sc_2BiN, Sc_2BiB, Sc_2BrC, Sc_2BrN, and Sc_2BrB phases are –0.665eV/atom, –1.368eV/atom, –0.5007eV/atom, –1.776eV/atom, –1.786eV/atom, and –1.0929eV/atom, respectively, which are presented in Table 4.1.

Fig. 4.2 shows that the formation energy values of all the compounds are below the critical line beginning at 0, indicating the phase and chemical stability of the compounds evaluated in this study.

The strength of hybridization within the d orbitals of Sc and others such as the *p* orbitals of A (Bi, Br) or the s and p orbitals of X (C, N, B) will typically have an impact on the formation energies, as well the number of valence electrons filling bonding, nonbonding, or anti–bonded states, as well as the energy needed for the transition metals to expand their volume to accommodate the X elements [48].

4.1.2 The dynamical stability

The dynamical stability of a material is a significant feature that influences its suitability for usage in extreme situations. The phonon dispersion curves (PDCs) calculation for the Sc_2AX (A = Bi, Br; X = C, N, B) phases has been carried out to demonstrate the dynamical stability and vibrational influence on the thermodynamic parameters like Helmholtz free energy, heat capacity, and thermal expansion [86] [presented in 4.5.1].

Fig. 4.3 (a-f) show the PDC and phonon DOS. A compound's stability is determined by the phonon frequency along the entire BZ; positive frequencies imply stability, while negative frequencies signify instability at any specific k-point. It strongly indicates that the Sc_2AX phases are dynamically stable by the absence of negative frequencies in the PDC over the entire Brillouin zone. Each unit cell of the Sc_2AX phase has eight atoms, producing twenty–four vibrational modes, including three acoustic modes (green lines) and the remaining twenty–one optical mode (blue lines).

To better understand the bands by comparing the peaks, the phonon density of states (PHDOS) of the Sc_2AX (A = Bi, Br; X = C, N, B) MAX phases are shown on the right side together with the PDCs. As seen in Figs. 4.3 (a-f), the bands attributed to the Transverse Optical (TO) are flat and produce substantial peaks in all phases, whereas the bands attributed to the Longitudinal Optical (LO) generate modest peaks.

The partial PHDOS also displays the contributions from various atoms, and it is evident that the X (X = C, N, B) atoms are responsible for the upper optical modes. The A (A = Bi, Br) atoms are responsible for intermediate dispersions of the optical branches. The 'Sc' atoms are accountable for the modes in the bottom optical branches and are credited with creating the acoustic modes.

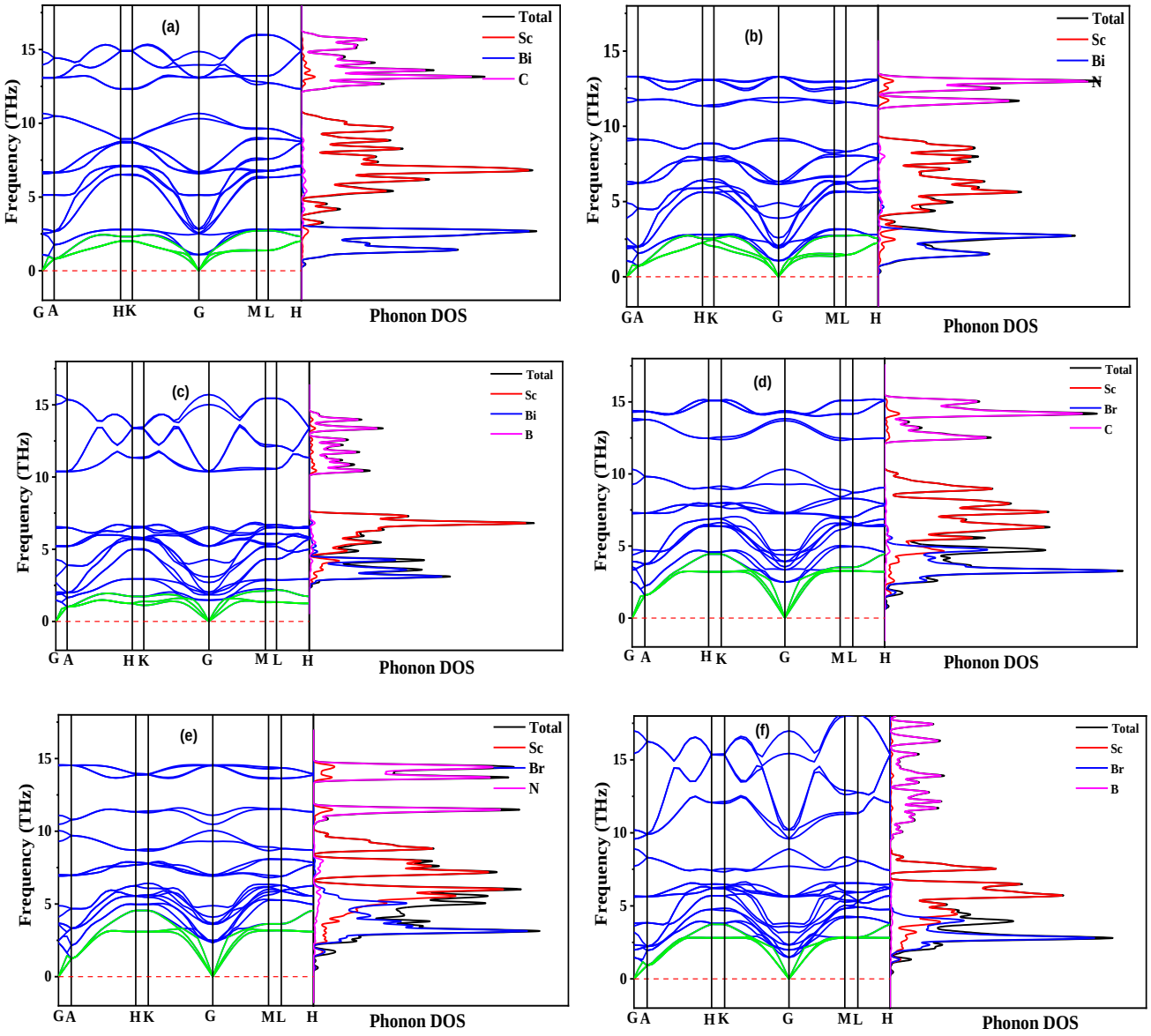

Fig. 4.3: Phonon DOS and phonon dispersion curves of Sc_2AX (A = Bi, Br; X = C, N, B) compounds.

4.2. Electronic properties

4.2.1. Band structure

The electronic band structure (EBS) provides information to comprehend the electronic properties of the Sc_2AX compounds. The band structure of studied compounds has been calculated along high–symmetry *k*–points in the first Brillouin zone shown in Figs. 4.4 (a-g). The Fermi level (E_F) was located at zero-energy level. The valence and conduction bands overlapped at E_F, indicating the metallic nature of them except for the Sc_2BrB phase.

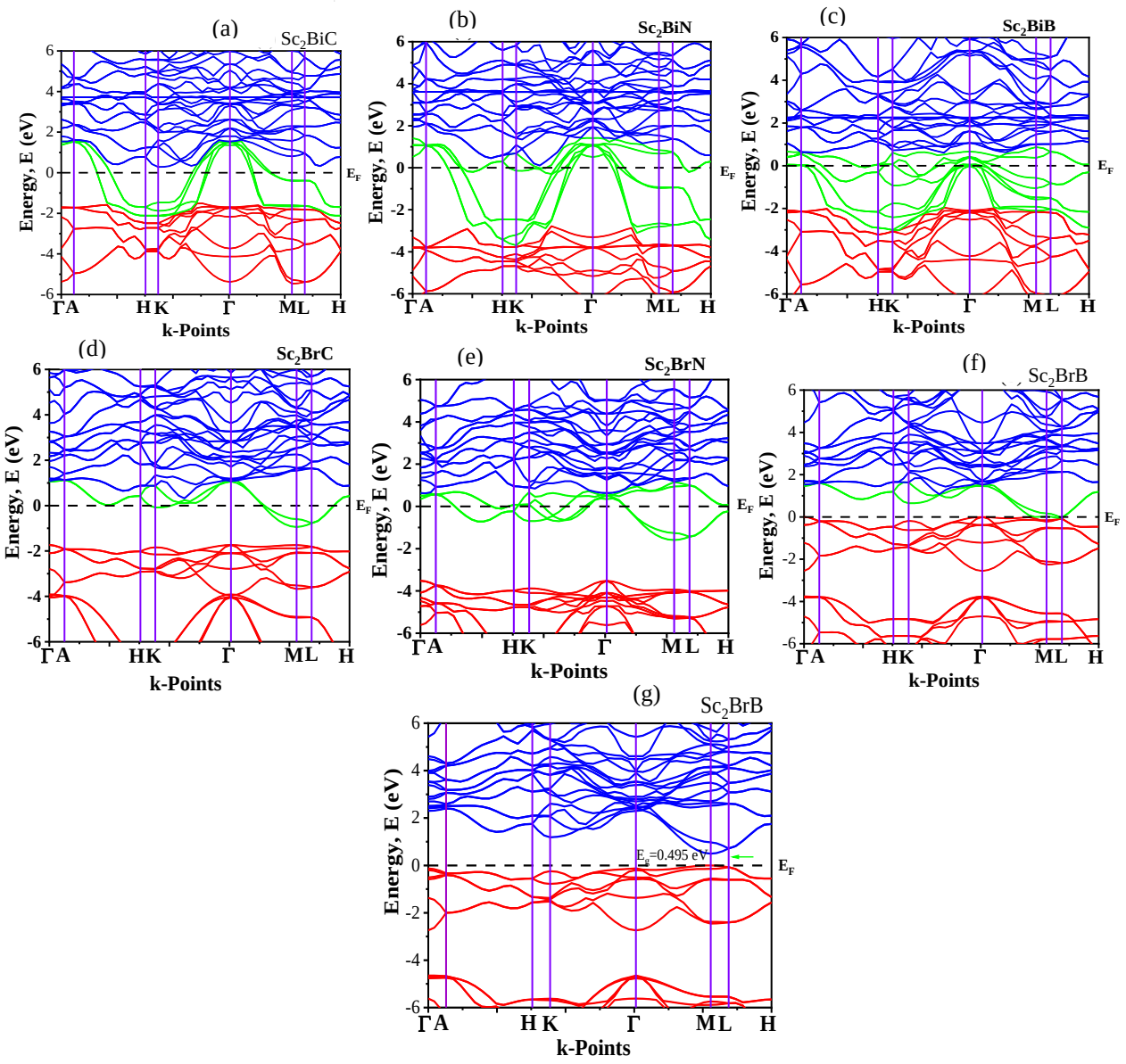

Fig. 4.4: Band structure of (a-f) Sc_2AX (A = Bi, Br; X = C, N, B) compounds; calculated using GGA PBEsol and (g) Sc_2BrB calculated using HSE06.

The energy dispersion along the A–H, K–Γ, Γ–M, and L–H directions are in the basal (*ab*) planes, while the energy dispersion along the Γ–A, H–K, and M–L directions are in the *c*–direction. The lines Γ–A, H–K, and M–L (*c*–direction) exhibit less energy dispersion than the pathways A–H, K–Γ, Γ–M, and L–H (basal plane), as seen in Figs. 4.4 (a-g). Diminished energy dispersion is a consequence of the greater electronic effective mass tensor, resulting in reduced conductivity, and vice versa. The electronic anisotropy of the Sc_2AX MAX phases is indicated by the lower energy dispersion in the *c*-direction caused by higher effective mass, similar to other MAX phases $(Ti_{1-x}Mo_x)_2AlC$ $(0 \leq x \leq 0.20)$ [87]. For Sc_2BrB phase, the conduction band minimum (CBM) and valence band maximum (VBM) merely touched the E_F without overlapping, as shown in Fig. 4.4 (f), certifying the semi–metallic character of it. The nonlocal functional HSE06 [88] was used to calculate the electronic properties of Sc_2BrB phase. The HSE06 hybrid functional
includes a fraction of exact exchange from Hartree-Fock theory, which addresses the typical underestimation of band gaps found with GGA PBEsol functional. Consequently, HSE06 is particularly useful for examining materials where accurate band gap values are critical [88]. The obtained result indicates thatSc_2BrB is a direct band gap semiconductor with a band gap of ~0.495 eV, as shown in Fig. 4. 4(g). Noted that Sc_2BrB is the first semiconductor compound to enrich the MAX phase family.

4.2.2. Density of states (DOS)

The total and partial DOS of Sc_2AX (A = Bi, Br; X = C, N, B) phases have also been computed to investigate the bonding nature and the different electronic states' contributions to electronic conductivity and depicted in Figs. 4.5(a-g). Like other MAX phase compounds, the *d*–orbital of 'Sc' provides the largest contribution to the TDOS (total DOS) at the Fermi level. The *d*–reverberation in the surrounding area of E_F and the non–zero value of the TDOS at E_F demonstrate the metallic nature of the Sc_2AX phase, a conventional feature of MAX phases [2]. According to Figs. 4.5 (a-f) the TDOS, $N(E_F)$, value at Fermi level (E_F) for Sc_2BiC, Sc_2BiN, Sc_2BiB, Sc_2BrC, and Sc_2BrN are 2.67, 4.34, 3.85, 3.63, and 2.13 states/eV–uc, respectively. In addition, the partial DOS confirms hybridization among the different electronic states. There are two major parts in the valence band of Sc_2AX phases. The lower energy range is between -

7to -1 eV for Sc_2BiX and -7 to -3 eV for Sc_2BrX (X = C, N, B) compounds containing a flat region and a distinct peak.

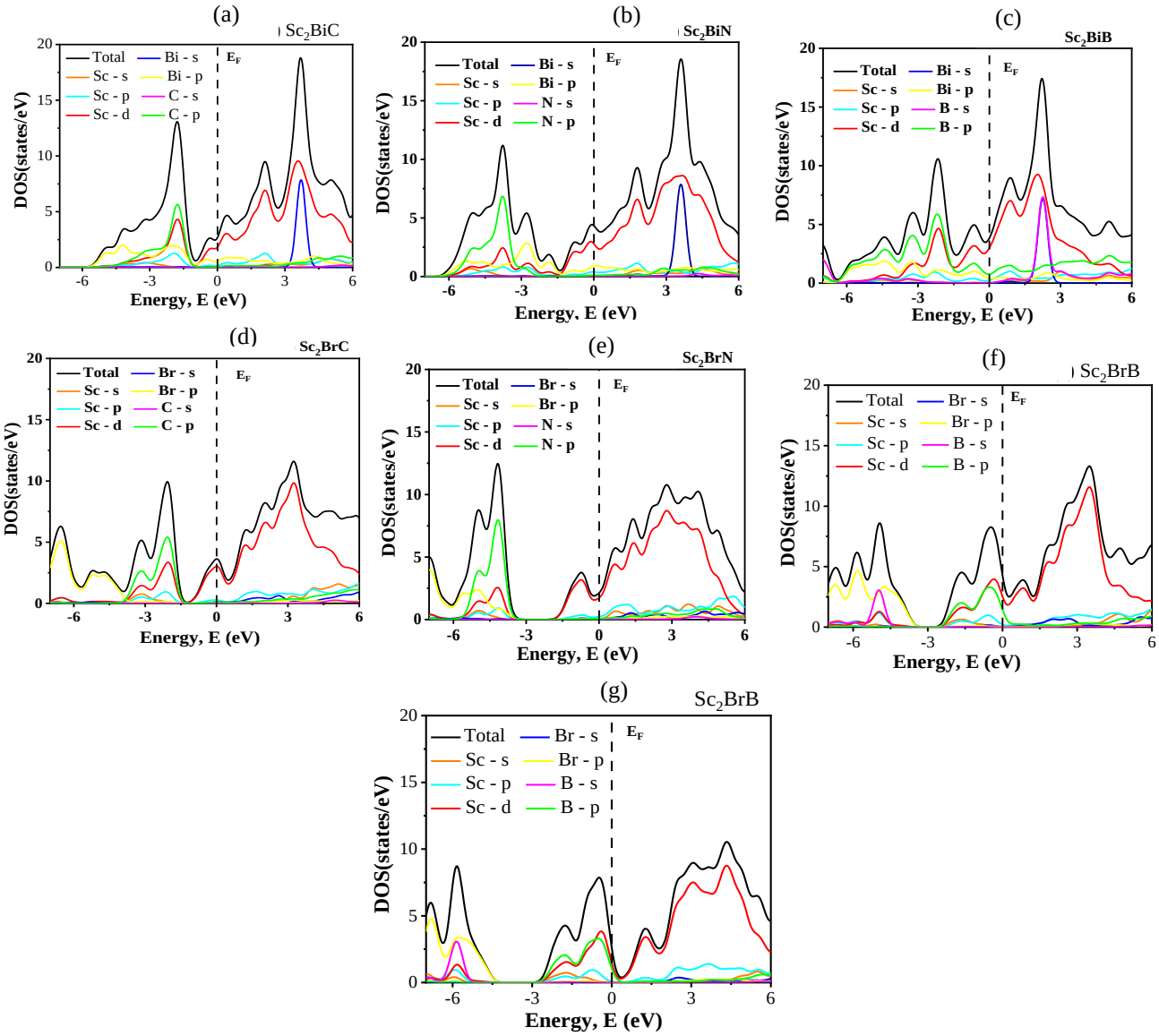

Fig. 4.5: Total and partial DOS of (a-f) Sc_2AX (A = Bi, Br; X = C, N, B) compounds; calculated using GGA PBEsol and (g) Sc_2BrB calculated using HSE06.

The peak originated in this range by the hybridization of Sc–*d* and X–*p* orbitals. Hybridization results ina Sc–B covalent bond in the upper energy region, which exhibits

features different from conventional MAX phases. Particularly, the Sc–*d* and X–*p* (X = C, N, B) hybridization peak for the other studied phases is in the lower energy range, indicating strong covalent Sc–X bonding. The positions of the peaks illustrate how strongly the bonds between the states are held; the lower energy region peak has a stronger bonding strength [87].

Due to E_F's proximity to the pseudo gap, the compound's structural stability is increased. Based on the positions of E_F and the pseudo gap for all the compounds studied, the stability of the structure should be in the following order: Sc_2BiC > Sc_2BiB > Sc_2BrN > Sc_2BiN > Sc_2BrC > Sc_2BrB. All this information demonstrates that the strongest Sc–*d,* and X–*p* covalent bond causes the Sc_2AX phases to have improved Vickers hardness [presented in 4.3.4] and bulk modulus. The findings of this study are consistent with the obtained results of the Sc_2InC, Sc_2AlC, Sc_2AlN, and Sc_2SnCcompounds and also the conventional MAX phase [48,52,54].

4.2.3. Charge density mapping (CDM)

The charge density mapping in the [101] crystallographic plane has been determined in contour form (in units of e/Å^3) to explore the chemical bonding between different atoms in the Sc_2AX phases, illustrated in Fig. 4.6. The high (low) levels of electronic charge density are represented by the red (blue) colors on the adjacent scale. The main characteristic of this mapping is the electron densities brought on by various chemical bonds in the compounds. Strong accumulation zones indicated a sign of the formation of strong covalent bonding. Additionally, the presence of ionic bonding is suggested by the detection of balanced positive or negative charges at the atomic locations [89]. It is clear from looking at the contour map that areas of significant charge accumulation are found where the X and Sc atoms are located. This finding indicates the presence of strong covalent bonds between X–Sc atoms on the upper and bottom positions of the crystallographic surface. In addition, the second covalent bond between A and Sc atoms is seen at the center of the plane, albeit it is significantly weaker than the X–Sc bond.

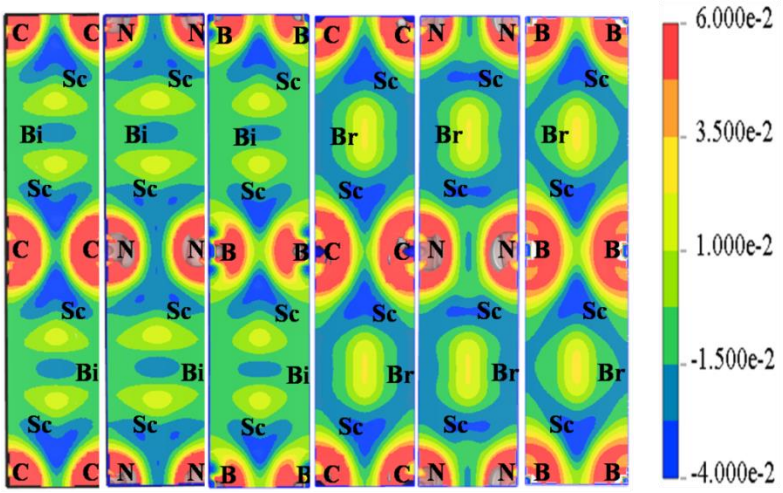

Fig. 4.6: CDM of Sc_2AX (A = Bi, Br); (X = C, N, B) compounds.

Furthermore, the C/N/B atoms close to 'Sc' exhibit tendencies of charge balancing together with a minimal amount of ionic bonding. The Sc_2AX phases are, therefore, expected to have a mixture of covalent and ionic bonding.

4.3. Mechanical behavior

4.3.1. Elastic properties

MAX phases, fascinating materials with a distinctive blend of metallic and ceramic characteristics, depend heavily on their mechanical properties. These characteristics, such as toughness, stiffness, and elastic modulus, directly impact how well they work and are applicable in various fields, including cutting, aerospace, and automotive manufacturing equipment. Initially, the mechanical characteristics of the Sc_2AX (A = Bi, Br; X = C, N, B) phases were studied by calculating the elastic constants (C_{ij}) using the stress–strain technique [90,91] and presented in Table-2 alongside previous data where available. Six stiffness constants (C_{11} to C_{66}) are introduced by the hexagonal crystalline structure of the Sc_2AX phases, five of which are independent because C_{66}= (C_{11}-C_{12})/2 [92]:

Before considering the materials for structural applications, it is essential to evaluate the mechanical stability using elastic constants (C_{ij}). Conditions that guarantee the stability of a hexagonal system included in below [93]:

$$C_{11} > 0, C_{33} > 0, C_{44} > 0, C_{11} - C_{12} > 0, (C_{11} + C_{12})C_{33} - 2C_{13}^2 > 0 \quad (4.3)$$

The values shown in Table-4.3 satisfy these requirements, making the studied MAX compounds mechanically stable. The responses of the materials to various directions of applied stress are reflected in these constants. C_{11} and C_{33} expressly represent stiffness along the [100] and [001] axes, respectively, whereas C_{44} describes resistance to shear deformation in the [100] plane.

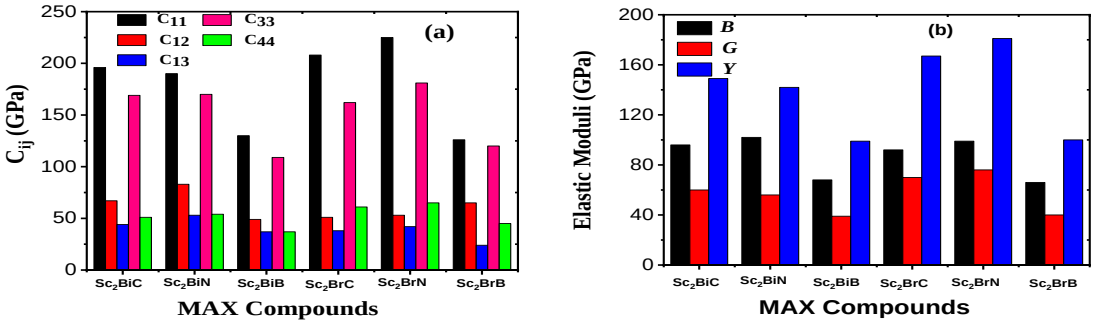

Fig. 4.7: The stiffness constants (a) and (b) elastic moduli of Sc_2AX.

Remarkably, C_{11} and C_{33} have higher values than C_{44}, indicating that shear deformation is preferable to unidirectional deformation for these compounds. The stiffness from chemical bonding along the *a*– and *c*–axes, respectively, is correlated with the elastic constants C_{11} and C_{33}, similar to the previous MAX phases, with C_{11} being higher than C_{33} [54,94]. According to this difference, these components are easily deformable along the *c*–axis rather than the *a*–axis, as seen in Fig. 4.1, where bonding connections along the *a*–axis are stronger because they have shorter bond lengths than those along the *c*–axis. The disparities between C_{11} and C_{33} also revealed the anisotropic bonding strength along the *a*– and *c*–axes, as other 211 phases, such as F_2CuB and F_2ZnB ($C_{11} > C_{33}$)exhibits the similar nature [95].

Table 4.3: The stiffness constants C_{ij} (GPa), fracture toughness (K_{IC}) (MPa.m$^{1/2}$), machinability (U_m), and brittleness index (M_B)(μm$^{-1/2}$) of Sc_2AX.

Parameters	Sc_2BiC	Sc_2BiN	Sc_2BiB	Sc_2BrC	Sc_2BrN	Sc_2BrB	Sc_2AlC	Sc_2AlN
C_{11}	196.28	190.45	130.18	208.15	225.25	126.48	179.23[a]	210.27[a]
C_{33}	169.36	170.19	108.87	162.08	180.74	120.33	194.46[a]	217.66[a]
C_{44}	51.08	53.74	37.06	61.07	65.12	44.52	45.18[a]	70.88[a]
C_{12}	67.32	83.92	49.44	51.32	52.92	64.89	65.34 [a]	69.59[a]
C_{13}	43.55	53.09	36.93	37.68	42.08	23.80	34.21[a]	54.007[a]
U_m	1.88	1.91	1.83	1.49	1.53	1.48	1.839 [a]	1.388[a]
K_{IC}	1.23	1.22	0.85	1.27	1.37	0.83	1.098[a]	1.431[a]
M_B	7.79	6.02	7.02	11.32	11.02	8.12	8.052[a]	11.16[a]

[a] Reference [48]

Furthermore, compared to the other elastic characteristics, C_{44} exhibits the best association with shear modulus, making it a superior predictor of hardness [96]. A low C_{44} value relates to a compound's better machinability since it shows a higher shear ability and reduced hardness. Hence, it is anticipated that Sc_2BrN would demonstrate the highest hardness attributed to its superior C_{44} (65.12 GPa) value, while Sc_2BiB is expected to be the least hard due to its lower C_{44} (37.06 GPa) value. Notably, Sc_2AlN [48]and Y_2SB [97]exhibit a notably higher C_{44} (70.88 GPa) and C_{44} (63.5 GPa) value compared to Sc_2BiB. This suggests that Sc_2BiB may offer enhanced machinability and shear ability relative to the other compounds, based on these findings.

The bulk modulus (B) and shear modulus (G) of the materials were calculated according to the Voigt [98] and Reuss [99]models using Hill's approximation [100]. The following equations are used for the calculations:

$$B = \frac{(B_V + B_R)}{2} \quad \text{..... .} \quad (4.4)$$

$$Where, B_V = \frac{[2(C_{11} + C_{12}) + C_{33} + 4C_{13}]}{9}; and\ B_R = \frac{C^2}{M}$$

$$C^2 = (C_{11} + C_{12})C_{33} - 2C_{13}^2; \text{and } M = C_{11} + C_{12} + C_{33} - 4C_{13}$$

The upper and lower limits of the bulk modulus, B, are denoted by the terms Voigt bulk modulus (B_V) and Reuss bulk modulus (B_R), respectively. The same process is used to

get shear modulus, *G*:

$$G = \frac{G_V + G_R}{2} \quad \ldots\ldots\ldots\ldots\ldots \quad (4.5)$$

$$Where, G_V = \frac{(M + 12C_{44} + 12C_{66})}{30}; \text{and } G_R = \frac{\left(\frac{5}{2}\right)[C^2 C_{44} C_{66}]}{[3B_V C_{44} C_{66} + C^2(C_{44} + C_{66})]}.$$

Additionally, *B* and *G* can be used to calculate Young's modulus (*Y*) and Poisson's ratio (ν) [101]:

$$Y = 9BG/(3B + G); \text{ and } v = (3B - Y)/(6B) \quad \ldots\ldots\ldots\ldots\ldots \quad (4.6)$$

A solid material's compressibility is determined by its bulk modulus (*B*), with higher *B* values indicating lesser compressibility under hydrostatic pressure. Larger *G* values indicate higher shear resistance, and the shear modulus (*G*) measures a solid's resistance to deformation under shearing force. As opposed to this, Young's modulus (*Y*) assesses the stiffness of materials under uniaxial stress in all directions, with higher (*Y)* values denoting more stiffness. When selecting a material for a thermal barrier coating (TBC), a crucial factor is the thermal shock resistance *R*, which is inversely related to *Y* [102]. The Young's modulus (*Y)* values of the mentioned compounds align closely with that of Sc_2AlC (*Y* = 133.4 GPa) [48], Sc_2SB(*Y* = 151.9 GPa) [97], $Y_4Al_2O_9$ [103], a recognized material for thermal barrier coatings (Y = 190 GPa) [79]. This suggests that Sc_2BiC (*Y* = 148.7 GPa), Sc_2BiN (*Y* = 142.0 GPa), Sc_2BrC (*Y* = 166.6 GPa), and Sc_2BrN (*Y* = 180.9 GPa) hold promise as potential alternatives for thermal barrier coating applications. Table 4.4 clarifies that Sc_2BiB (*Y* = 98.6 GPa) and Sc_2BrB (*Y* = 100.2 GPa) have the lowest *Y* values of all the phases. Due to their increased thermal shock resistance, Sc_2BiB and Sc_2BrB have become potential options for TBC materials.

Table 4.4: Bulk moduli *B* (GPa); shear moduli *G* (GPa); Young's modulus *Y*(GPa), macro hardness (H_{macro}), micro hardness (H_{micro}),Pugh's ratio (*G*/*B*) and Poisson's ratio (*v*), *f*– index, radiation factor $\left(\sqrt{G/\rho^3}\right)$(m^4/Kg.s), acoustic impedance (Z)(Rayl) of Sc_2AX (A = Bi, Br; X = C, N, B) MAX phases.

Parameters	Sc_2BiC	Sc_2BiN	Sc_2BiB	Sc_2BrC	Sc_2BrN	Sc_2BrB	Sc_2AlC	Sc_2AlN
B	96.1	102.8	67.9	91.5	99.9	65.7	86.1	102.3
	100.1 [b]			94.4 [b]	113.1 [b]		91.1 [a]	110.4 [a]
G	59.9	55.9	39.2	69.6	75.5	40.2	109.7	78.8
	56.0 [b]			64.0 [b]	69.4 [b]		111.7 [a]	72.9 [a]
Y	148.7	142.0	98.6	166.6	180.9	100.2	133.4	188.2
	141.6 [b]			156.6 [b]	172.8 [b]		139.5 [a]	179.4 [a]
v	0.25	0.27	0.26	0.20	0.20	0.25	0.24	0.19
	0.26 [b]			0.22 [b]	0.24 [b]		0.24 [a]	0.23 [a]
H_{macro}	9.59	7.33	5.99	14.39	15.09	6.76		
H_{micro}	9.82	8.62	6.32	14.12	15.20	6.65		
	8.80 [b]			11.79 [b]	11.78 [b]			
G/B	0.623	0.544	0.577	0.761	0.756	0.611	0.624	0.770
f	1.40	1.44	1.47	1.47	1.40	1.49	1.059[a]	0.994[a]
$\sqrt{G/\rho^3}$	0.41	0.36	0.39	0.84	0.79	0.75	1.391[a]	1.16[a]
$Z \times 10^6$	20.56	20.52	15.72	17.94	19.34	12.92	12.76[a]	16.23[a]

[a] Reference [48], [b] Reference [60]

The ductility or brittleness of the solids can be studied using the calculated values of Young's modulus (*Y*), bulk modulus (*B*), and shear modulus (*G*). The brittleness or ductility of the compounds is determined using Pugh's ratio *G/B*, where *G/B* > 0.57 suggests brittleness and *G/B* < 0.57 indicates ductility [104]. In addition, Poisson's ratio (*v*) can foretell a material's brittleness or ductility. Frantsevich *et al.* [105] state that a substance is brittle if its Poisson's ratio is less than 0.26 and ductile if it surpasses this threshold. According to the present study, Sc_2BiN and Sc_2BiB are ductile compounds, but the remaining phases are brittle, as shown in Table 4.3. While Sc_2BiN, Sc_2BiB, and Sc_2BrB phases have never been reported, the values found for Sc_2BrC and Sc_2BrN accord well with those previously reported by Dominik *et al.* [60] (represent in Table

4.4). While MAX phases are generally characterized by their brittle nature, certain specific MAX phases demonstrate ductility. Notable examples include Zn_2GaB (ν = 0.273), Mo_2GaB (ν = 0.276), Sc_2SB (ν = 0.27), Y_2SB (ν = 0.277), and Sc_2GaB (ν = 0.275) [97,106,107]. These compounds exhibit ductile behavior, corroborating findings from this studies Sc_2BiN (ν = 0.27) and Sc_2BiB (ν = 0.26) that highlight their exceptional mechanical properties.

In addition, Poisson's ratio offers crucial new information about the inter-atomic forces that keep crystal structures stable. Poisson's ratio values for Sc_2BiC, Sc_2BiN, Sc_2BiB, and Sc_2BrB phases range from 0.25 to 0.50, demonstrating central forces supporting their crystal structures. Poisson's ratio of the other phases, Sc_2BrC and Sc_2BrN, fall outside of this range (below 0.25 or above 0.50), indicating the contribution of non–central forces to stabilize their crystal structures [108].

Machinability is a crucial determinant of a material's performance, which has been calculated using the following formula [50]:

$$U_M = B/C_{44} \quad \text{……} \quad (4.7)$$

Where, B stands for the bulk modulus. Table 4.3 provides the $U_M$values for all compounds, and the following is a ranking of machinability: Sc_2BrB > Sc_2BiB > Sc_2BiC > Sc_2BiN > Sc_2BrN > Sc_2BrC. Sc_2BrC demonstrated the lowest U_M as anticipated to its largest C_{44} value. It's important to note that the variance in B and C_{44}values accounts for the difference in U_M values. Nevertheless, the reported U_M values are equivalent to those of other 211 MAX phases, including Ti_2AlC [109], which has a machinability index of 1.23. Although other 211 phases, such as W_2SnC (U_M = 33.3) and Mo_2PbC (U_M = 15.8), have extremely high U_M values, these phases' have very low C_{44} values (6 GPa for W_2SnC and 10 GPa for Mo_2PbC) [16,50].

Fracture toughness (K_{IC}), which gauges the ability of a material to resist crack extension, is another essential factor. TheK_{IC} of Sc_2AX compounds (A = Bi, Br; X = C, N, B) was calculated using the following formula [110]:

$$K_{IC} = V_0^{1/6} G (B/G)^{1/2} \quad \text{……} \quad (4.8)$$

According to the K_{IC}values listed in Table-4.3, Sc_2BrN has a stronger resistance to crack extensions than the other compounds. Sc_2BrN is found to have the highest K_{IC} value (1.37 MPa $m^{1/2}$), which is much less than the values for other MAX phases, including Ti_3SiC_2 (7.0 MPa $m^{1/2}$), Ti_2AlC (6.5 MPa $m^{1/2}$), Ta_2AlC (7.7 MPa $m^{1/2}$), andV_2AlC (5.5 MPa $m^{1/2}$) [111].

The brittleness index (M_B), which is related to hardness (H_V) and Fracture toughness K_{IC}, to better understand the resistance to deformation or damage tolerance [112] has been calculated as follows [113]:

$$M_B = \frac{H_V}{K_{IC}} \quad \text{…… (4.9)}$$

Where H_V is the Vickers Hardness represented by Chen's formula [113]. While M_B measures a material's damage tolerance, K_{IC} assesses a material's resistance to fracture. Better damage tolerance is indicated by a lower $M_B$value. Table 4.3 lists the M_B values for the Sc_2AX compounds, in which Sc_2BiN (M_B = 6.02) shows the low value and exhibit the substantially higher damage tolerance than all other studied phases.

The hardness parameter and the value of C_{44} are directly related, as was already indicated. The results reported in Tables 4.3 and 4.4 clearly show that a higher C_{44} value denotes a greater hardness parameter (H_{macro} &H_{micro}) [112,114]. The hardness of Sc_2AX was determined using the formulae and listed in Table 4.4.

$$H_{macro} = 2[(G/B)^2G]^{0.585} - 3; \quad and\ H_{micro} = \frac{(1-2\upsilon)Y}{6(1+\upsilon)} \quad \text{…… (4.10)}$$

Among all the compounds under investigation, the computed values for H_{micro} obtained for Sc_2BiC, Sc_2BrC, and Sc_2BrN correspond well with previously published data by Dominik *et al.* [60], which is displayed in Table 4.4. Meanwhile, other Sc_2BiN, Sc_2BiB, and Sc_2BrB phases lack any previous reports. According to the obtained H_{macro} value Sc_2BrN (H_{macro} = 15.09GPa) is predicted to be the hardest compound among the studied phases, whilst Sc_2BiB displays the lowest value (H_{macro} = 5.99

GPa). Vickers hardness (H_V) [presented in Table-4.6], which is believed to be more accurate, particularly for partially metallic systems like MAX phases, [115,116]. Mourad Rougab *et al.* [117] calculated the Vickers hardness for the F_2CuB and F_2ZnB phases, obtaining values of 5.08 and 9.00, respectively, through a semi-empirical method. These compounds exhibit lower hardness compared to the macro hardness (H_{macro}), & micro hardness (H_{micro}) of the studied Sc_2AX phases and higher hardness compared to Vickers hardness(H_V) that computed by the Mullican population approach. It's remarkable that the results of(H_V)differ for using different method.

The f–index, which is calculated by contrasting linear compressibility towards the *a*– and *c*–axes, is an important variable that aids in determining the bonding strength and anisotropic behavior along these axes [16].

$$f = \frac{(C_{11} + C_{12} - 2C_{13})}{(C_{33} - C_{13})} \qquad \ldots\ldots\ldots \quad (4.11)$$

A value of '*f*' is greater (lower) than 1, indicating stronger chemical bonding in the '*ab*' plane along the *c*-direction as evident in Table 4. 4. A weaker bonding in the *c*-direction implies the possibility of chemical exfoliation to derive 2D MXene materials, which is also observed for all compounds studied here. Chemical solutions have previously been utilized in experiments to exfoliate Ti_2AlC, resulting in the formation of the 2D Ti_2C system [118,119]. Given this precedent, we predict that Sc_2AX compounds, with '*f*' values ranging from 1.40 to 1.49, would serve as optimal candidates for experimental exfoliation, particularly since Ti_2AlC (*f* =1.174) has already been successfully exfoliated.

4.3.2. Acoustic behavior

Determining a material's acoustic impedance concerning its surrounding medium is crucial for designing effective transducers and providing noise reduction. At their contact, the differences in acoustic impedance between the two materials have a significant impact on the transfer of sound and reflection. Higher sound transmission happens when the acoustic impedances of two materials are close to one another while sound is transmitted between them. Most of the sound will be reflected, though, if the

impedances are sufficiently different. The material's mass density (ρ) and shear modulus (G) can be used to represent acoustic impedance (Z) as the following equation:

$$Z = \sqrt{\rho G} \quad \ldots\ldots\ldots\ldots \quad (4.12)$$

The potential for extraordinary applications becomes apparent for materials with increasing densities and shear moduli.

The sound radiation intensity is very important in situations where soundboards are used, notably in musical instruments. The radiation factor, often known as ($\sqrt{G/\rho^3}$), is a desirable property for materials used in instruments. The following equation denotes the relationship between the sound intensity of radiation (I) and the density and stiffness of the material [100].

$$I = \sqrt{G/\rho^3} \quad \ldots\ldots\ldots\ldots\ldots\ldots \quad (4.13)$$

Advanced materials research in this field is concentrated on creating substances with appropriate acoustic characteristics. For the Sc_2AX phases, the results demonstrated in Table 4. 4 suggest attractive prospects for soundboard applications.

4.3.3. Mulliken atomic population

Mulliken population data analysis for non–magnetic systems provide Mulliken charges, Hirshfeld charges, and Mulliken bond populations. The CASTEP code projects the surface wave states via a localized basis employing the technique proposed by Sanchez–Portal *et al*. [120]. The Mulliken technique's framework is then utilized to perform a population analysis [121]. The following formulas can be used to determine the Mulliken charge that corresponds to an atomic species "A":

$$Q(A) = \sum_k \omega_k \sum \sum_{\mu}^{on\ A} \sum_v P_{\mu v}(K) S_{\mu v}(K) \sum \quad \ldots\ldots\ldots\ldots \quad (4.14)$$

Where $P_{\mu v}$ denotes the density matrix and $S_{\mu v}$ denotes the overlap matrix. Two atoms *A* and *B*'s united bond population can be determined as:

$$P(AB) = \sum_k \omega_k \sum \sum_{\mu}^{on\ A} \sum_v^{on\ B} 2P_{\mu v}(K) S_{\mu v}(K) \quad \ldots\ldots\ldots\ldots\ldots\ldots (4.15)$$

The finding of positive and negative Mulliken charges in Table-4.5 denotes electron gain and loss, respectively. In this case, positive Mulliken charges on Sc and Br atoms

indicate electron loss during bonding, while negative Mulliken charges on Bi and X (X = C, N, B) atoms indicate electron gain. This information implies that X atoms (C, N, B) are more effective at absorbing electrons than Bi atoms during bonding, while Br atoms are more likely to lose electrons than Sc atoms. The difference between the Mulliken charges and the formal ionic charges on the anion species can be used to study the nature of chemical bonding and the strength of these bonds. The effective valence charge (EVC) can be determined using this discrepancy. An ionic bond would have an EVC value of zero, whereas rising covalency would be demonstrated by values greater than zero. It is readily apparent the bonding between the atoms involves a significant amount of covalence based on the calculated EVC values for the examined Sc_2AX phases displayed in Table 4.5. The following result suggests that these chemical bonding are more covalently strong. The bond population demonstrates bond covalence, which also shows how electron densities are distributed inside the compounds.

The Sc_2AX phase's estimated Bond Overlap Population (BOP) is shown in Table 4.5. It has been discovered that a low population overlap and a high amount of ionicity are related. In contrast, a high value denotes a high degree of covalence in the chemical interaction [122]. The positive and negative BOP are caused by the bonding and anti–bonding states, respectively [76]. It has been noted that B–Sc bonds are seen to be more covalent in the Sc_2BrB phase than the other. In the present research, it is seen that Sc_2BiC, Sc_2BiN, and Sc_2BiB phases all display positive BOP, whereas Sc_2BrC, Sc_2BrN, and Sc_2BrB phases demonstrate both positive and negative BOP. The Sc–Br bond has a high negative BOP in the Sc_2BrN phase, whereas the identical bond is seen with a modest negative BOP in the Sc_2BrC and Sc_2BrB phases, respectively.

Table 4. 5: Mulliken population analysis of Sc_2AX phases.

Phases	Atoms	Mulliken atomic population					Effective valance charge
		s	P	d	Total	Charge (e)	
Sc_2BiC	C	1.50	3.31	0.00	4.81	–0.81	–
	Bi	1.82	3.32	9.99	15.13	–0.13	4.87
	Sc	2.25	6.63	1.65	10.53	0.47	2.53
Sc_2BiN	N	1.71	4.08	0.00	5.78	–0.78	–
	Bi	1.80	3.32	9.99	15.11	–0.11	4.89
	Sc	2.23	6.60	1.73	10.55	0.45	2.55
Sc_2BiB	B	1.25	2.51	0.00	3.76	–0.76	–
	Bi	1.85	3.27	9.99	15.11	–0.11	4.89
	Sc	2.28	6.66	1.63	10.56	0.44	2.56
Sc_2BrC	C	1.49	3.31	0.00	4.80	–0.80	–
	Br	1.62	5.24	0.00	6.86	0.14	6.86
	Sc	2.35	6.63	1.70	10.67	0.33	2.67
Sc_2BrN	N	1.70	4.08	0.00	5.78	–0.78	–
	Br	1.73	5.22	0.00	6.95	0.05	6.95
	Sc	2.29	6.56	1.79	10.64	0.36	2.64
Sc_2BrB	B	1.20	2.58	0.00	3.78	–0.78	–
	Br	1.51	5.25	0.00	6.77	0.23	6.77
	Sc	2.41	6.69	1.63	10.73	0.27	2.73

Therefore, it may conclude that the anti–bonding states in the Sc_2BrX phase are mainly responsible for the same negative Sc–Br bond. The chemical bonds in Sc_2AX phases can be evaluated for metallicity(fm) using the following formula [123]:

$$fm = \frac{P_{\mu'}}{P_{\mu}} \quad \ldots\ldots\ldots \quad (4.16)$$

Investigating metallicities in different Sc_2BiX and Sc_2BrX phases shows attractive bonding traits. The C–Sc, N–Sc, and B–Sc bond metallicitiesfm in the Sc_2BiC, Sc_2BiN, and Sc_2BiB phases are calculated to be 0.0019, 0.168, and 0.0031, respectively. The metallicity fm values for the C–Sc, N–Sc, and B–Sc bonds in the Sc_2BrC, Sc_2BrN, and

Sc_2BrB phases, on the other hand, are 0.013, 0.0038, and 0.364, respectively. The Sc_2BiX phases exhibit a notably high covalent character in their bonding, according to these studies. By integrating both covalent and metallic properties, the Sc_2BrX phases, in contrast, display a more complex bonding behavior. Intriguingly, theSc_2BrB phase stands out with the highest metallicity of all the phases studied, indicating a considerable metallic input to its bonding.

4.3.4. Theoretical Vickers Hardness

A solid's mechanical properties, combining both internal and external variables, affect how hard it is. The hardness of a material is greatly influenced by its natural properties, including adhesive energy, crystal arrangement, and strength of bonds. These qualities are intrinsic to the solid and deeply embedded in its atomic and molecular arrangement. Testing methods, temperature, and other factors can all affect experimental indicators of hardness.

It is a challenging task to theoretically calculate the hardness of MAX phases, which is a partially metallic compound. To calculate the Vickers hardness theoretically for partially metallic systems, Gou *et al*. [124] amplify a model from Gao's equation, based on the Mullikan bond population suing the following equation:

$$H_v^{\mu} = 740\left(P^{\mu} - P^{\mu'}\right)\left(v_b^{\mu}\right)^{-\frac{5}{3}} \qquad \ldots\ldots\ldots\ldots\ldots\ldots\ldots (4.17)$$

Here, P^{μ}representthe positive Mulliken BOP, while the metallic population $P^{\mu'}$ is generated from the unit cell volume (V) and the number of free electrons$n_{free} = \int_{Ep}^{Ef} N(E)dE$with $P^{\mu} = n_{free}/V$. Using $v_b^{\mu} = (d^{\mu})^3 / \sum_{\mu}\left[(d^{\mu})^3 N_b^{\mu}\right]$, where d^{μ} is the bond length and N_b^{μ} is the number of bonds per unit volume, one may determine the bond volume v_b^{μ}.

Table 4.6: Mulliken bond number (n^{μ}), bond length (d^{μ}), bond overlap population (p^{μ}), metallic Population ($p^{\mu'}$), bond volume ($v_b{}^{\mu}$) of μ – type bond and Vickers hardness H_V of Sc_2AX phases.

Compounds	Bond	n^{μ}	d^{μ} (Å)	p^{μ}	$p^{\mu'}$	$v_b^{\mu}(Å^3)$	H_V(GPa)	Ref.
Sc_2BiC	C– Sc	4	2.2885	1.14	0.0022	36.58	2.089	This
Sc_2BiN	N –Sc	4	2.2379	0.88	0.0148	34.529	1.749	This
Sc_2BiB	B –Sc	4	2.3960	1.18	0.0037	40.823	1.798	This
Sc_2BrC	C –Sc	4	2.2820	1.27	0.0166	10.506	2.767	This
Sc_2BrN	N –Sc	4	2.2197	0.89	0.0034	7.0117	2.165	This
Sc_2BrB	B–Sc	4	2.3874	1.49	0.05431	12.116	2.684	This
Sc_2SnC	C–Sc	4	2.2927	1.17	0.00568	36.60	2.1	[52]
Hf_2BiB	B–Hf	4	2.3889	1.73	0.0175	38.781	2.85	[47]

This model helps to explain the mechanical characteristics and hardness of partially metallic materials. The hardness of crystals with intricate multiband structures can be calculated by averaging the hardness values of all the relevant bonds geometrically. The formula for this computation is [125,126]:

$$H_V = \left[\Pi^{\mu}\left(H_v^{\mu}\right)^{n^{\mu}}\right]^{1/\Sigma n^{\mu}} \quad \ldots\ldots\ldots\ldots\ldots\ldots\ldots (4.18)$$

Table 4. 6 contains the hardness values of Sc_2BiC, Sc_2BiN, Sc_2BiB, Sc_2BrC, Sc_2BrN, and Sc_2BrB, which are 2.089, 1.749, 1.798, 2.767, 2.165, and 2.684 GPa respectively. As evident, Bi-based compounds have lower hardness values than Sc_2SnC [52], while the values are higher for Br-based compounds. The Vickers hardness of Sc_2BrC surpasses that of other investigated compounds. The obtained hardness values, ranging from 1.749 to 2.798 GPa, fall within the typical range for MAX phases, which is between 2 to 8 GPa [115]. This indicates that Sc_2BrC, like other MAX phases, exhibits softness and ease of machinability. Comparable MAX compounds, such as Sc_2InC [54] (Hv = 2.4 GPa), Sc_2GaB [106] (Hv = 2.005 GPa), and Sc_2SnC [52] (Hv = 2.1 GPa), display similar characteristics. Among the examined borides, nitrides, and carbides, Sc_2BrC stands out for its ideal combination of mechanical properties.

4.4. The elastic anisotropy

A quantitative evaluation of directional–dependent characteristics under the effect of external stress is required to understand the idea of elastic anisotropy parameter. This phenomenon is crucial to numerous crystalline solids–specific physical processes. These processes include fluid exchange in poor–elastic materials, internal abrasion, phase transitions, and plastic deformations. They also include crack initiation, crack propagation, micro–scale fracturing in ceramics, nontraditional phonon modes, precipitancy, enhanced charged defect mobility, and dislodgment dynamics [127,128]. Atomic configurations along the *a*– and *c*–axes can vary because of the MAX phase materials layered hexagonal symmetry.

Investigations into the anisotropic properties of Sc_2AX compounds use a variety of formalisms. A_1, A_2, and A_3 indicate the elastic shear constants at the [100], [010], and [001] directions of hexagonal crystals, respectively, and are computed using the following equation [129].

Table 4.7: Anisotropy factors of Sc_2AX (A = Bi, Br; X = C, N, B).

Phases	**A_1**	**A_2**	**A_3**	**B_a**	**B_c**	**K_c/K_a**	**A_B**	**A_G**	**A^U**	**Ref.**
Sc_2BiC	1.39	0.79	1.11	278.54	336.01	1.40	0.694	1.036	0.1187	This
Sc_2BiN	1.25	1.01	1.26	292.48	388.28	1.44	0.701	0.527	0.0671	This
Sc_2BiB	1.12	0.92	1.03	192.15	264.89	1.47	0.751	0.255	0.0407	This
Sc_2BrC	1.81	0.78	0.92	272.29	295.43	1.48	0.999	0.826	0.1035	This
Sc_2BrN	1.21	0.76	0.91	292.58	336.03	1.39	0.721	0.934	0.1089	This
Sc_2BrB	1.26	1.45	1.82	199.31	199.81	1.49	1.118	2.873	0.3185	This
Sc_2SnC	1.22	0.95	1.16	-	-	1.12	0.077	0.28	0.029	[52]
Hf_2BiB	0.84	1.17	0.99	293	620	0.94	0.017	0.322	0.033	[47]

The values of these variables, as displayed in Table 4.7, indicate that the compounds under consideration are anisotropic.

$$A_1 = \frac{\frac{1}{6}(C_{11} + C_{12} + 2C_{33} - 4C_{13})}{C_{44}};\ A_2 = \frac{2C_{44}}{C_{11} - C_{12}}$$

$$and A_3 = A_1.A_2 = \frac{\frac{1}{3}(C_{11} + C_{12} + 2C_{33} - 4C_{13})}{C_{11} - C_{12}} \quad \ldots\ldots\ldots\ldots (4.19)$$

In order to calculate the Bulk Modulus (B) in the a– and c–directions, the following relationships are used [130]:

$$B_a = a\frac{dP}{da} = \frac{\Lambda}{\alpha};\ B_c = c\frac{dP}{dc} = \frac{B_a}{\alpha} \quad \ldots\ldots\ldots\ldots (4.20)$$

$$Where, \alpha = \frac{(C_{11} + C_{12}) - 2C_{13}}{C_{33} + C_{13}}; and\ \Lambda = 2(C_{11} + C_{12}) + 4C_{13}\alpha + C_{33}\alpha^2$$

B_c is noticeably higher than B_a in the compounds under consideration, suggesting that compressing the materials in the a–direction is easier than in the c–direction.
Using the bulk modulus (Voigt, Reuss) and shear modulus (Voigt, Reuss) formulas, the percentage of anisotropy in compressibility (A_B) and shear (A_G) is calculated [131]:

$$A_B = \frac{B_V - B_R}{B_V + B_R} \times 100\%;\ A_G = \frac{G_V - G_R}{G_V + G_R} \times 100\% \quad \ldots\ldots (4.21)$$

Additionally, the following is an estimate of the universal anisotropic index A^U [132]:

$$A^U = 5\frac{G_V}{G_R} + \frac{B_V}{B_R} - 6 \geq 0 \quad \ldots\ldots\ldots\ldots (4.22)$$

The non–zero values of A_B, A_G, and A^U (Table 4.7) affirm the anisotropic nature of these solids [133].

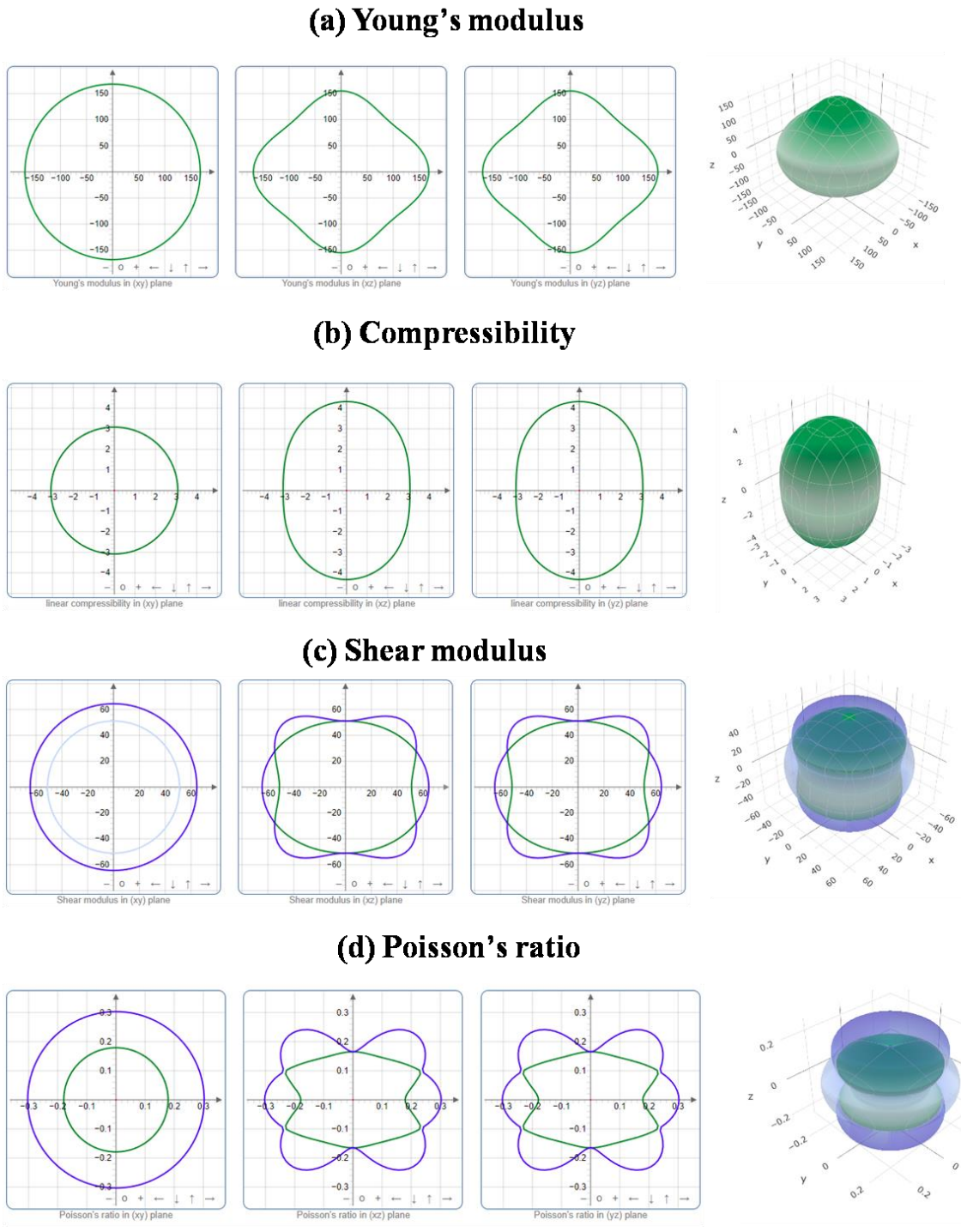

Fig. 4.8(i): 2D and 3D presentations of (a) Young's modulus, Y (b) Linear compressibility, K (c) Shear modulus, G (d) Poisson's ratio, *v* of the Sc_2BiC.

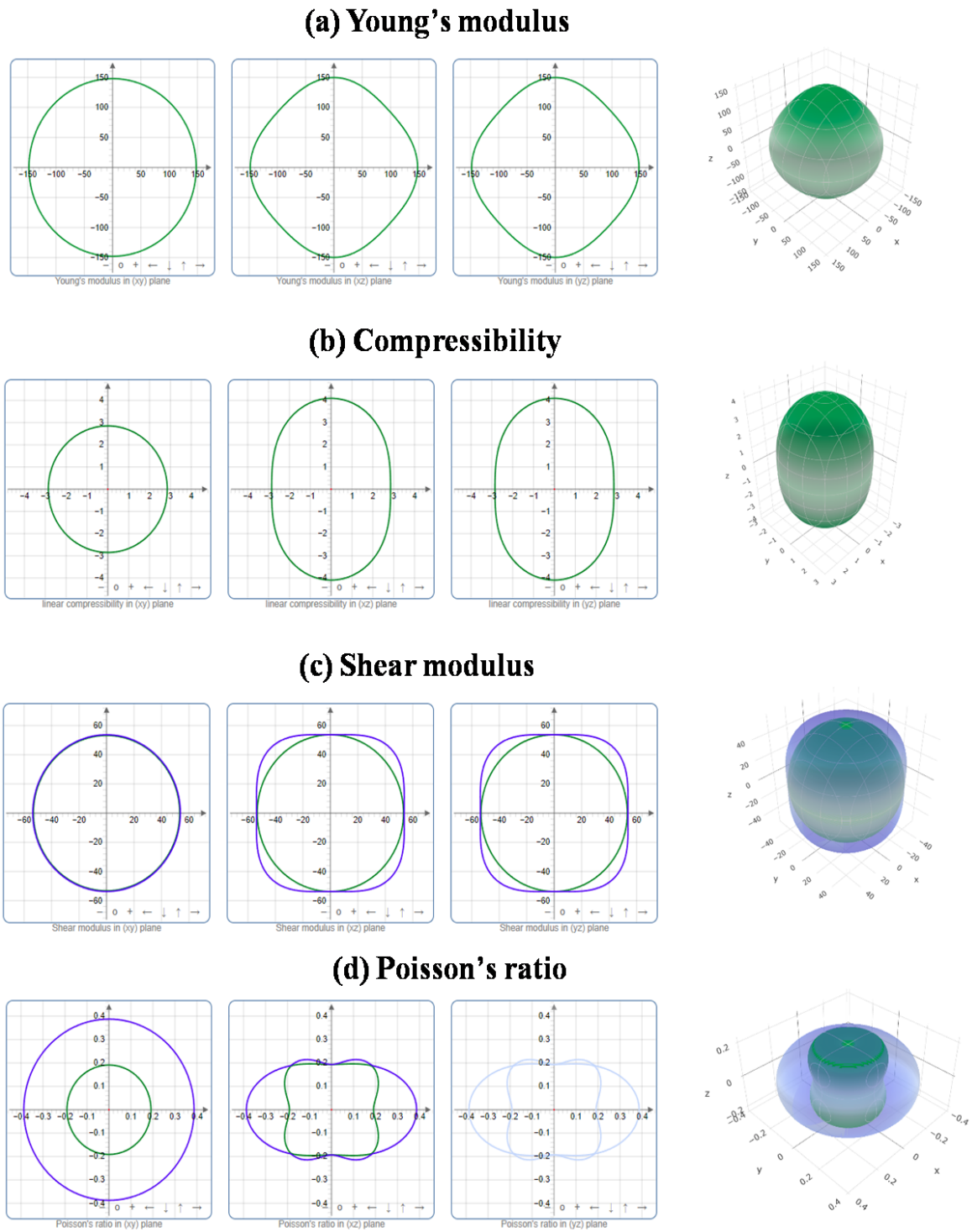

Fig. 4.8(ii): 2D and 3D presentations of (a) Young's modulus, Y (b) Linear compressibility, K (c) Shear modulus, G (d) Poisson's ratio, *v* of the Sc_2BiN.

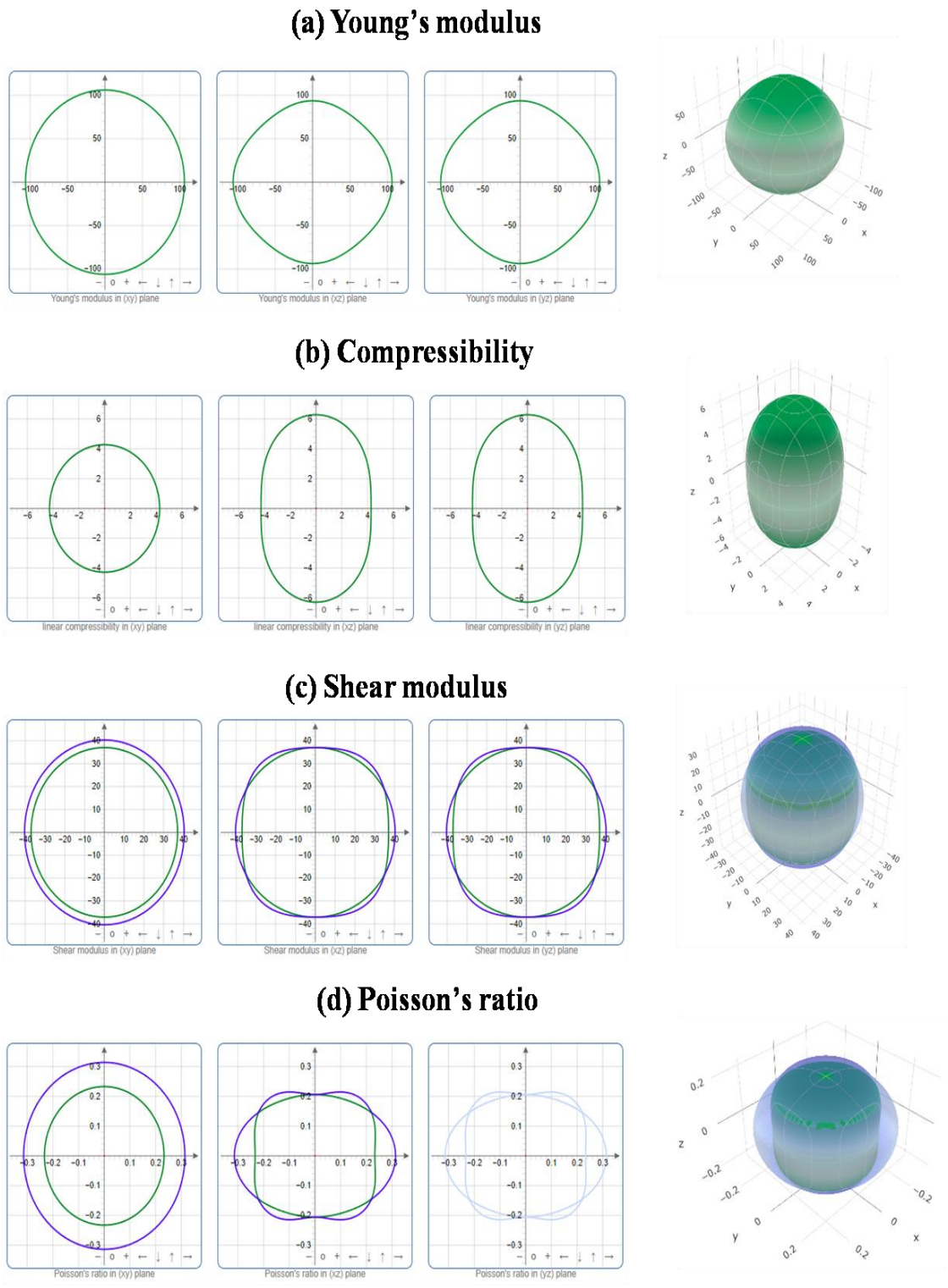

Fig. 4.8(iii): 2D and 3D presentations of (a) Young's modulus, Y (b) Linear compressibility, K (c) Shear modulus, G (d) Poisson's ratio, *v* of the Sc_2BiB.

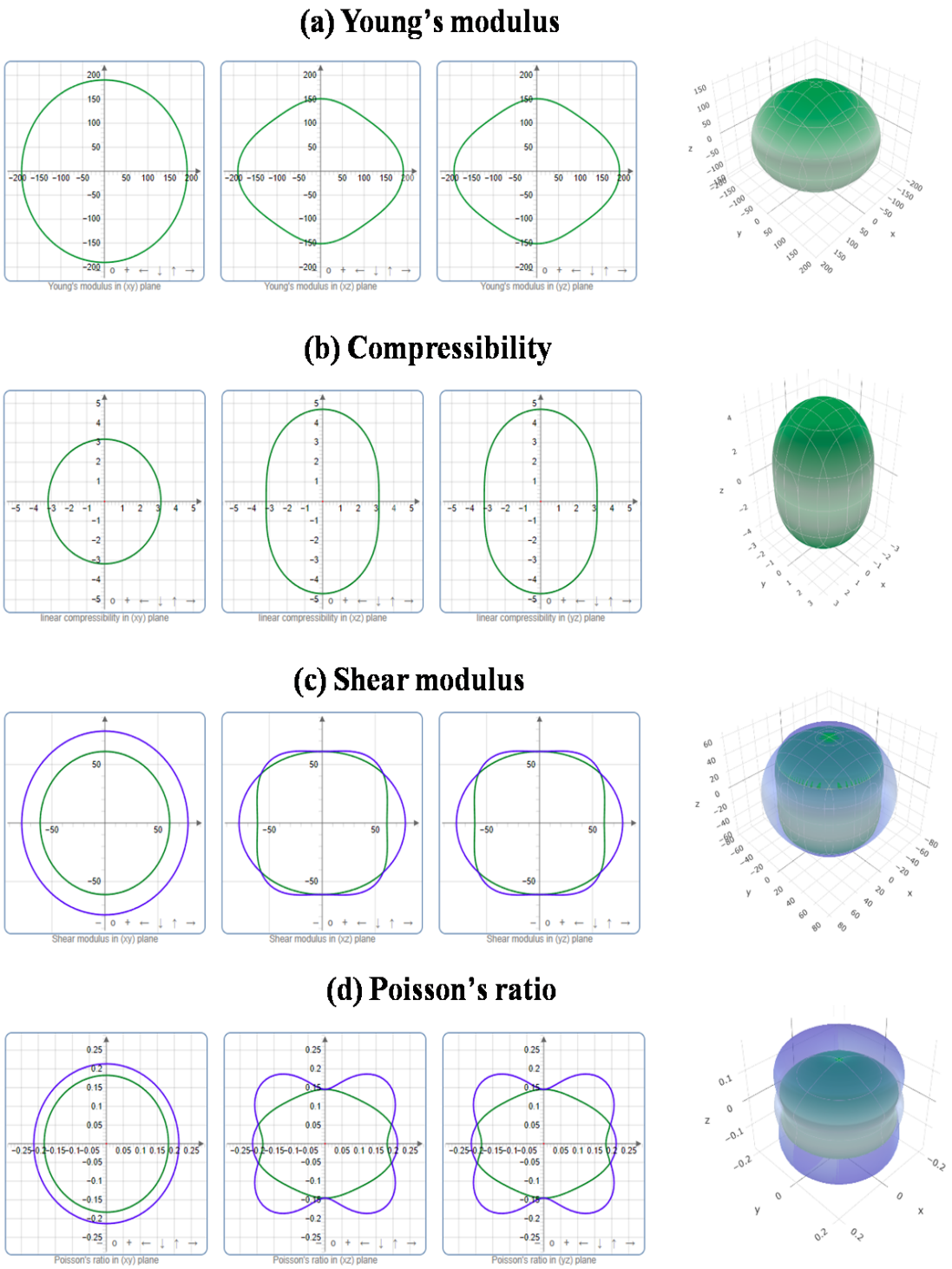

Fig. 4.8(iv): 2D and 3D presentations of (a) Young's modulus, Y (b) Linear compressibility, K (c) Shear modulus, G (d) Poisson's ratio, *v* of the Sc_2BrC.

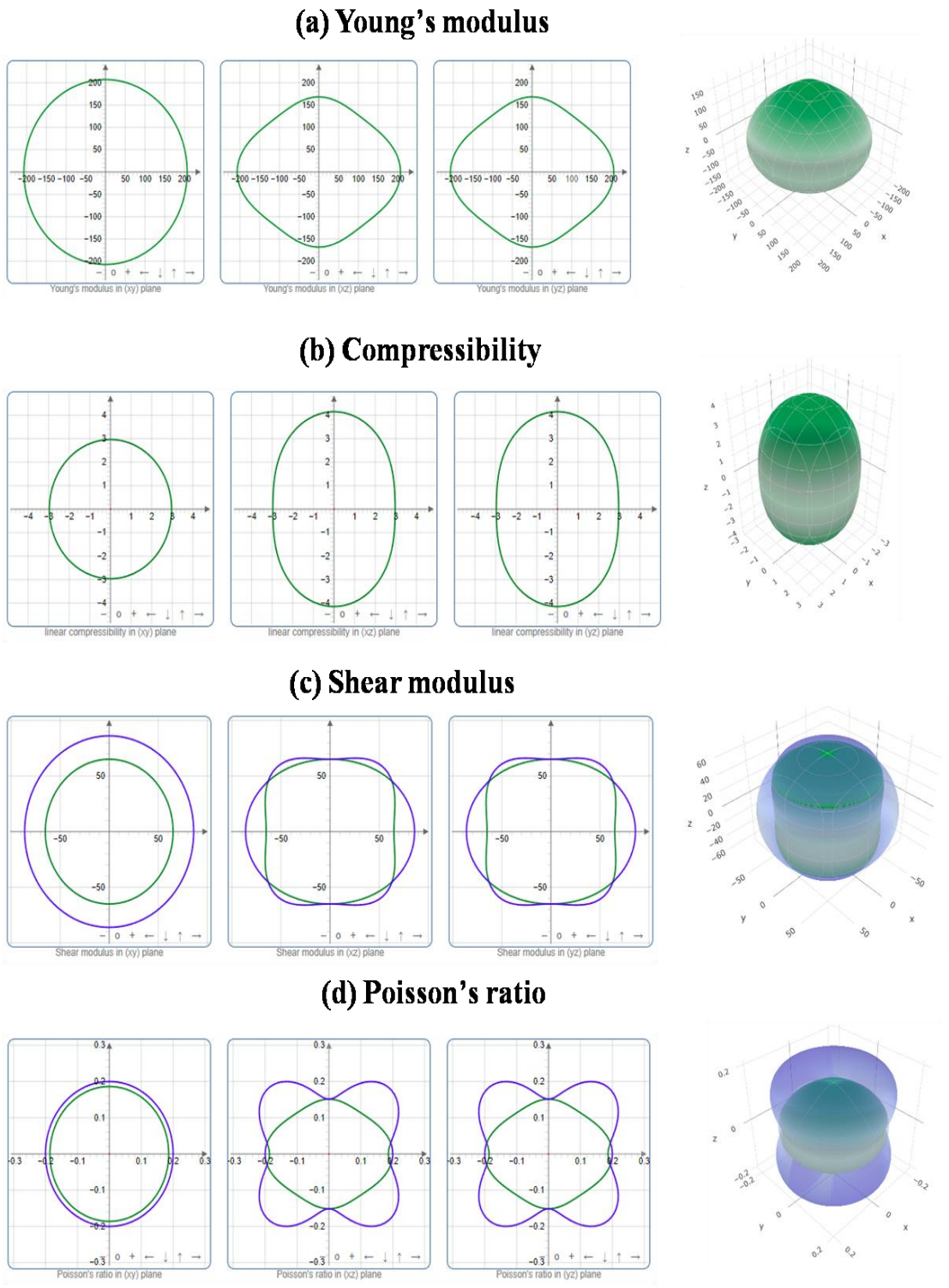

Fig. 4.8(v): 2D and 3D presentations of (a) Young's modulus, Y (b) Linear compressibility, K (c) Shear modulus, G (d) Poisson's ratio, *v* of the Sc_2BrN.

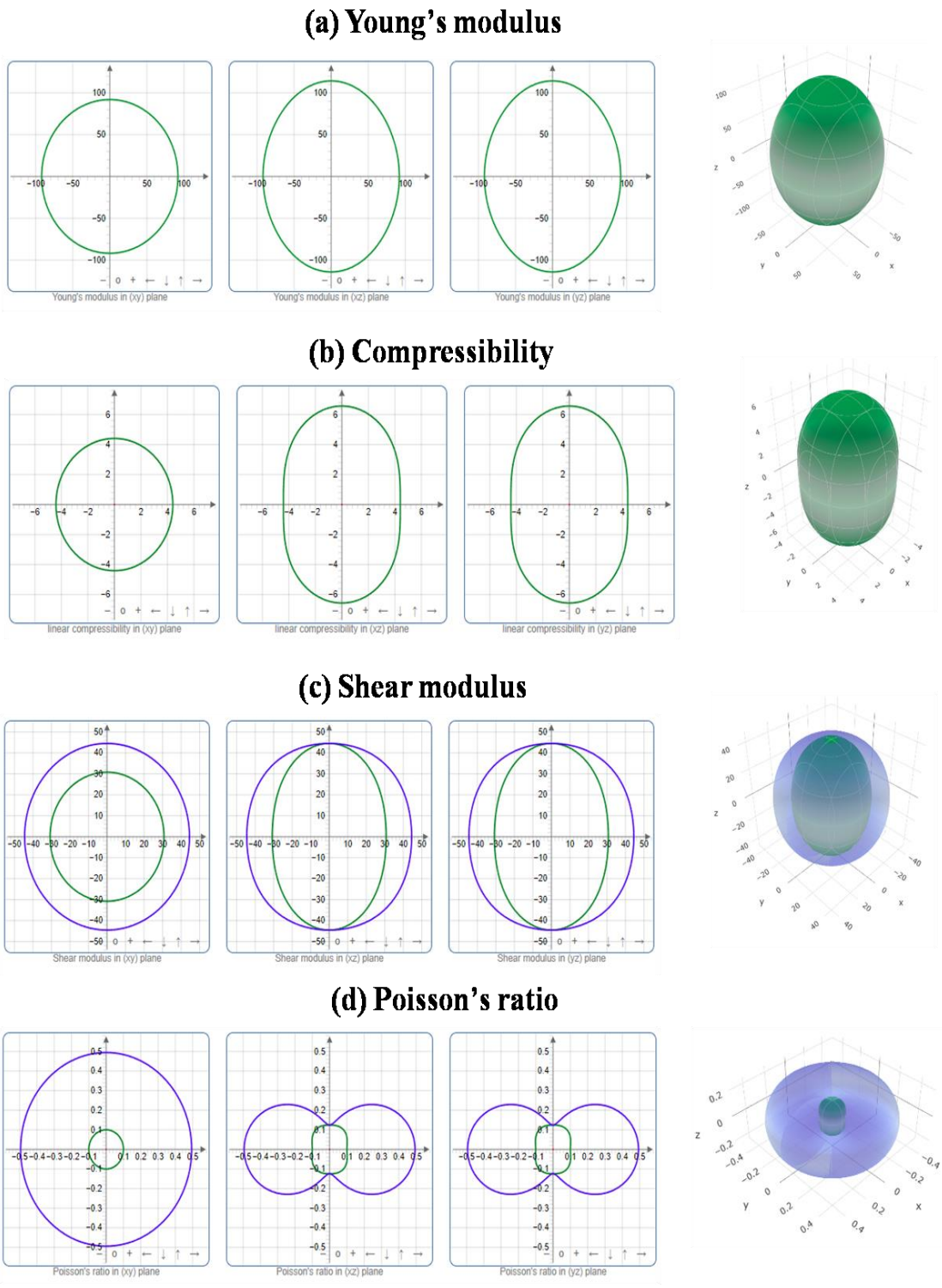

Fig. 4.8(vi): 2D and 3D presentations of (a) Young's modulus, Y (b) Linear compressibility, K (c) Shear modulus, G (d) Poisson's ratio, *v* of the Sc_2BrB.

The use of 3D contour graphs and their 2D projections allows for a visual depiction of mechanical anisotropy. A perfect sphere denotes total isotropy, while variations from the sphere's shape reflect the degree of anisotropy [134]. The stiffness matrix–based 2D and 3D plots produced by the ELATE [135] program are shown in Figs. 4.8 (i-vi).
The Young's modulus (*Y*) and compressibility appeared to be anisotropic in the '*xz*' and '*yz*' planes, while it is isotropic in the '*xy*' plane, as shown in Figs. 4.8(i-vi).

Table 4.8: Calculated minimum and maximum values of the *Y*, 1/*B*, *G*, ν, and the ratio (A) of them for Sc_2AX (A = Bi, Br; X = C, N, B) phases.

Phase	Y_{min} GPa	Y_{max} GPa	A_Y	K_{min} TPa^{-1}	K_{min} TPa^{-1}	A_K	G_{min} GPa	G_{max} GPa	A_G	v_{min}	v_{max}	A_v
Sc_2BiC	133.8	168.1	1.26	3.08	4.32	1.40	51.08	68.80	1.35	0.17	0.31	1.89
Sc_2BiN	135.7	149.6	1.10	2.85	4.09	1.44	53.27	62.36	1.17	0.19	0.39	2.00
Sc_2BiB	92.3	106.1	1.15	4.28	6.29	1.47	37.06	40.83	1.10	0.21	0.31	1.52
Sc_2BrC	147.9	190.3	1.29	3.17	4.69	1.48	61.07	78.41	1.28	0.15	0.25	1.69
Sc_2BrN	161.3	206.8	1.28	2.97	4.15	1.39	65.12	86.17	1.32	0.15	0.26	1.78
Sc_2BrB	92	114.4	1.24	4.41	6.57	1.49	30.79	45.91	1.49	0.10	0.49	4.94

As seen in Figs. 4.8(i-vi) shear modulus is shown across two surfaces in both 2D and 3D renderings. The lowest values are shown by the green line, while the blue line represents the greatest values for each angle. The minimum value denoted by the green line shifts in the direction of the horizontal axis for Sc_2BiC, Sc_2BiB, and Sc_2BrB. The axes of the *xz*– and *yz*–planes are parallel to the maximum values (denoted by the green line), whereas the axes of the minimum values are at a 45–degree angle. The axes of the *xz*– and *yz*–planes correspond to the maximum values of the blue line for the other compounds Sc_2BiN, Sc_2BrC, and Sc_2BrN, whereas the axes of the corresponding minimum values are at a 45° angle. An indication of isotropy within the *xy* plane is conceivable.

[Figs. 4.8(i-vi) show the anisotropic nature of Poisson's ratio (*v*) in the *xz*– and *yz*–planes. The two lines, blue and green, signifying the highest and lowest values for each angle, show the detailed anisotropic pattern.

The minimum and maximum values of *Y, K, G,* and *v* for the Sc_2AX phases are given

in Table 4.8. This table demonstrates that Sc_2BiB exhibits the least anisotropy, whereas Sc_2BrB exhibits the highest level of anisotropy in comparison to the other studied compounds. The table further broadens its coverage to include the minimum and maximum values of *Y, K, G*, and v for different other 211 MAX phases, revealing a comparable level of anisotropy.

4.5. Thermodynamic properties

4.5.1. Thermodynamic potential functions

The thermal characteristics for Sc_2AX (A = Bi, Br; X= C,N, B) at zero pressure using the quasi–harmonic approach [136] were calculated, which allowed us to determine crucial thermodynamic potential functions, including internal energy *E*, Helmholtz free energy *F*, and entropy *S*.

The equilibrium state of a system can be thoroughly analyzed using the thermodynamic potential functions. The following formulas were used to determine the computed parameters *F, E,* and *S* [137]:

$$F = 3nN_A K_B T \int_0^{\omega_{max}} ln\{2\, sinh(\hbar\,\omega/2K_B T)\} g(\omega) d\omega \quad \ldots\ldots\ldots\ldots (4.23)$$

$$E = 3nN_A \frac{\hbar}{2} \int_0^{\omega_{max}} \omega\, coth(\hbar\,\omega/2K_B T) g(\omega) d\omega \quad \ldots\ldots\ldots\ldots\ldots (4.24)$$

$$S = 3nN_A k_B \int_0^{\omega_{max}} \left[\frac{\hbar\omega}{2k_B T} coth(\hbar\,\omega/2k_B T) - ln\{2\, sinh(\hbar\,\omega/2k_B T)\}\right] g(\omega) d\omega \ldots\ldots\ldots\ldots\ldots\ldots\ldots\ldots\ldots\ldots (4.25)$$

In these equations,$k_B$stands for the Boltzmann constant, N_A represents Avogadro's number,$n$for the number of atoms per unit cell, ω_{max} for the cut–off phonon frequency, for the phononfrequency, and $g(\omega)$for the normalized phonon density of states, satisfying, $\int_0^{\omega_{max}} g(\omega) d\omega = 1$.

It is important to note that in the 0–1000 K temperature range, the thermodynamic properties were calculated without taking any phase shifts into account, as shown in Figs. 4.9 (a-c). Free energy, enthalpy, and entropy values for all phases at temperatures

below 100 K are essentially nonexistent. Beyond this point, the free energy, which is a common characteristic in solids going through natural processes, exhibits a nonlinear decline and starts to get progressively worse as the temperature rises. As expected for solids, the enthalpy (*E*) increases as the temperature rises.

Entropy is a crucial factor in measuring the number of possible configurations at the microscopic level and contributes significantly to assessing a system's disorder. The system's entropy also increases noticeably with temperature and is influenced by lattice vibration. The rise in temperature-induced thermal disturbance, which results in more disorder, is thought to be the cause of the increase in entropy.

Additionally, the following thermal properties, such as linear thermal expansion coefficient (TEC), heat capacity at constant pressure (C_p), and heat capacity at constant volume (C_v), were assessed using the equations [138,139]:

$$C_v = 9nN_A k_B \left(\frac{T}{\theta_D}\right) \int_0^{x_D} \frac{x^4}{(e^x - 1)^2};\ TEC = \frac{\gamma C_v}{3B_T V_m};\ C_p = C_v[1 + (TEC)\gamma T] \quad \ldots\ldots\ldots\ldots\ldots\ldots \quad (4.26)$$

Here, n stands for the number of atoms per formula unit, N_A represents the Avogadro number, k_B denotes the Boltzmann constant, B_T represents the isothermal bulk modulus, V_m for the molar volume, and γ stands for the Grüneisen parameter, in that order. $x_D = \theta_D/T$ is also used as a constant.

The fluctuations in C_v, TEC, and C_p for Sc_2AX compounds over the temperature range of 0 – 2000 K are shown in Figs. 4.9 (d-f). As the number of degrees of freedom for particles increases, so does a material's heat capacity, which gauges its ability to absorb thermal energy. At low temperatures below 300 K, the heat capacity follows the Debye–T^3 power–law, while at high temperatures above 600 K, it approaches the Dulong–Petit (DP) model. The difference between C_p and C_v results from the thermal expansion of materials, which is impacted by anharmonicity in the lattice dynamics. This thermal expansion denotes how much a unit cell enlarges with each degree Kelvin increases in temperature [140]. Additionally, in Fig. 4.9(f), the temperature–dependent linear thermal expansion coefficient (TEC) is shown.

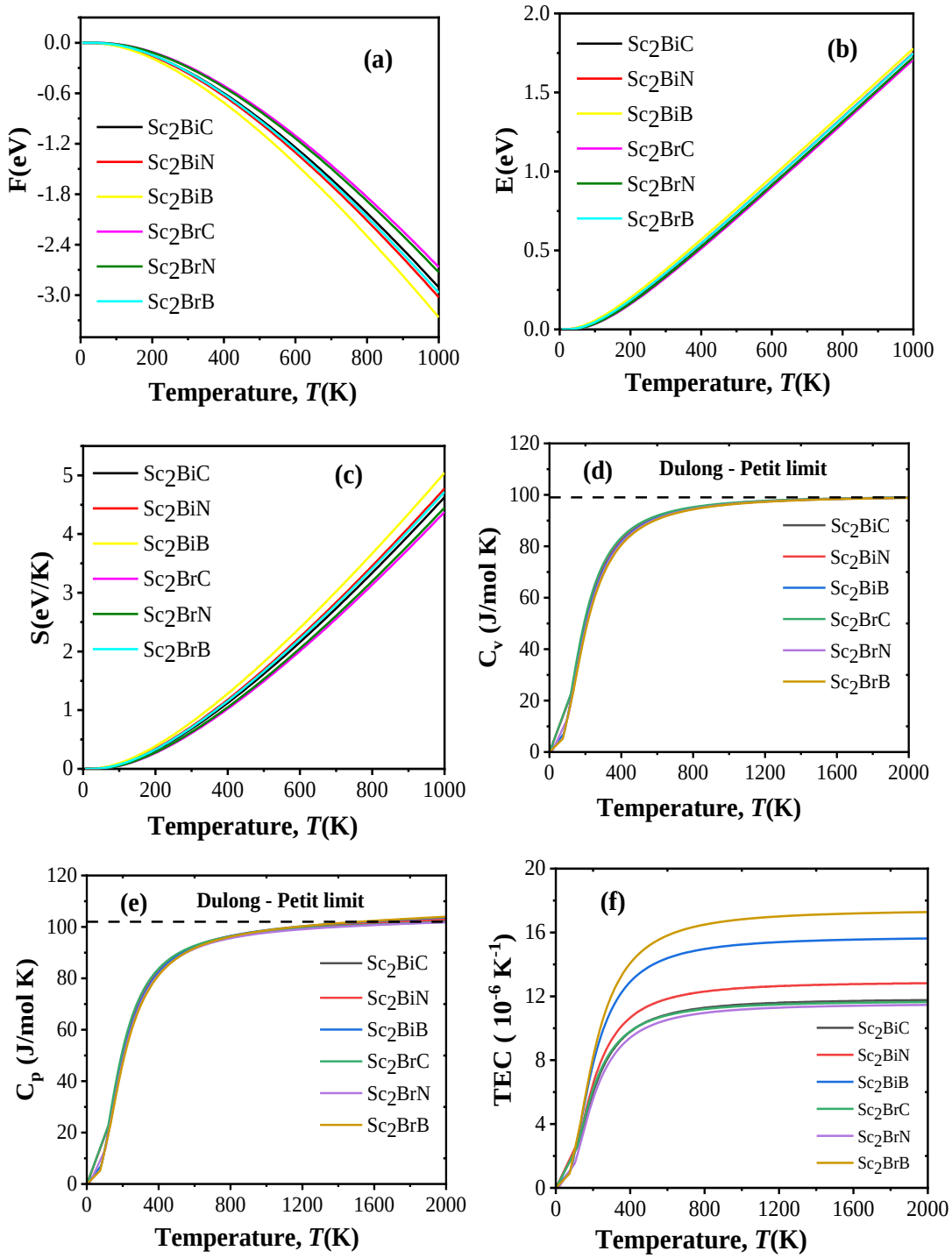

Fig. 4.9: Temperature dependence of the calculated thermodynamic parameters. (a) Free energy, F (b) Internal energy, *E* (c) Entropy, *S* (d) Specific heat at constant volume, *C*v (e) Specific heat at constant pressure, *C*p and (f) Thermal expansion coefficient, (TEC) of Sc_2AX.

The findings show that *TEC* increases rapidly up to 220 K, then steadily between 250K and 400K before reaching a value that is almost constant at high temperatures. Sc_2BiC, Sc_2BiN, Sc_2BiB, Sc_2BrC, Sc_2BrN, and Sc_2BrB have *TEC* values of 8.51×10^{-6}, 9.25×10^{-6}, 10.88×10^{-6}, 8.64×10^{-6}, 8.03×10^{-6}, and $12.11\times10^{-6}K^{-1}$ at 300 K, respectively.

These values are comparable to those of several other MAX phases, such as M_2SX (M =Zr, Nb, Hf; X =B, C) compounds [115], which have *TEC* values 6.71×10^{-6}, 5.90×10^{-6}, 6.22×10^{-6}, and $7.05\times10^{-6}K^{-1}$ at room temperature (300 K), respectively. A very low value of *TEC* is a prerequisite for application in high-temperature technology.
The strong mechanical properties of the MAX phases at high temperatures have made them promise as possible candidates for high–temperature technology. Therefore, sharing knowledge regarding their high–temperature applications is crucial. Thermal barrier coating (TBC) elements are a crucial prerequisite for numerous high–temperature technological applications. The turbine blades of gas turbine engines are commonly treated with TBC to increase their efficiency at high temperatures. The thermal properties, such as Debye temperature (θ_D), phonon thermal conductivity (k_{ph}), minimum thermal conductivity (K_{min}), Grüneisen parameter (γ), and melting temperature (T_m) [87,141] can be used to select the materials for use at high temperatures.

4.5.2. Debye temperature

The Debye temperature (θ_D) regarded as a crucial thermal parameter since it connects the mechanical properties of solids to other important physical processes. The greatest vibrational frequency, also referred to as the Debye frequency, corresponds to the Debye temperature, which in a crystal activates all conceivable lattice vibrational modes.

The calculation of θ_D is made easier by using Anderson's method [142], which is frequently used to compute the sound velocities in solids.
The calculation is dependent on the following equation:

$$\theta_D = \frac{h}{K_B}\left[\left(\frac{3n}{4\pi}\right)\frac{N_A\rho}{M}\right]^{\frac{1}{3}} V_m \qquad \ldots\ldots\ldots\ldots \qquad \ldots\ldots \qquad (4.27)$$

Table 4.9: Calculated Density (ρ), sound velocities (v_l, v_t and v_m), Debye temperature (Θ_D), Gruneisen parameter (γ), minimum thermal conductivity (K_{min}), Lattice thermal conductivity (K_{ph}) and Melting temperature (T_m) of Sc_2AX (A = Bi, Br; X = C, N, B).

Phase	ρ $(gm/cm$	v_l (m/s)	v_t (m/s)	v_m (m/s)	θ_D (K)	k_{min} (W/mK)	k_{ph} (W/mK)	γ	T_m (K)	Ref.
Sc_2BiC	7.058	4992	2912	3230	800	0.64	29.19	1.51	1197	This
Sc_2BiN	7.526	4854	2726	3033	816	0.63	25.53	1.59	1181	This
Sc_2BiB	6.301	4367	2494	2771	772	0.51	28.91	1.54	908	This
Sc_2BrC	4.621	6315	3881	4283	831	0.92	23.93	1.27	1222	This
Sc_2BrN	4.953	6363	3905	4310	847	0.96	23.42	1.28	1301	This
Sc_2BrB	4.152	5360	3111	3452	804	0.69	17.00	1.50	914	This
Sc_2SnC	5.005	6017	3593	3976	449	0.79	19.16		1196	[52]
Hf_2BiB	12.33	4175	2416	2681	297	0.78		1.33		[47]

The terms h, K_B, and N_A in this equation stand for the Planck constant, Boltzmann constant, and Avogadro number, respectively. *M* stands for the molecular weight, *n* for the number of atoms in the molecule, and for the mass density. The following formula can be used to determine the mean sound velocity, abbreviated as V_m:

$$v_m = \left[\frac{1}{3}\left(\frac{1}{v_l^3} + \frac{2}{v_t^3}\right)\right]^{-1/3} \quad \ldots\ldots\ldots (4.28)$$

Here, $v_l$denotes the sound velocity in the longitudinal and v_t represent the transverse modes and the values of v_l and v_t are estimated by the formulae below:

$$v_l = \left(\frac{3B + 4G}{3\rho}\right)^{\frac{1}{2}};\ v_t = \left(\frac{G}{\rho}\right)^{\frac{1}{2}} \quad \ldots\ldots\ldots\ldots (4.29)$$

Table 4.9 shows the computed values of v_l, v_t, v_m, and θ_D for the Sc_2AX compounds. A substance's ability to conduct heat is greatly influenced by the sound velocity of that material.

The compounds are in the following order, based on the expected values of θ_D: Sc_2BrN > Sc_2BrC > Sc_2BiN > Sc_2BrB > Sc_2BiC > Sc_2BiB. These compounds' typical sound

velocities also follow the same pattern as θ_D. Notably, a recent study by Hadi *et al.* revealed a potential thermal barrier coating (TBC) material belonging to the MAX phase family (V_2SnC) [143] that has a θ_D value of 472 K. The $Y_4Al_2O_9$ [103] compound is a well–known TBC material with $\theta_D$value 564 K, which is lower than all of the Sc_2AX compounds investigated. This implies that the investigated compounds have promise as prospective TBC material candidates.

4.5.3. Melting temperature

In order to determine the melting temperature (T_m) of hexagonal crystals like the MAX phases, Fine *et al.* [144] developed an empirical method that makes use of single-crystal elastic constants. The following is the calculation ofT_m's formula:

$$T_m = 354 + 1.5(2C_{11} + C_{33}) \quad \ldots\ldots\ldots\ldots (4.30)$$

The computed T_m values for the Sc_2AX phases are shown in Table-4.9 below. Interestingly, Sc_2BrN has the highest melting point, whilst Sc_2BiB has the lowest. Crystals with higher melting points have stronger interatomic forces at work. As a result, a relationship between the elastic moduli and the crystal melting point can be found, which has been demonstrated in Fig. 4.10 (a) for Sc_2AX phases. According to the analysis, the melting point correlates more favorably with the bulk modulus (*B*) and Young's modulus (*Y)* than it does with the shear modulus (*G*).

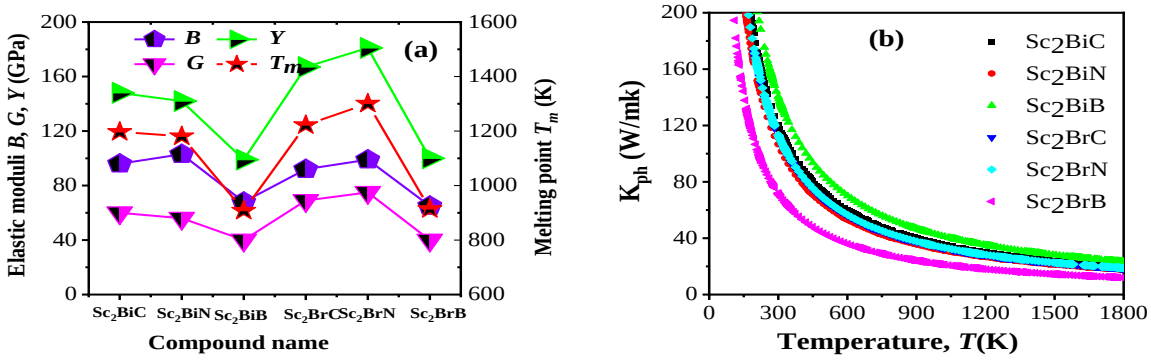

Fig. 4. 10: (a) Melting temperature with elastic moduli, (b) Lattice thermal conductivity as a function of temperature.

4.5.4. Lattice thermal conductivity

The lattice thermal conductivity (K_{ph}) offers important details regarding how heat energy is transferred through lattice vibrations in a material because of temperature gradients. To compute K_{ph}, Slack [145] proposed the following empirical formula:

$$K_{ph} = A(\gamma)\frac{M_{av}\theta_D^3\delta}{\gamma^2 n^{\frac{2}{3}}T} \quad \ldots\ldots\ldots \quad (4.31)$$

$$\gamma = \frac{3(1+v)}{2(2-3v)} \quad \ldots\ldots\ldots\ldots (4.32)$$

The absolute temperature, in this case, is T, θ_D is the Debye temperature, the Grüneisen parameter is represented by γ, and the total number of atoms in the unit cell is indicated by n. Higher values of the Grüneisen parameter (γ) indicate lower phonon thermal conductivity because of significant anharmonic contributions. [131]. M_{av}denotes the compound's average atomic mass per atom. The following expression can be used to calculate the formula's coefficient$A(\gamma)$:

$$A(\gamma) = \frac{4.85628 \times 10^7}{2\left(1 - \frac{0.514}{\gamma} + \frac{0.228}{\gamma^2}\right)} \quad \ldots\ldots\ldots\ldots\ldots \quad (4.33)$$

The computed K_{ph} values for Sc_2AX compounds at 300K are provided in Table-4.9, along with the appropriate Grüneisen parameter, and their temperature dependence is depicted in Fig. 4.10 (b). As temperature rises, there is a steady decrease in lattice thermal conductivity. Among the investigated phases, Sc_2BiC displays the greatest K_{ph} value, while Sc_2BrB displays the lowest. TheK_{ph} values for the 211 MAX phases were reported to range from 2.5 (W/mK) to 36 (W/mK) [2]. Furthermore, a MAX phase (Ti_2SnC) [52] with a K_{ph} value of 30 (W/mK) has been reported by Hadi *et al.* , which is higher than the compounds investigated here.

4.5.5. Minimum thermal conductivity

The lower limit of a compound's inherent thermal conductivity at high temperatures is represented by its minimal thermal conductivity (K_{min}). It functions as an essential indication for materials designed for high–temperature applications. A typical method for determining the minimum thermal conductivity of solids is the Clarke model, given by the equation [146]:

$$K_{min} = K_B v_m \left(\frac{M}{n\rho N_A}\right)^{-2/3} \quad \ldots\ldots\ldots\ldots \quad (4.34)$$

The K_{min} values obtained after applying this model are listed in Table 4.8. These numbers are strongly dependent on the mean sound velocity (v_m). It is noteworthy that the lowest $v_m$matches the lowest K_{min}value. Due to its remarkably low v_m, Sc_2BiB compound has the best K_{min} among all compounds. The studied Sc_2AX phases have lower K_{min} values than traditional TBC materials like V_2SnC [143] (1.20 W/mK) and $Y_4Al_2O_9$ [103] (1.13 Wm1 K1), establishing them as extremely interesting options for TBC applications.

Additionally, the thorough analysis of the parameters TEC, K_{min}, θ_D, and T_m for Sc_2AX in comparison to the well–known traditional TBC material $Y_4Al_2O_9$ [103] and the MAX phase TBC material V_2SnC [143] highlights the tremendous potential of Sc_2AX compounds as TBC candidates. Sc_2BiB and Sc_2BrN stand out as the best and most viable options among them, demonstrating their applicability and potential in high–temperature environments.

4.6. Optical Properties

In the field of materials science, investigating optical characteristics in solids has taken on a central role and opened doors to a wide range of potential applications. This work presents the optical properties of Sc_2AX (A = Bi, Br; X = C, N, B) MAX. The optical properties of the Sc_2AX compounds for polarization orientations [100] are calculated and presented in Fig. 4.11 and 4.12 up to 19 eV. By looking at their band structures, the Sc_2AX compounds all exhibit a metallic character, except Sc_2BrB. The dielectric characteristics of the compounds are strongly influenced by both intra–band and inter–band transitions. The low–energy spectrum is refined by adding a plasma frequency of 3 eV. At 0.5 eV Gaussian blurring was used to improve *k*-point efficiency close to the Fermi level. The complex dielectric function is $\varepsilon(\omega) = \varepsilon_1(\omega) + i\varepsilon_2(\omega)$, where the $\varepsilon_2(\omega)$ represents light absorption, $\varepsilon_1(\omega)$ characterizes the polarization of the material. The imaginary portion of the dielectric function can be expressed [147]:

$$\varepsilon_2(\omega) = \frac{2e^2\pi}{\Omega\varepsilon_0}\sum_{k,v,c}\left|\psi_k^c\right|\boldsymbol{u}.\boldsymbol{r}|\psi_k^v|^2\delta(E_k^c - E_k^V - E) \quad \ldots\ldots\ldots(4.35)$$

Here, e denotes the charge of the electron, ψ_k^c denotes the wave function of the conduction band, ψ_k^v denotes the wave function of the valence band, and $\boldsymbol{u}$ is the unit vector defining the polarization of the applied electric field. The real part $[\varepsilon_1(\omega)]$ of $\varepsilon(\omega)$ can be calculated from the imaginary part by applying the Kramers–Kronig transformation equation [148,149].

$$\varepsilon_1(\omega) = 1 + \frac{2}{\pi}P\int_0^\infty \frac{\acute{\omega}\varepsilon_2(\acute{\omega})d\acute{\omega}}{\left(\acute{\omega}^2 - \omega^2\right)} \quad \ldots\ldots\ldots(4.36)$$

In this case, P denotes the integral's primary value. Calculations for loss function$L(\omega)$, reflectivity $R(\omega)$, extinction coefficient $K(\omega)$, refractive index $\eta(\omega)$, absorption coefficient$\alpha(\omega)$, and photoconductivity $\sigma(\omega)$, are used the following equation [150–152]:

$$R(\omega) = \left|\frac{\sqrt{\varepsilon(\omega)} - 1}{\sqrt{\varepsilon(\omega)} + 1}\right|^2 \quad \ldots\ldots\ldots(4.37)$$

$$L(\omega) = \frac{\varepsilon_2(\omega)}{[\{\varepsilon_1(\omega)\}^2 + \{\varepsilon_2(\omega)\}^2]} \quad \ldots\ldots\ldots\ldots(4.38)$$

$$K(\omega) = \frac{1}{\sqrt{2}}\left[\sqrt{\{\varepsilon_1(\omega)\}^2 + \{\varepsilon_2(\omega)\}^2} - \varepsilon_1(\omega)\right]^{1/2} \quad \ldots\ldots\ldots(4.39)$$

$$\eta(\omega) = \frac{1}{\sqrt{2}}\left[\sqrt{\{\varepsilon_1(\omega)\}^2 + \{\varepsilon_2(\omega)\}^2} + \varepsilon_1(\omega)\right]^{1/2} \quad \ldots\ldots\ldots(4.40)$$

$$\alpha(\omega) = \sqrt{2}\omega\left[\sqrt{\{\varepsilon_1(\omega)\}^2 + \{\varepsilon_2(\omega)\}^2} - \varepsilon_1(\omega)\right]^{1/2} \quad \ldots\ldots\ldots(4.41)$$

$$\sigma(\omega) = \frac{\omega\varepsilon_2}{4\pi} \quad \ldots\ldots\ldots(4.42)$$

The complex dielectric behavior of the MAX phases for incident photon energy is vividly depicted in Figs. 4.11 (a, b). At lower frequencies, intra-band transitions predominate, whereas the band structure and inter-band term are closely entwined, as noted [153]. As the real part of the dielectric constant $\varepsilon_1(\omega)$approaches zero from below, it becomes clear that Drude–like behavior is emerging. The value of $\varepsilon_1(\omega)$transition from below to zero at distinct energies16.34, 13.93, 17.61, 18.32,

18.20, and 17.44 eV for Sc_2BiC, Sc_2BiN, Sc_2BiB, Sc_2BrC, Sc_2BrN, and Sc_2BrB compounds, respectively. At the same time, the significant positive values of $\varepsilon_2(\omega)$at lower energies indicate strong absorption tendencies for [100] polarizations within Sc_2AX phases. Interestingly, for both polarization directions, the values of $\varepsilon_2(\omega)$ switch from above to zero at around 16.34, 13.93, 17.61, 18.32, 18.20, and 17.44 eV photon energy for Sc_2BiC, Sc_2BiN, Sc_2BiB, Sc_2BrC, Sc_2BrN, and Sc_2BrB compounds, respectively. This behavior indicates the metallic character of the Sc_2AX (A = Bi, Br; X = C, N, B) MAX phases.

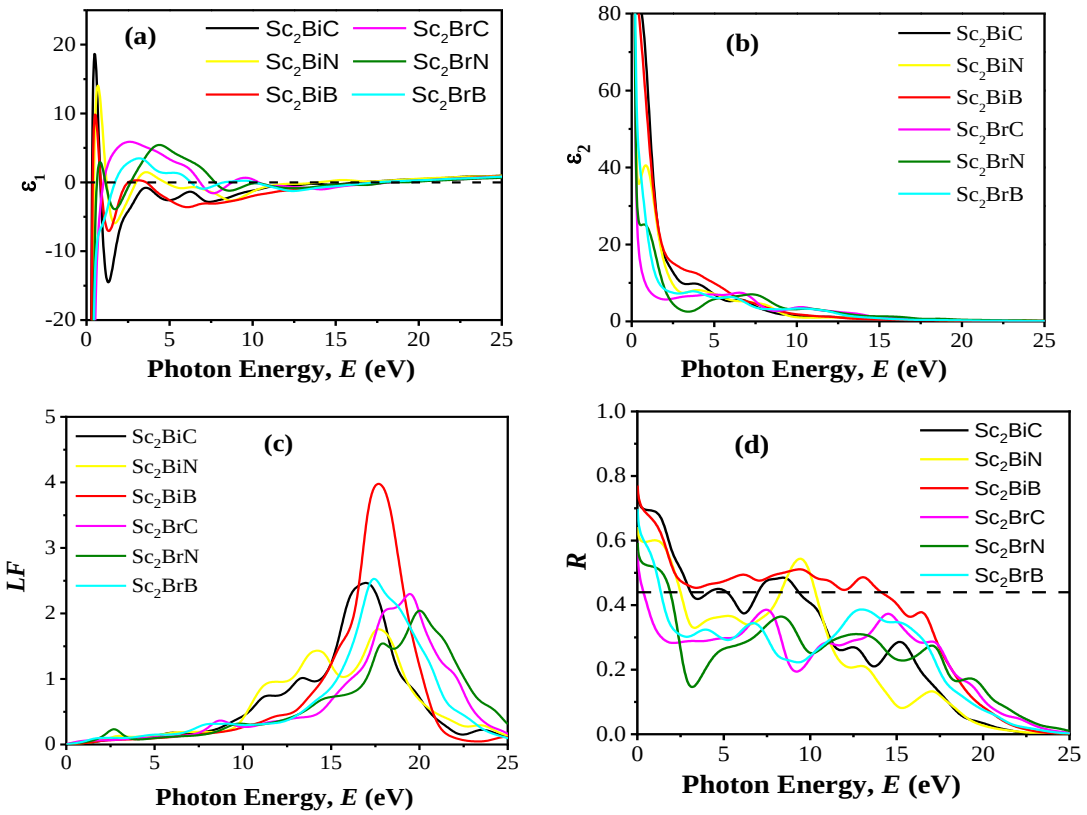

Fig. 4.11: (a) Real part of dielectric constant, (ε_1); (b) Imaginary part of dielectric constant, (ε_2); (c) Loss function, (LF); and (d) Reflectivity, (R) of Sc_2AX for [100] polarization directions.

The loss function, a crucial optical metric, represents the amount of energy that a high–speed electron gives up when moving through matter. The loss function for Sc_2AX is shown in Fig. 4.11(c). The bulk plasma frequency (ω_p), where $\varepsilon_2(\omega) < 0$ and $\varepsilon_1(\omega) = 0$, coincides with its peak.

It is significant that the loss function spectrum is used to obtain the bulk plasma frequency (ω_p). When the frequency of the incident light exceeds the plasma frequency in the context of the researched Sc_2AX (A = Bi, Br; X = C, N, B) MAX phases, transparency is expected. For Sc_2BiC, Sc_2BiN, Sc_2BiB, Sc_2BrC, Sc_2BrN, and Sc_2BrB, the ω_p was found at 16.98, 17.68, 17.69, 19.48, 20.05, and 17.49 (19.5) eV, respectively. It is noteworthy that the loss function's peak energy matches the trailing edges of the reflection spectrum.

The term reflectivity can quantify this effect, which denotes the proportion of the reflected wave to the incident wave. The reflectance spectra for compounds Sc_2AX with a particular crystal orientation [100] are shown in Figs. 4.11(d) as a function of photon energy. The starting point of these spectra corresponds to zero frequency. More specifically, the reflectance values at zero frequency $R(0)$ for the compounds Sc_2BiC, Sc_2BiN, Sc_2BiB, Sc_2BrC, Sc_2BrN, and Sc_2BrB are 0.76, 0.64, 0.77, 0.57, 0.59, and 0.67, respectively. According to Li *et al.* [154], a reference line is drawn at 44% of reflectance (R) to assess their potential as coating materials for solar heating reduction. This benchmark shows that MAX phases can reflect solar light and, as a result, reduce solar heating in the visible region, with a consistent reflectivity in that region averaging around 44%. All compounds, except Sc_2BrC and Sc_2BrB compounds, display reflectivity above 44% in the infrared range (1.24 eV to 1.7 eV) and the visible range (1.7 eV to 3.3 eV). It should be noted that Sc_2BrB exhibits noticeable reflectivity in the infrared range, making it also a candidate for coating material that can block heat from infrared rays. Intriguingly, the Sc_2BiB compounds stand out when focusing on polarization [100], with reflectivity reaching 44% in the ultraviolet (UV) region, extending up to energies of 14.22 eV. The reflectance spectra of all substances tend to approach zero at photon energies between 22 and 29 eV. All the compounds studied, except Sc_2BrC, have promising qualities that could be used in solar heating reduction applications.

The refractive index $\eta(\omega)$ for Sc_2AX is shown in Figs. 4.12(a), an important optical parameter with major effects on the design of optical devices including photonic crystals and waveguides. It is particularly helpful in adjusting optical functions. For our examined compounds, Sc_2BiC (14.13), Sc_2BiN (9.02), Sc_2BiB (15.08), Sc_2BrC (6.95), Sc_2BrN (7.64), and Sc_2BrB (10.91) using GGA PBEsol had different refractive index

$\eta(0)$ static values when analyzed in the context of electric field polarization along the [100] direction. The growth of the refractive index with incident photon energy is notable because it exhibits a behavior that is like that of $\varepsilon_1(\omega)$, proving their relationship. Elevated refractive index values are caused by a reduction in the wave's propagation speed through Sc_2AX brought on by the presence of electron interactions. The higher values of the refractive index clearly demonstrate this impact.

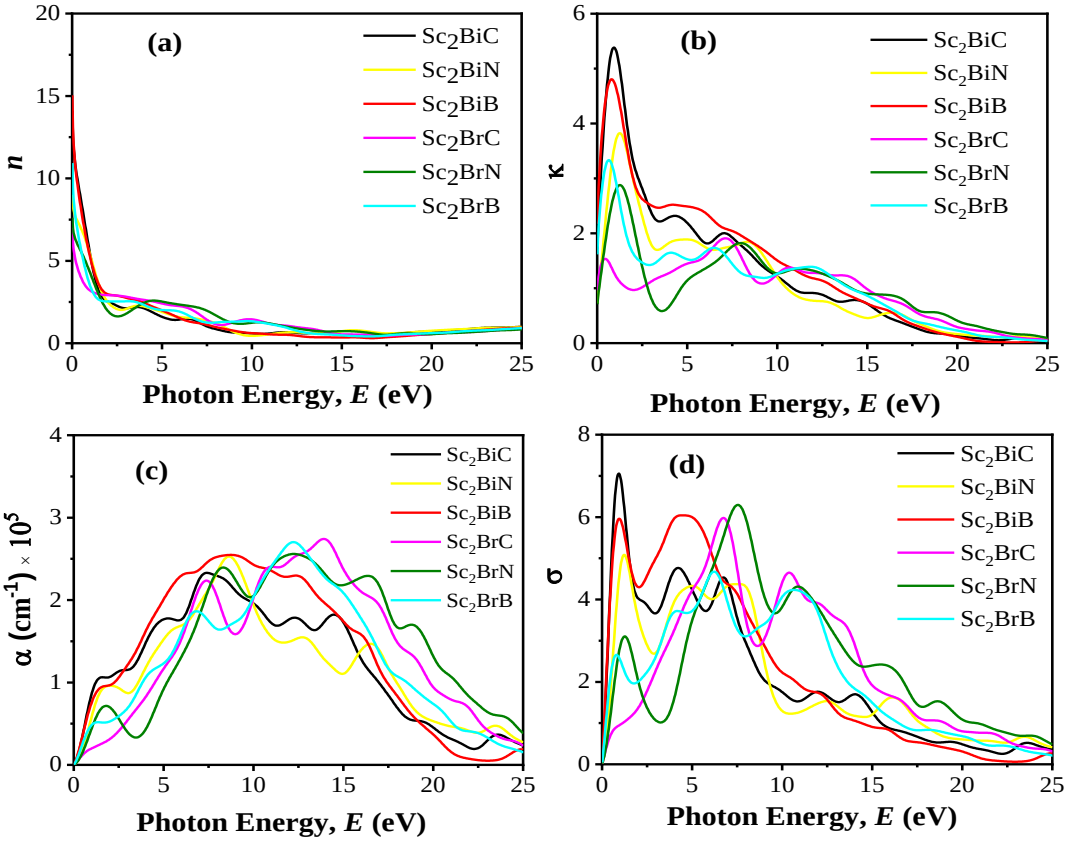

Fig. 4. 12: (a) Refractive index (η), (b) Extinction coefficient (k), (c) Absorption coefficient (α), and (d) Photoconductivity (σ)of Sc_2AX for [100] electric field directions.

Additionally, Figs. 4.12 (b) highlights the extinction coefficient, abbreviated as$k(\omega)$, emphasizing its significance in measuring the absorption loss when electromagnetic radiation passes through an optical medium. It's interesting to note that the association between the $k(\omega)$ and$\varepsilon_2(\omega)$ spectra is strengthenedacross all MAX phases covered in this paper. The Sc_2AX compounds' intrinsic features are indicated by the $k(\omega)$range, which is between 0.7 and 2.21. At 23 eV, $k(\omega)$ diminishes to zero, which is indicative

of Sc_2AX's unique oscillatory nature. Notably, $k(\omega)$ exceeds $\eta(\omega)$ within the energy range of 5 eV to 17 eV, indicating a region where light penetration within the compound is constrained. This phenomenon fits the characteristics of reflective metal detected in Sc_2AX materials.

An important consideration for the materials used in solar cells is the absorption coefficient$\alpha(\omega)$, which provides information on the effectiveness of solar energy conversion. It determines the degree to which light of a particular wavelength is absorbed inside a solid material.

The spectra of the Sc_2AX (A = Bi, Br; X = C, N, B) MAX phases energy–based absorption is shown in Fig. 4.12(c). It is noteworthy that the Sc_2AX absorption coefficient $\alpha(\omega)$ starts at 0 eV when considering polarization orientations with a factor of [100] due to their metallic properties. All phases display strong absorption coefficients inside the UV area, as can be seen by looking at the absorption profiles. As one moves into the UV region, the IR range shows a progressive increase in absorption coefficients, peaking in the energy range of 7.5–14. 0 eV. Furthermore, 2.3 to 2.8 eV is the range of the greatest value. The absorption spectra typically show little anisotropy over the whole range of photon energies. It is interesting that the absorption coefficients in the high–energy region show a noticeable rise. This finding highlights the potential of Sc_2AX compounds as absorbent materials, especially in this energy range.
Particularly in the visible and UV light ranges, these specialized materials are widely used in optical and optoelectronic systems. As a result, their distinct absorption characteristics raise the possibility of them enhancing optical and energy–related technology.

A material's photoconductivity $\sigma(\omega)$ is the phenomenon whereby its electric conductivity rises because of absorbing light. The process of photoconductivity starting from zero photon energy is shown in Figs. 4.12(d). This spectral response characteristic is consistent with the strong metallic nature displayed by these compounds. Notably, the distinctive photoconductivity spectrum trends confirm the compound's metallic properties. The maximum photoconductivity among the Sc_2AX compounds appears in the IR to near visible region, in the following order: Sc_2BiC > Sc_2BiB > Sc_2BiN >

Sc_2BrN > Sc_2BrB > Sc_2BiC. The results of the absorption coefficient$\sigma(\omega)$ are consistent with this order. Therefore, these Sc_2AX materials have the potential to be used in optoelectronic devices that operate in the IR and visible light spectrums. It is noteworthy that the findings from the electronic density of states (DOS) are in good agreement with the concordance between the absorption coefficient and photoconductivity properties. This alignment strengthens the material's compatibility and increases their attraction for use in optoelectronic applications.

CHAPTER 5
CONCLUSIONS

5.1. General

In this thesis, we have conducted a comprehensive investigation into the physical properties of Sc_2AX (A = Bi, Br; X = C, N, B) compounds utilizing DFT-based ab-initio calculations with various exchange–correlation functionals. Our study aimed to elucidate stability, electronic structure, mechanical properties, and potential applications of these compounds, providing a robust foundation for future research and practical implementations.

5.2. Key Findings

- The study confirmed the stability of Sc_2AX (A = Bi, Br; X = C, N, B) compounds through negative formation energy, phonon dispersion curves, and elastic constants (C_{ij}).
- Among the compounds, Sc_2BrB was identified as a semiconductor with a 0.495 eV indirect bandgap using the HSE06 functional, while the other phases displayed metallic characteristics with significant valence and conduction band overlap at the Fermi level.
- The electronic band structures indicated anisotropy in conductivity, and the DOS analysis highlighted the significant contribution of Sc–*d* electronic states to electrical conductivity. Additionally, charge density mapping (CDM) and partial density of states (PDOS) analyses revealed complex bonding patterns and anisotropy in mechanical properties, with Sc_2BrN and Sc_2BiB demonstrating the most and least favorable mechanical properties, respectively.
- The compounds exhibited varying degrees of ductility and brittleness, and their potential for exfoliation into 2D nanosheets was indicated by the f-index. In the optical domain, these compounds showed anisotropic behavior, aligning with their electronic and mechanical properties, and emerged as promising candidates for advanced coating materials to mitigate solar heating.

5.3. Limitation of the Study

While our study provides substantial insights, it is not without limitations. DFT-based calculations, despite being powerful, may not capture all the subtleties of real-world material behavior, particularly under extreme conditions. Furthermore, the exchange–correlation functional employed, though diverse, might still introduce certain approximations that could affect the accuracy of predicted properties. Experimental validation of our theoretical predictions is essential to confirm the reliability of our findings.

5.4. Recommendation for Further Study

Future research should focus on experimental validation of the predicted properties to confirm their practical applicability. Further exploration of the Sc_2AX (A = Bi, Br; X = C, N, B) compounds under different environmental conditions and stressors would provide a more comprehensive understanding of their behavior. Investigating the potential for exfoliating these compounds into 2D nanosheets could open new avenues for material applications in nanotechnology. Additionally, exploring the doping and alloying of these compounds might enhance their properties, making them even more versatile for various technological applications.

5.5. Impact of the Present Research

The findings of this study have several practical implications. The identified compounds, particularly Sc_2BrB, could be utilized in semiconductor applications due to their bandgap properties. The robust mechanical properties of Sc_2AX make them potential candidates for applications requiring high damage tolerance and crack resistance. The anisotropic optical properties of these compounds highlight their potential for advanced coating applications aimed at reducing solar heating. This could provide innovative solutions for thermal barrier coatings (TBC) in a wide range industry.

References

[1] D. J. Green, An introduction to the mechanical properties of ceramics, Cambridge University Press, 1998.

[2] M. W. Barsoum, MAX Phases: Properties of Machinable Ternary Carbides and Nitrides, WILEY-VCH Verlag GmbH & Co. KGaA, 2013.

[3] M. A. Hadi, Superconducting phases in a remarkable class of metallic ceramics, Journal of Physics and Chemistry of Solids 138 (2020) 109275. https://doi. org/10.1016/j. jpcs.2019.109275.

[4] W. Jeitschko, H. Nowotny, F. Benesovsky, Kohlenstoffhaltige ternare Verbindungen, Mh. Chem. 94 (1963) 844–850.

[5] W. Jeitschko, H. Nowotny, F. Benesovsky, Die H-Phasen: Ti_2CdC, Ti_2GaC, Ti_2GaN, Ti_2InN, Zr_2InN und Nb_2GaC, Monatshefte Für Chemie 95 (1964) 178–179. https://doi. org/10.1007/BF00909264.

[6] V. H. Nowotny, Strukturchemie einiger Verbindungen der Übergangsmetalle mit den elementen C, Si, Ge, Sn, Progress in Solid State Chemistry 5 (1971) 27–70.https://doi.org/10.1016/0079-6786(71)90016-1.

[7] W. Jeitschko, H. Nowotny, F. Benesovsky, Die H-Phasen Ti_2TlC, Ti_2PbC, Nb_2InC, Nb_2SnC und Ta_2GaC, Monatshefte Für Chemie 95 (1964) 431–435. http://link. springer. com/10.1007/BF00901306.

[8] J. Lyu, E. B. Kashkarov, Sintering of MAX-phase materials by spark plasma and other methods, Journal of Materials Science 56 (2021) 1980–2015. https://doi.org/10.1007/s10853-020-05359-y.

[9] M. W. Barsoum, T. El-Raghy, Synthesis and characterization of a remarkable ceramic: Ti_3SiC_2, Journal of the American Ceramic Society 79 (1996) 1953–1956. https://doi.org/10.1111/j.1151-2916.1996.tb08018.x.

[10] M. W. Barsoum, D. Brodkin, T. El-raghy, L . AYERED MACHINABLE CERAMICS FOR HIGH TEMPERATURE APPLICATIONS, 36 (1997) 535–541.

[11] M. Radovic, M. Barsoum, MAX Phases: Bridging the gap Between Metals and Ceramics, (2015).

[12] P. Eklund, M. Beckers, U. Jansson, H. Högberg, L. Hultman, The $M_{n+1}AX_n$ phases: Materials science and thin-film processing, Thin Solid Films 518 (2010)

1851–1878. https://doi.org/10.1016/j.tsf.2009.07.184.

[13] J. Ward, D. Bowden, E. Prestat, S. Holdsworth, D. Stewart, M. W. Barsoum, M. Preuss, P. Frankel, Corrosion performance of Ti_3SiC_2, Ti_3AlC_2, Ti_2AlC and Cr_2AlC MAX phases in simulated primary water conditions, Corrosion Science 139 (2018) 444–453. https://doi.org/10.1016/j.corsci. 2018.04.034.

[14] J. L. Smialek, Oxidation of Al_2O_3 Scale-Forming MAX Phases in Turbine Environments, Metallurgical and Materials Transactions A: Physical Metallurgy and Materials Science 49 (2018) 782–792. https://doi.org/10.1007/s11661-017-4346-9.

[15] W. E. Lee, E. Giorgi, R. Harrison, A. Maître, O. Rapaud, Ultra-High Temperature Ceramics: Materials for ExtremeEnvironment Applications, (n. d.).

[16] I. R. Shein, A. L. Ivanovskii, Elastic properties of superconducting MAX phases from first-principles calculations, Physica Status Solidi (B) Basic Research 248 (2011) 228–232. https://doi.org/10.1002/pssb.201046163.

[17] M. Naguib, V. N. Mochalin, M. W. Barsoum, Y. Gogotsi, 25th anniversary article: MXenes: A new family of two-dimensional materials, Advanced Materials 26 (2014) 992–1005. https://doi. org/10.1002/adma. 201304138.

[18] B. Anasori, M. R. Lukatskaya, Y. Gogotsi, 2D metal carbides and nitrides (MXenes) for energy storage, Nature Reviews Materials 2 (2017). https://doi. org/10.1038/natrevmats.2016.98.

[19] P. Eklund, Layered ternary $M_{n+1}AX_n$ phases and their 2D derivative MXene : an overview from a thin-film perspective, (2017). https://doi.org/10.1088/1361-6463/aa57bc.

[20] V. H. Nowotny, Strukturchemie einiger Verbindungen der Übergangsmetalle mit den elementen C, Si, Ge, Sn, Progress in Solid State Chemistry 5 (1971) 27–70.https://doi.org/https://doi.org/10.1016/0079-6786(71)90016-1.

[21] M. Barsoum, The MAX Phases : Unique New Carbide and Nitride Materials, (2014). https://doi.org/10.1511/2001.28.736.

[22] A. Cottrell, Chemical Bonding in Transition Metal Carbides, 1995.

[23] H. O. Pierson, Hand book of Refractory Carbides and Nitrides, Westwood, NJ: Noyes, 1996.

[24] W. Jeitschko, H. Nowotny, F. Benesovsky, Die H-Phasen: Ti_2CdC, Ti_2GaC,

Ti_2GaN, Ti_2InN, Zr_2InN und Nb_2GaC, Monatshefte Für Chemie Und Verwandte Teile Anderer Wissenschaften 95 (1964) 178–179. https://doi.org/10.1007/BF00909264.

[25] W. Jeitschko, H. Nowotny, F. Benesovsky, Kohlenstoffhaltige ternäre Verbindungen (V-Ge-C, Nb-Ga-C, Ta-Ga-C, Ta-Ge-C, Cr-Ga-C und Cr-Ge-C), Monatshefte Für Chemie Und Verwandte Teile Anderer Wissenschaften 94 (1963) 844–850.https://doi.org/10.1007/BF00902358.

[26] W. Jeitschko, H. Nowotny, F. Benesovsky, Ti_2AlN, eine stickstoffhaltige H-Phase, Monatshefte Für Chemie Und Verwandte Teile Anderer Wissenschaften 94 (1963) 1198–1200.https://doi.org/10.1007/BF00905710.

[27] P. Eklund, J. -P. Palmquist, J. Höwing, D. H. Trinh, T. El-Raghy, H. Högberg, L. Hultman, Ta_4AlC_3: Phase determination, polymorphism and deformation, Acta Materialia 55 (2007) 4723–4729. https://doi.org/https://doi.org/10.1016/j.actamat.2007.04.040.

[28] Z. J. Lin, M. J. Zhuo, Y. C. Zhou, M. S. Li, J. Y. Wang, Structural characterization of a new layered-ternary Ta_4AlC_3 ceramic, Journal of Materials Research 21 (2006) 2587–2592. https://doi.org/10.1557/jmr.2006.0310.

[29] C. J. Rawn, M. W. Barsoum, T. El-raghy, A. Procipio, Structure of Ti_4AlN_3 —a layered M, 35 (2008) 1785–1796.

[30] Aosterland, Supporting Information, Unpublished 1803336 (2012) 1–12. https://doi.org/10.1002/adma.

[31] M. Naguib, O. Mashtalir, J. Carle, V. Presser, J. Lu, L. Hultman, Y. Gogotsi, M. W. Barsoum, Two-dimensional transition metal carbides, ACS Nano 6 (2012) 1322–1331. https://doi.org/10.1021/nn204153h.

[32] N. I. Medvedeva, D. L. Novikov, A. L. Ivanovsky, M. V. Kuznetsov, A. J. Freeman, Electronic properties of Ti_3SiC_2-based solid solutions, Physics Review B 58 (1998) 42–50.

[33] J. Haemers, R. Gusmão, Z. Sofer, Synthesis Protocols of the Most Common Layered Carbide and Nitride MAX Phases, Small Methods 4 (2020) 1–32. https://doi.org/10.1002/smtd.201900780.

[34] S. Aryal, R. Sakidja, M. W. Barsoum, W. Y. Ching, A genomic approach to the stability, elastic, and electronic properties of the MAX phases, Physica Status

Solidi (B) Basic Research 251 (2014) 1480–1497. https://doi.org/10.1002/pssb.201451226.

[35] M. W. Barsoum, J. Golczewski, H. J. Seifert, F. Aldinger, Fabrication and electrical and thermal properties of Ti_2InC, Hf2InC and $(Ti,Hf)_2InC$, Journal of Alloys and Compounds 340 (2002) 173–179. https://doi.org/10.1016/S0925-8388(02)00107-X.

[36] V. J. Keast, S. Harris, D. K. Smith, Prediction of the stability of the Mn+1 A Xn phases from first principles, Physical Review B - Condensed Matter and Materials Physics 80 (2009) 1–7. https://doi.org/10.1103/PhysRevB. 80.214113.

[37] Z. J. Yang, L. Tang, A. M. Guo, X. L. Cheng, Z. H. Zhu, X. D. Yang, Origin of c-axis ultraincompressibility of Zr_2InC above 70 GPa via first-principles, Journal of Applied Physics 114 (2013) 1–11. https://doi.org/10.1063/1.4819174.

[38] J. Wang, T. N. Ye, Y. Gong, J. Wu, N. Miao, T. Tada, H. Hosono, Discovery of hexagonal ternary phase Ti_2InB_2 and its evolution to layered boride TiB, Nature Communications 10 (2019) 1–8. https://doi.org/10.1038/s41467-019-10297-8.

[39] M. M. Ali, M. A. Hadi, I. Ahmed, A. F. M. Y. Haider, A. K. M. A. Islam, Physical properties of a novel boron-based ternary compound Ti_2InB_2, Materials Today Communications 25 (2020). https://doi.org/10.1016/j.mtcomm.2020.101600.

[40] H. Bolvardi, J. Emmerlich, M. To Baben, D. Music, J. Von Appen, R. Dronskowski, J. M. Schneider, Systematic study on the electronic structure and mechanical properties of X_2BC (X = Mo, Ti, V, Zr, Nb, Hf, Ta and W), Journal of Physics Condensed Matter 25 (2013). https://doi.org/10.1088/0953-8984/25/4/045501.

[41] M. Dahlqvist, B. Alling, J. Rosén, Stability trends of MAX phases from first principles, Physical Review B - Condensed Matter and Materials Physics 81 (2010) 1–4. https://doi.org/10.1103/PhysRevB. 81. 220102.

[42] O. O. Kurakevych, Superhard phases of simple substances and binary compounds of the B-C-N-O system: From diamond to the latest results (a Review), Journal of Superhard Materials 31 (2009) 139–157. https://doi.org/10.3103/S1063457609030010.

[43] J. Wang, M. Khazaei, M. Arai, N. Umezawa, T. Tada, H. Hosono, Semimetallic

Two-Dimensional TiB_{12}: Improved Stability and Electronic Properties Tunable by Biaxial Strain, Chemistry of Materials 29 (2017) 5922–5930.https://doi.org/10.1021/acs. chemmater.7b01433.

[44] P. Li, R. Zhou, X. C. Zeng, Computational Analysis of Stable Hard Structures in the Ti-B System, ACS Applied Materials and Interfaces 7 (2015) 15607–15617. https://doi.org/10.1021/acsami.5b04332.

[45] G. Surucu, Investigation of structural, electronic, anisotropic elastic, and lattice dynamical properties of MAX phases borides: An Ab-initio study on hypothetical M_2AB (M = Ti, Zr, Hf; A = Al, Ga, In) compounds, Materials Chemistry and Physics 203 (2018) 106–117. https://doi.org/10.1016/j. matchemphys.2017.09.050.

[46] A. Bouhemadou, R. Khenata, M. Kharoubi, Y. Medkour, First-principles study of structural and elastic properties of Sc_2AC (A = Al, Ga, In, Tl), Solid State Communications 146 (2008) 175–180.https://doi.org/10.1016/j. ssc.2008.01.033.

[47] M. S. Hossain, M. A. Ali, M. M. Hossain, M. M. Uddin, Physical properties of predicted MAX phase borides Hf_2AB (A = Pb, Bi): A DFT insight, Materials Today Communications 27 (2021) 102411. https://doi. org/10.1016/j.mtcomm.2021.102411.

[48] M. Khazaei, M. Arai, T. Sasaki, M. Estili, Y. Sakka, Trends in electronic structures and structural properties of MAX phases: A first-principles study on M_2AlC (M = Sc, Ti, Cr, Zr, Nb, Mo, Hf, or Ta), M_2AlN, and hypothetical M2AlB phases, Journal of Physics Condensed Matter 26 (2014). https://doi.org/10.1088/0953-8984/26/50/505503.

[49] D. Music, Z. Sun, J. M. Schneider, Electronic structure of Sc_2AC (A = Al, Ga, in, Tl), Solid State Communications 133 (2005) 381–383. https://doi. org/10.1016/j. ssc.2004.11.034.

[50] M. F. Cover, O. Warschkow, M. M. M. Bilek, D. R. McKenzie, A comprehensive survey of M_2AX phase elastic properties, Journal of Physics Condensed Matter 21 (2009). https://doi.org/10.1088/0953-8984/21/30/305403.

[51] M. A. Ali, M. T. Nasir, M. R. Khatun, A. K. M. A. Islam, S. H. Naqib, An ab initio investigation of vibrational, thermodynamic, and optical properties of

Sc_2AlC MAX compound, Chinese Physics B 25 (2016). https://doi.org/10.1088/1674-1056/25/10/103102.

[52] M. A. Hadi, S. R. G. Christopoulos, A. Chroneos, S. H. Naqib, A. K. M. A. Islam, DFT insights into the electronic structure, mechanical behaviour, lattice dynamics and defect processes in the first Sc-based MAX phase Sc_2SnC, Scientific Reports 12 (2022) 1–16. https://doi.org/10.1038/s41598-022-18336-z.

[53] M. yen, (1966) 29–32.

[54] A. Chowdhury, M. A. Ali, M. M. Hossain, M. M. Uddin, S. H. Naqib, A. K. M. A. Islam, Predicted MAX Phase Sc_2InC: Dynamical Stability, Vibrational and Optical Properties, Physica Status Solidi (B) Basic Research 255 (2018) 1–9. https://doi.org/10.1002/pssb.201700235.

[55] S. Kuchida, T. Muranaka, K. Kawashima, K. Inoue, M. Yoshikawa, J. Akimitsu, Superconductivity in Lu_2SnC, Physica C: Superconductivity and Its Applications 494 (2013) 77–79. https://doi.org/10.1016/j.physc.2013.04.050.

[56] A. Bouhemadou, Calculated structural and elastic properties of M_2InC (M = Sc, Ti, V, Zr, Nb, Hf, Ta), Modern Physics Letters B 22 (2008) 2063–2076. https://doi. org/10.1142/S0217984908016807.

[57] T. Rackl, D. Johrendt, The MAX phase borides Zr_2SB and Hf_2SB, Solid State Sciences 106 (2020) 106316. https://doi.org/10.1016/j.solidstatesciences. 2020.106316.

[58] Q. Zhang, Y. Zhou, X. San, D. Wan, Y. Bao, Q. Feng, S. Grasso, C. Hu, Thermal explosion synthesis of first Te-containing layered ternary Hf_2TeB MAX phase, Journal of the European Ceramic Society 43 (2023) 173–176. https://doi.org/10.1016/j. jeurceramsoc.2022.09.051.

[59] Q. Zhang, Y. Zhou, X. San, W. Li, Y. Bao, Q. Feng, S. Grasso, C. Hu, Zr_2SeB and Hf_2SeB: Two new MAB phase compounds with the Cr_2AlC-type MAX phase (211 phase) crystal structures, Journal of Advanced Ceramics 11 (2022) 1764–1776. https://doi.org/10.1007/s40145-022-0646-7.

[60] D. Ohmer, G. Qiang, I. Opahle, H. K. Singh, H. Zhang, High-throughput design of 211- M_2AX compounds, Physical Review Materials 3 (2019) 1–11. https://doi.org/10.1103/PhysRevMaterials.3.053803.

[61] M. C. Payne, M. P. Teter, D. C. Allan, T. A. Arias, J. D. Joannopoulos, Iterative

minimization techniques for ab initio total-energy calculations: Molecular dynamics and conjugate gradients, Reviews of Modern Physics 64 (1992) 1045–1097. https://doi.org/10.1103/RevModPhys. 64.1045.

[62] H. E. Krizner, D. O. De Haan, J. Kua, Thermodynamics and kinetics of methylglyoxal dimer formation: A computational study, Journal of Physical Chemistry A 113 (2009) 6994–7001. https://doi.org/10.1021/jp903213k.

[63] J. P. Perdew, K. Burke, M. Ernzerhof, Generalized gradient approximation made simple, Physical Review Letters 77 (1996) 3865–3868. https://doi.org/10.1103/PhysRevLett.77.3865.

[64] J. P. Perdew, A. Ruzsinszky, G. I. Csonka, O. A. Vydrov, G. E. Scuseria, L. A. Constantin, X. Zhou, K. Burke, Restoring the density-gradient expansion for exchange in solids and surfaces, Physical Review Letters 100 (2008) 1–4. https://doi.org/10.1103/PhysRevLett. 100.136406.

[65] D. Vanderbilt, Soft self-consistent pseudopotentials in a generalized eigenvalue formalism, Phys. Rev. B 41(11) (1990) 7892–7895.

[66] D. J. Monkhorst, Special points for Brillonin-zone integrations, Physics Review B 13(12) (1976) 5188–5192.

[67] T. H. Fischer, J. Almlöf, General methods for geometry and wave function optimization, Journal of Physical Chemistry 96 (1992) 9768–9774. https://doi. org/10.1021/j100203a036.

[68] K. Refson, P. R. Tulip, S. J. Clark, Variational density-functional perturbation theory for dielectrics and lattice dynamics, Physical Review B - Condensed Matter and Materials Physics 73 (2006) 1–12. https://doi. org/10.1103/PhysRevB. 73.155114.

[69] C. D. Sherrill, Wavefunction Theory Approaches to Noncovalent Interactions, in: Non-Covalent Interactions in Quantum Chemistry and Physics, Elsevier, 2017: pp. 137–168. https://doi. org/10.1016/B978-0-12-809835-6. 00005-0.

[70] U. Bozkaya, Coupled-cluster theory and chemical reactivity, in: Chemical Reactivity, Elsevier, 2023: pp. 65–81. https://doi. org/10.1016/B978-0-32-390257-1. 00009-7.

[71] J. M. Anderson, Bloch Functions: The Basic Theory, in: Operators and Function Theory, Springer Netherlands, Dordrecht, 1985: pp. 1–17. https://doi.

org/10.1007/978-94-009-5374-1_1.

[72] S. J. Clark, M. D. Segall, C. J. Pickard, P. J. Hasnip, M. I. J. Probert, K. Refson, M. C. Payne, First principles methods using CASTEP, Zeitschrift Für Kristallographie - Crystalline Materials 220 (2005) 567–570.https://doi.org/10.1524/zkri.220.5.567.65075.

[73] M. D. Segall, P. J. D. Lindan, M. J. Probert, C. J. Pickard, P. J. Hasnip, S. J. Clark, M. C. Payne, First-principles simulation: ideas, illustrations and the CASTEP code, Journal of Physics: Condensed Matter 14 (2002) 2717–2744. https://doi.org/10.1088/0953-8984/14/11/301.

[74] E. Schrödinger, Annalen der Physik, 79, 361, (1926).

[75] F. W. Kutzler, G. S. Painter, First-row diatomics: Calculation of the geometry and energetics using self-consistent gradient-functional approximations, Physical Review B 45 (1992) 3236–3244. https://doi.org/10.1103/PhysRevB.45.3236.

[76] W. Kohn, L. J. Sham, Self-Consistent Equations Including Exchange and Correlation Effects, Physical Review 140 (1965) A1133–A1138. https://doi.org/10.1103/PhysRev.140.A1133.

[77] J. Tidholm, Lattice dynamics : From fundamental research to practical applications, Linköping University Electronic Press, Linköping, 2020.https://doi.org/10.3384/diss.diva-170800.

[78] J. P. Perdew, K. Burke, M. Ernzerhof, Generalized Gradient Approximation Made Simple, Physical Review Letters 77 (1996) 3865–3868. https://doi.org/10.1103/PhysRevLett.77.3865.

[79] M. Ernzerhof, G. E. Scuseria, Assessment of the Perdew–Burke–Ernzerhof exchange-correlation functional, The Journal of Chemical Physics 110 (1999) 5029–5036. https://doi. org/10.1063/1.478401.

[80] J. D. Pack, H. J. Monkhorst, “special points for Brillouin-zone integrations”-a reply, Physical Review B 16 (1977) 1748–1749. https://doi.org/10.1103/PhysRevB. 16.1748.

[81] J. D. Pack, H. J. Monkhorst, No Title, (1977).

[82] M. L. Cohen, V. Heine, The Fitting of Pseudopotentials to Experimental Data and Their Subsequent Application, in: 1970: pp. 37–248. https://doi.

org/10.1016/S0081-1947(08)60070-3.

[83] S. Aydin, A. Tatar, Y. O. Ciftci, Some new members of MAX family including light-elements: Nanolayered Hf_2XY (X = Al, Si, P and YCombining double low lineB, C, N), Solid State Sciences 53 (2016) 44–55. https://doi.org/10.1016/j. solidstatesciences. 2015.10.010.

[84] M. W. Qureshi, X. Ma, G. Tang, R. Paudel, Ab initio predictions of structure and physical properties of the Zr_2GaC and Hf_2GaC MAX phases under pressure, Scientific Reports 11 (2021) 1–24. https://doi.org/10.1038/s41598-021-82402-1.

[85] Y. Bai, N. Srikanth, C. K. Chua, K. Zhou, Density Functional Theory Study of $M_{n+1}AX_n$ Phases: A Review, Critical Reviews in Solid State and Materials Sciences 44 (2019) 56–107. https://doi.org/10.1080/10408436.2017.1370577.

[86] Omar MA., Elementary solid state physics: principles and applications. , Pearson Education India, 1975.

[87] M. A. Ali, S. H. Naqib, Recently synthesized $(Ti_{1-X}\,Mo_x)_2AlC$ $(0 \leq x \leq 0.20)$ solid solutions: Deciphering the structural, electronic, mechanical and thermodynamic properties via ab initio simulations, RSC Advances 10 (2020) 31535–31546. https://doi.org/10.1039/d0ra06435a.

[88] J. Heyd, G. E. Scuseria, M. Ernzerhof, Hybrid functionals based on a screened Coulomb potential, Journal of Chemical Physics 118 (2003) 8207–8215. https://doi.org/10.1063/1.1564060.

[89] E. F. Rühle M, High-resolution imaging and spectrometry of materials. , Springer Verlag, 2003.

[90] Y. X. Wang, Z. X. Yan, W. Liu, G. L. Zhou, Structure stability, mechanical properties and thermal conductivity of the new hexagonal ternary phase Ti_2InB_2 under pressure, Philosophical Magazine 100 (2020) 2054–2067. https://doi. org/10.1080/14786435. 2020.1754485.

[91] M. A. Ali, A. K. M. A. Islam, $Sn_{1-x}Bi\ xO_2$ and $Sn_{1-x}Ta_xO_2(0\leq x\leq 0.75)$: A first-principles study, Physica B: Condensed Matter 407 (2012) 1020–1026. https://doi.org/10.1016/j. physb.2012.01.002.

[92] H. Li, G. Sun, J. Deng, W. Zhang, L. Xu, W. Jiang, Y. Feng, K. Li, Phonon and electronic properties of Ti_2SiC from first-principles calculations, Solid State Communications 204 (2015) 37–40.https://doi.org/10.1016/j.ssc.2014.12.010.

[93] M. Born, On the stability of crystal lattices. I, Mathematical Proceedings of the Cambridge Philosophical Society 36 (1940) 160–172. https://doi. org/10.1017/S0305004100017138.

[94] M. Zr, H. Max, P. An, M. W. Qureshi, X. Ma, G. Tang, R. Paudel, Structural Stability, Electronic, Mechanical, Phonon, and Thermodynamic Properties of the M_2GaC (M = Zr, Hf) MAX Phase: An ab Initio Calculation, (2020).

[95] M. Rougab, A. Gueddouh, Stability and physical properties of two novel magnetic MAX phase compounds Fe_2AB (A = Cu and Zn) from density functional theory, Materials Today Communications 38 (2024) 108437. https://doi.org/10.1016/j.mtcomm.2024.108437.

[96] S. H. Jhi, J. Ihm, S. G. Loule, M. L. Cohen, Electronic mechanism of hardness enhancement in transition-metal carbonitrides, Nature 399 (1999) 132–134. https://doi.org/10.1038/20148.

[97] W. Tan, S. Zheng, Y. Zhou, X. Wei, L. Zhang, X. Tao, Y. Ouyang, Structural stability and physical properties of MAX phases M_2SX (M = Sc, Y, X = B, C, N) via first-principles calculations, Physica Scripta 98 (2023) 085938. https://doi. org/10.1088/1402-4896/ace500.

[98] W. Voigt, Lehrbuch der Kristallphysik, Lehrbuch der Kristallphysik, 1928.

[99] A. Reuss, Berechnung der Fließgrenze von Mischkristallen auf Grund der Plastizitätsbedingung für Einkristalle , JAMM - Journal of Applied Mathematics and Mechanics / Zeitschrift Für Angewandte Mathematik Und Mechanik 9 (1929) 49–58. https://doi.org/10.1002/zamm.19290090104.

[100] G. Steinle-Neumann, L. Stixrude, R. E. Cohen, First-principles elastic constants for the hcp transition metals Fe, Co, and Re at high pressure, Physical Review B - Condensed Matter and Materials Physics 60 (1999) 791–799. https://doi. org/10.1103/PhysRevB.60.791.

[101] M. A. Ali, M. Roknuzzaman, M. T. Nasir, A. K. M. A. Islam, S. H. Naqib, Structural, elastic, electronic and optical properties of Cu_3MTe_4 (M = Nb, Ta) sulvanites-An ab initio study, International Journal of Modern Physics B 30 (2016). https://doi.org/10.1142/S0217979216500892.

[102] X. Wang, H. Xiang, X. Sun, J. Liu, F. Hou, Y. Zhou, Synthesis, characterization, and sintering behavior of $Yb_3Al_5O_{12}$ powders, Ceramics International 41 (2015)

1735–1742. https://doi.org/10.1016/j.ceramint.2014.09.117.

[103] Y. Zhou, H. Xiang, X. Lu, Z. Feng, Z. Li, Theoretical prediction on mechanical and thermal properties of a promising thermal barrier material: $Y_4Al_2O_9$, Journal of Advanced Ceramics 4 (2015) 83–93. https://doi.org/10.1007/s40145-015-0140-6.

[104] S. F. Pugh, XCII. Relations between the elastic moduli and the plastic properties of polycrystalline pure metals, The London, Edinburgh, and Dublin Philosophical Magazine and Journal of Science 45 (1954) 823–843. https://doi.org/10.1080/14786440808520496.

[105] FRANTSEVICH I. N. , Elastic constants and elastic moduli of metals and insulators, in: Reference Book, 1982.

[106] M. R. Rana, S. Islam, K. Hoque, G. G. Biswas, M. E. Hossain, S. H. Naqib, M. A. Ali, DFT prediction of the stability and physical properties of M_2GaB (M = Sc, V, Nb, Ta), Journal of Materials Research and Technology 24 (2023) 7795–7815. https://doi.org/10.1016/j.jmrt.2023.05.008.

[107] S. Islam, M. R. Rana, K. Hoque, G. G. Biswas, M. E. Hossain, M. M. Hossain, M. M. Uddin, S. H. Naqib, M. A. Ali, A comprehensive exploration of the physical properties of M_2GaB (M = Ti, Zr, Mo, Hf) through DFT method, Results in Materials 19 (2023) 100438. https://doi.org/10.1016/j.rinma.2023.100438.

[108] H. Fu, D. Li, F. Peng, T. Gao, X. Cheng, Ab initio calculations of elastic constants and thermodynamic properties of NiAl under high pressures, Computational Materials Science 44 (2008) 774–778. https://doi.org/10.1016/j.commatsci.2008.05.026.

[109] I. R. Shein, A. L. Ivanovskii, Graphene-like titanium carbides and nitrides $Ti_{n+1}C_n$, $Ti_{n+1}N_n$ (n = 1, 2, and 3) from de-intercalated MAX phases: First-principles probing of their structural, electronic properties and relative stability, Computational Materials Science 65 (2012) 104–114. https://doi.org/10.1016/j.commatsci.2012.07.011.

[110] H. Niu, S. Niu, A. R. Oganov, Simple and accurate model of fracture toughness of solids, Journal of Applied Physics 125 (2019). https://doi.org/10.1063/1.5066311.

[111] M. W. Barsoum, M. Radovic, Elastic and mechanical properties of the MAX phases, Annual Review of Materials Research 41 (2011) 195–227. https://doi. org/10.1146/annurev-matsci-062910-100448.

[112] X. Chen, H. Niu, D. Li, Y. Li, Intermetallics Modeling hardness of polycrystalline materials and bulk metallic glasses, Intermetallics 19 (2011) 1275–1281. https://doi.org/10.1016/j. intermet.2011.03.026.

[113] A. R. Boccaccini, Machinability and brittleness of glass-ceramics, Journal of Materials Processing Technology 65 (1997) 302–304. https://doi. org/10.1016/S0924-0136(96)02275-3.

[114] C. Zuo, C. Zhong, Screen the elastic and thermodynamic properties of MAX solid solution using DFT procedue: Case study on $(Ti_{1-x}Vx)_2AlC$, Materials Chemistry and Physics 250 (2020) 123059. https://doi. org/10.1016/j. matchemphys. 2020.123059.

[115] M. A. Ali, M. M. Hossain, M. M. Uddin, M. A. Hossain, A. K. M. A. Islam, S. H. Naqib, Physical properties of new MAX phase borides M_2SB (M = Zr, Hf and Nb) in comparison with conventional MAX phase carbides M_2SC (M = Zr, Hf and Nb): Comprehensive insights, Journal of Materials Research and Technology 11 (2021) 1000–1018. https://doi.org/10.1016/j. jmrt.2021.01.068.

[116] M. T. Nasir, M. A. Hadi, M. A. Rayhan, M. A. Ali, M. M. Hossain, M. Roknuzzaman, S. H. Naqib, A. K. M. A. Islam, M. M. Uddin, K. Ostrikov, First-Principles Study of Superconducting ScRhP and ScIrP pnictides, Physica Status Solidi (B) Basic Research 254 (2017) 1–10.https://doi.org/10.1002/pssb. 201700336.

[117] M. Rougab, A. Gueddouh, Stability and physical properties of two novel magnetic MAX phase compounds Fe_2AB (A = Cu and Zn) from density functional theory, Materials Today Communications 38 (2024) 108437. https://doi.org/10.1016/j.mtcomm.2024.108437.

[118] M. Naguib, M. Kurtoglu, V. Presser, J. Lu, J. Niu, M. Heon, L. Hultman, Y. Gogotsi, M. W. Barsoum, Two-Dimensional Nanocrystals Produced by Exfoliation of Ti_3AlC_2, Advanced Materials 23 (2011) 4248–4253. https://doi. org/10.1002/adma. 201102306.

[119] M. Naguib, V. Presser, N. Lane, D. Tallman, Y. Gogotsi, J. Lu, L. Hultman, M.

W. Barsoum, Synthesis of a new nanocrystalline titanium aluminum fluoride phase by reaction of Ti_2AlC with hydrofluoric acid, RSC Advances 1 (2011) 1493. https://doi. org/10.1039/c1ra00390a.

[120] D. Sanchez-Portal, E. Artacho, J. M. Soler, Projection of plane-wave calculations into atomic orbitals, Solid State Communications 95 (1995) 685–690.https://doi.org/10.1016/0038-1098(95)00341-X.

[121] R. S. Mulliken, Electronic population analysis on LCAO-MO molecular wave functions. II. Overlap populations, bond orders, and covalent bond energies, The Journal of Chemical Physics 23 (1955) 1841–1846. https://doi. org/10.1063/1. 1740589.

[122] D. Yonghua, M. Lishi, L. Ping, C. Yong, First-principles calculations of electronic structures and optical, phononic, and thermodynamic properties of monoclinic α-spodumene, Ceramics International 43 (2017) 6312–6321. https://doi.org/10.1016/j.ceramint.2017.02.038.

[123] M. A. Hadi, M. S. Ali, S. H. Naqib, A. K. M. A. Islam, Band structure, hardness, thrrmodynamic and optical properties of superconducting Nb_2AsC, Nb_2InC and Mo_2GaC, International Journal of Computational Materials Science and Engineering 02 (2013) 1350007. https://doi.org/10.1142/s2047684113500073.

[124] M. Wang, Y. Li, T. Cui, Y. Ma, G. Zou, Origin of hardness in WB_4 and its implications for ReB_4, TaB_4, MoB_4, TcB_4, and OsB_4, Applied Physics Letters 93 (2008) 4–7. https://doi.org/10.1063/1.2977760.

[125] S. J. Szymanski A, Hardness estimation of minerals, rocks and ceramic materials, Materials science monographs, 1989.

[126] V. V. Glazov VM, Hardness of metals, Izd. Metellurgiya, Moskva. , 1989.

[127] M. A. Ali, Newly Synthesized Ta-Based MAX Phase $(Ta_{1-x}Hf_x)_4AlC_3$ and $(Ta_{1-x}Hf_x)_4Al_{0.5}Sn_{0.5}C_3$ $(0 \leq x \leq 0.25)$ Solid Solutions: Unravelling the Mechanical, Electronic, and Thermodynamic Properties, Physica Status Solidi (B) Basic Research 258 (2021). https://doi.org/10.1002/pssb.202000307.

[128] H. Ledbetter, A. Migliori, A general elastic-anisotropy measure, Journal of Applied Physics 100 (2006) 1–6. https://doi.org/10.1063/1.2338835.

[129] H. M. Ledbetter, Elastic properties of zinc: A compilation and a review, Journal of Physical and Chemical Reference Data 6 (1977) 1181–1203. https://doi.

org/10.1063/1.555564.

[130] M. A. Ali, M. W. Qureshi, Newly synthesized MAX phase Zr_2SeC: DFT insights into physical properties towards possible applications, RSC Advances 11 (2021) 16892–16905. https://doi.org/10.1039/d1ra02345d.

[131] M. M. Hossain, M. A. Ali, M. M. Uddin, M. A. Hossain, M. Rasadujjaman, S. H. Naqib, M. Nagao, S. Watauchi, I. Tanaka, Influence of Se doping on recently synthesized $NaInS_{2-x}Se_x$ solid solutions for potential thermo-mechanical applications studied via first-principles method, Materials Today Communications 26 (2021) 101988. https://doi.org/10.1016/j.mtcomm. 2020.101988.

[132] C. M. Kube, Elastic anisotropy of crystals Elastic anisotropy of crystals, 095209 (2016). https://doi.org/10.1063/1.4962996.

[133] S. I. Ranganathan, M. Ostoja-Starzewski, Universal elastic anisotropy index, Physical Review Letters 101 (2008) 3–6. https://doi. org/10.1103/PhysRevLett. 101.055504.

[134] W. C. Hu, Y. Liu, D. J. Li, X. Q. Zeng, C. S. Xu, First-principles study of structural and electronic properties of C14-type Laves phase Al_2Zr and Al_2Hf, Computational Materials Science 83 (2014) 27–34. https://doi.org/10.1016/j. commatsci. 2013.10.029.

[135] R. Gaillac, P. Pullumbi, F. X. Coudert, ELATE: An open-source online application for analysis and visualization of elastic tensors, Journal of Physics Condensed Matter 28 (2016). https://doi.org/10.1088/0953-8984/28/27/275201.

[136] S. Baroni, P. Giannozzi, E. Isaev, Density-functional perturbation theory for quasi-harmonic calculations, Theoretical and Computational Methods in Mineral Physics: Geophysical Applications 71 (2018) 39–58. https://doi. org/10.2138/rmg.2010.71.3.

[137] C. Lee, X. Gonze, Ab initio calculation of the thermodynamic properties and atomic temperature factors of SiO_2 α-quartz and stishovite, Physical Review B 51 (1995) 8610–8613. https://doi.org/10.1103/PhysRevB.51.8610.

[138] M. A. Rayhan, M. A. Ali, S. H. Naqib, A. K. M. A. Islam, First-principles Study of Vickers Hardness and Thermodynamic Properties of Ti_3SnC_2 Polymorphs, Journal of Scientific Research 7 (2015) 53–64. https://doi.org/10.3329/jsr.v7i3.

23182.

[139] T. Plirdpring, K. Kurosaki, A. Kosuga, T. Day, S. Firdosy, V. Ravi, G. J. Snyder, A. Harnwunggmoung, T. Sugahara, Y. Ohishi, H. Muta, S. Yamanaka, Chalcopyrite $CuGaTe_2$: A high-efficiency bulk thermoelectric material, Advanced Materials 24 (2012) 3622–3626. https://doi.org/10.1002/adma.201200732.

[140] M. Elamin Ketfi, H. Bennacer, S. S. Essaoud, M. Issam Ziane, A. Boukortt, Computational evaluation of optoelectronic, thermodynamic and electron transport properties of $CuYZ_2$ (Z = S, Se and Te) chalcogenides semiconductors, Materials Chemistry and Physics 277 (2022) 125553. https://doi.org/10.1016/j.matchemphys.2021.125553.

[141] X. Luo, B. Wang, Structural and elastic properties of $LaAlO_3$ from first-principles calculations, Journal of Applied Physics 104 (2008) 0–7. https://doi.org/10.1063/1.2990068.

[142] O. L. Anderson, a Simplified Method for Calculating the, J. Phys. Chem. Solids 24 (1963) 909–917.

[143] M. A. Hadi, M. Dahlqvist, S. R. G. Christopoulos, S. H. Naqib, A. Chroneos, A. K. M. A. Islam, Chemically stable new MAX phase V_2SnC: A damage and radiation tolerant TBC material, RSC Advances 10 (2020) 43783–43798. https://doi.org/10.1039/d0ra07730e.

[144] M. E. Fine, L. D. Brown, H. L. Marcus, Elastic constants versus melting temperature in metals, Scripta Metallurgica 18 (1984) 951–956. https://doi.org/10.1016/0036-9748(84)90267-9.

[145] G. A. Slack, The Thermal Conductivity of Nonmetallic Crystals, Solid State Physics - Advances in Research and Applications 34 (1979) 1–71. https://doi.org/10.1016/S0081-1947(08)60359-8.

[146] D. R. Clarke, Materials selections guidelines for low thermal conductivity thermal barrier coatings, Surface and Coatings Technology 163–164 (2003) 67–74. https://doi.org/10.1016/S0257-8972(02)00593-5.

[147] M. M. Uddin, M. A. Ali, M. M. Hossain, S. H. Naqib, A. K. M. A. Islam, Comparative study of predicted MAX phase Hf_2AlN with recently synthesized Hf_2AlC: a first principle calculations, Indian Journal of Physics 96 (2022) 1321–

1333. https://doi.org/10.1007/s12648-021-02050-z.

[148] A. Settouf, H. Rached, N. Benkhettou, D. Rached, DFT calculations of structural, optoelectronic and thermodynamic properties of $BxAl_{1-x}$ P alloys, Computational Condensed Matter 19 (2019) e00377. https://doi.org/10.1016/j.cocom.2019.e00377.

[149] H. Rached, S. Bendaoudia, D. Rached, Investigation of Iron-based double perovskite oxides on the magnetic phase stability, mechanical, electronic and optical properties via first-principles calculation, Materials Chemistry and Physics 193 (2017) 453–469. https://doi.org/10.1016/j.matchemphys.2017.03.006.

[150] R. C. Fang, Solid Spectroscopy, Chinese Science Technology University Press, Hefei, 2003.

[151] Ming Fu Li, Physics of Semiconductor, Science Press,Beijing, 1991.

[152] Y. Z. and W. M. Shen, Basic of Solid Electronics, Zhe Jiang University Press, Hangzhou, 2005.

[153] S. Saha, T. P. Sinha, A. Mookerjee, Electronic structure, chemical bonding, and optical properties of paraelectric $BaTiO_3$, Physical Review B - Condensed Matter and Materials Physics 62 (2000) 8828–8834. https://doi.org/10.1103/PhysRevB.62.8828.

[154] S. Li, R. Ahuja, M. W. Barsoum, P. Jena, B. Johansson, Optical properties of Ti_3SiC_2 and Ti_4AlN_3, Applied Physics Letters 92 (2008) 90–93. https://doi.org/10.1063/1.2938862.